REPORT DOCUMENTATION PAGE

1. AGENCY USE ONLY (Leave blank)	2. REPORT DATE 12 September 1997	3. REPORT TYPE AND DATES COVERED Final Report (1 May 94 - 30 Apr 97)

4. TITLE AND SUBTITLE

Calibration of Regional Wave Discriminants in Diverse Geological Environments: Topographic Correlations

5. FUNDING NUMBERS

AFOSR-TR-97

F49620-94-1-0247

0636

6. AUTHOR(S)

Thorne Lay

7. PERFORMING ORGANIZATION NAME(S) AND ADDRESS(ES)

University of California, Santa Cruz
Institute of Tectonics/Earth Sciences Department
Santa Cruz, CA 95064

8. PERFORMING ORGANIZATION REPORT NUMBER

9. SPONSORING/MONITORING AGENCY NAME(S) AND ADDRESS(ES)

AFOSR/NL (Sponsor)
110 Duncan Ave. Suite B115
Bolling AFB DC 20332-8050
Prof. Man.: Stanley Dickinson/NL

10. SPONSORING/MONITORING AGENCY REPORT NUMBER

11. SUPPLEMENTARY NOTES

19971204 175

12a. DISTRIBUTION/AVAILABILITY STATEMENT

Approval for public release: distribution unlimited

13. ABSTRACT (Maximum 200 words)

This is the final report for this grant to explore waveguide effects on high frequency regional signals. Three studies are presented. The first is a theoretical investigation of the effects of thin crustal structure on Lg propagation. This study demonstrates that standard Lg in the frequency band 0.3 to 2 Hz does not develop in crustal structures less than 10 km thick due to a lack of overtone energy. This is the primary explanation for why oceanic crust blocks Lg phases in this frequency band. A second study demonstrates that surface topography variations are correlated with Pg/Lg amplitude ratios for frequencies less than 3 Hz, using broadband observations in the western U.S.. Optimal variance reduction of Pg/Lg amplitude ratio measurements (a common seismic discriminant), are achieved by using empirical relationships with propagation distance and roughness. Pn/Lg data show less sensitivity to surface topography variations, but strong distance dependence. The third study demonstrates the complexity of high frequency wavefields in tectonically active regions, using a very dense short period array deployed in the Santa Cruz Mountains area. Large apparent back-azimuth deflections, of up to 60 degrees, are found for P wave particle motions and f-k measurements, and appear to be the result of shallow dipping layers under the array. Spatial coherence of the high frequency wavefield exhibits strong decreases with frequency and sensor offset.

14. SUBJECT TERMS

Lg Blockage
Regional Waves

DTIC QUALITY INSPECTED 4

15. NUMBER OF PAGES

43

16. PRICE CODE

17. SECURITY CLASSIFICATION OF REPORT	18. SECURITY CLASSIFICATION OF THIS PAGE	19. SECURITY CLASSIFICATION OF ABSTRACT	20. LIMITATION OF ABSTRACT
Unclassified	Unclassified	Unclassified	SAR

Table of Contents

Why the L_g Phase Does Not Traverse Oceanic Crust

by Tian-Run Zhang and Thorne Lay

Abstract It has long been recognized that L_g waves are not observed on paths traversing oceanic crust, but this has not yet been fully explained. Using normal-mode analysis and finite-difference simulations, we demonstrate that (1) the overall thickness of the crustal wave guide affects the number of normal modes in a given frequency range; in general, thinner crust accommodates fewer modes; (2) 6-km-thick oceanic crust does not allow L_g to develop as a significant phase in the frequency band 0.3 to 2 Hz because of the limited number of modes that exist; (3) in continental crust thicker than 15 km, there are usually sufficient modes that L_g is stable; (4) the shallow sediment layer plays important roles in crustal-guided wave propagation, trapping energy near the surface, separating L_g and R_g waves; (5) a 100-km-long segment of oceanic structure on a mixed ocean/continent path can block P–SV type L_g propagation. The primary reason why L_g does not travel through oceanic crust thus lies in the structure of the crustal wave guide, with the decisive factor being the crustal thickness. The detailed shape of ocean-to-continent crustal transitions can influence L_g blockage, but the general inefficiency of L_g propagation in the oceanic structure is the dominant effect.

Introduction

Early observations detected L_g extinction when the propagation path included an oceanic portion with length greater than 100 to 200 km (Press and Ewing, 1952). However, the reason why L_g only propagates in continental crust still remains unclear after four decades, and the basis for characterizing crustal structure using L_g propagation efficiency has been questioned (Regan and Harkrider, 1989a).

Ewing et al. (1957) hypothesized that the disappearance of L_g in oceanic regions might be due to the effect of propagation across a continent-ocean margin. Kennett (1986) has illustrated this hypothesis with ray diagrams. There is no doubt that initially trapped L_g energy will radiate out of the crust when passing through a tapered wave guide, as the varying geometry allows some postcritical raypaths to become precritical (e.g., Kock, 1965; Bostock and Kennett, 1990). If this is the main reason, the structure of the continental margins would play a more important role than the structure of the oceanic crust itself in disrupting L_g propagation. However, there have been observations along purely oceanic paths in the Atlantic and Pacific (for earthquakes at trenches and receivers on small islands) that show no short-period L_g arrivals (Knopoff et al., 1979). Knopoff et al. (1979) found that clustering of higher-mode group velocity minima (the generally recognized cause of the L_g phase (e.g., Knopoff et al., 1973)) is absent in simple oceanic crustal structures. This suggests that the reason for L_g not being observed on paths with mixed continental and oceanic crust may lie in the structure of oceanic crust, rather than in the

details of the continental margin. We will explore this issue using synthetic seismograms for both one-dimensional crustal models and two-dimensional continent-ocean transitions in this study.

The importance of understanding crustal wave-guide controls on L_g has prompted several modeling studies of blockage, but the observations have been hard to simulate (Maupin, 1989; Regan and Harkrider, 1989a, 1989b; Campillo et al., 1993; Chazalon et al., 1993; Gibson and Campillo, 1994). These authors argue that unmodeled small-scale heterogeneity is needed to account for the blockage rather than large-scale wave-guide structure. Recently, Cao and Muirhead (1993) used a two-dimensional P–SV finite-difference method to explore L_g blockage. Because the reduction of L_g obtained in models that involve a segment of thinned crust is not as strong as required by observations, they introduced a water layer overlying the thinned crust that further reduces the energy they identify as L_g. We perform finite-difference calculations similar to those of Cao and Muirhead (1993) and draw somewhat different conclusions in this study by taking care to separate the effects of wave-guide structure on L_g and R_g.

In this article, we consider the basic nature of L_g in oceanic and continental wave guides along with further investigation of L_g blockage for the P–SV component. We use normal-mode analysis and a two-dimensional fourth-order elastic wave finite-difference method (Xie and Yao, 1988) to construct dispersion curves and synthetic velocity seis-

mograms for L_g in one- and two-dimensional crustal models. Our basic objective is to improve our understanding of the relative efficiency of L_g excitation and propagation in oceanic and continental structures.

Crustal Thickness and the Number of Normal Modes

To first order, we can view the crust as a low-velocity layer over a higher-velocity half-space. In such a simple system, the L_g phase can be visualized either as trapped postcritical reflections (e.g., Campillo, 1990) or, equivalently, as Rayleigh and Love wave overtones (e.g., Kovach and Anderson, 1964; Knopoff et al., 1973). In the latter interpretation, it is necessary to consider a substantial number of overtones to produce the complexity and interference characterizing the L_g phase. It is well known that as wave-guide thickness and/or frequency decrease, the number of surface-wave overtones reduces (e.g., Marcuse, 1991, p. 12). Aki and Richards (1980, p. 264) give the traditional formula for calculating the cutoff frequency of the nth higher-mode ω_{cn} for the case of Love waves in a simple layer over a half-space model:

$$\omega_{cn} = \frac{n\pi\beta_1}{H\left(1 - \frac{\beta_1^2}{\beta_2^2}\right)^{1/2}}, \tag{1}$$

where H is the thickness of the crustal layer (wave guide), β_1 is the shear-wave velocity in the wave guide, β_2 is the shear-wave velocity in the half-space, n is the order number of that higher mode. This expression is commonly used for fixed H and n. Alternatively, if we specify a maximum frequency and the layer thickness, we can express the maximum number of viable overtones in the system, n_c, as

$$n_c = \frac{\omega H}{\pi\beta_1}\left(1 - \frac{\beta_1^2}{\beta_2^2}\right)^{1/2}, \tag{2}$$

with truncation to an integer value being assumed. Equation (2) shows that the maximum number of normal modes up to a particular frequency is determined by the wave-guide thickness and the wave velocities. The corresponding solution for the number of Rayleigh wave overtones up to a certain frequency is similar but more complicated. Fewer normal modes exist as thinner wave guides are considered. The existence of the Rayleigh wave fundamental mode does not depend on the wave-guide thickness, and even when the thickness is so small that no higher modes can propagate in the wave guide, the fundamental mode will still exist (e.g., Brekhovskikh, 1980, p. 64).

To further explore the dependence of number of modes on crustal thickness, we calculated the Rayleigh wave dispersion curves for a simple one-layer crustal model like that in Figure 1a. We assign the crustal layer the density, S-wave velocity and P-wave velocity values corresponding to "ba-

salt," and the half-space the parameters corresponding to "mantle," given in Table 1. These parameters follow those used by Cao and Muirhead (1993). Group velocity dispersion curves were calculated in the frequency range of 0.0 to 2.0 Hz for varying crustal thickness, using the codes developed by Herrmann and Wang (1985). For a 32-km-thick crust (Fig. 2a), the group velocity minima (or Airy phases) concentrate within a narrow group velocity range between 3 and 3.5 km/sec. The concentrated L_g phase develops by constructive interference of these higher-mode Airy phases. The fundamental-mode Airy-phase group velocity is slightly lower than that of any of the overtones, so there will be some separation of the L_g phase and the R_g phase, but not very much for this model.

As the thickness decreases, the cutoff frequencies for the dispersion curves shift to higher frequencies, reducing the number of overtones. For the 0- to 2-Hz band, there are 24 modes for a 32-km-thick crust, 19 modes for a 25-km-thick crust, 12 modes for a 15-km-thick crust, and only 5 modes for the 6-km-thick (oceanic) crust (Fig. 2). With the velocities of crust and mantle being held fixed, the Airy-phase group velocities do not vary significantly. The number-of-modes versus layer thickness behavior of Rayleigh waves for constant velocity models clearly exhibits a quasi-linear relationship. As expected from equation (2), Love waves display a similar behavior.

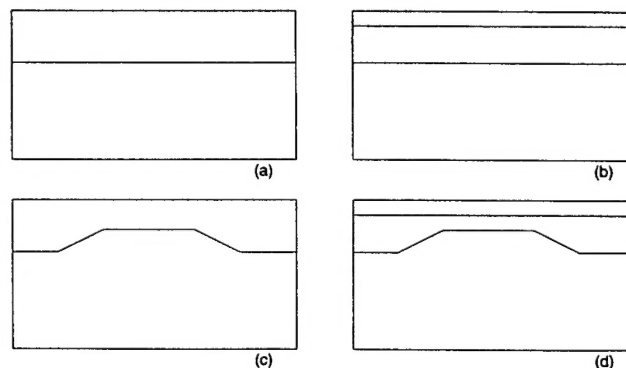This simple calculation holds no surprises, but it does

Figure 1. Four categories of crustal model used in this study including (a) a layer over half-space model; (b) a two-layer crust model, with a sediment layer added on top of model (a); (c) a model with a segment of thin crust; (d) a model with a segment of thin crust and a sediment layer.

Table 1
Model Parameters Used in Finite-Difference Simulation

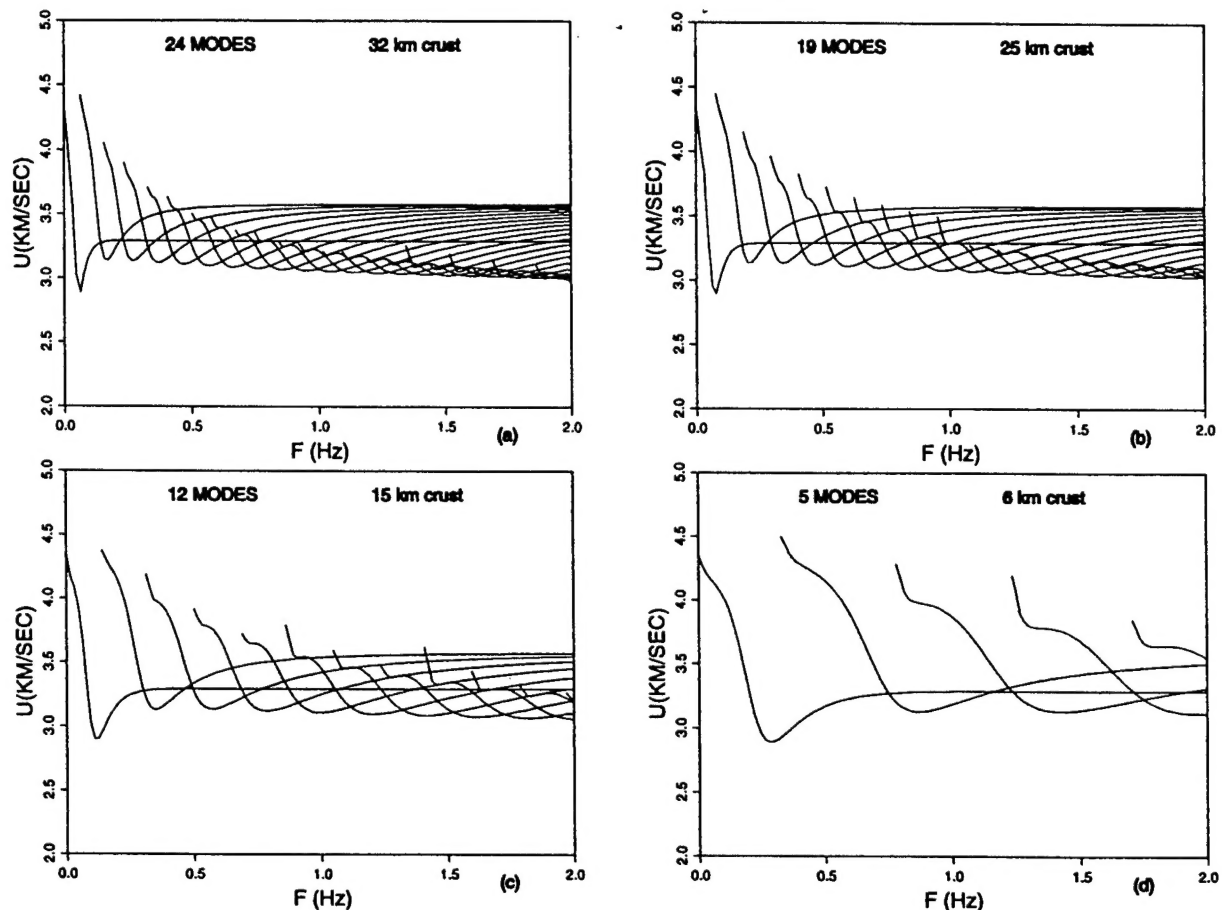|	Density (gm/cm³)	S-wave velocity (km/sec)	P-wave velocity (km/sec)
Sediment	2.2	2.60	4.50
Basalt	2.8	3.58	6.20
Mantle	3.4	4.73	8.20

Figure 2.   Dispersion curves for Rayleigh waves in layer over half-space models with crustal thickness of (a) 32 km, (b) 25 km, (c) 15 km, and (d) 6 km. U stands for group velocity. The number of normal modes in the 0 to 2 Hz range decreases for thinner crust.

focus attention on the issue that the development of the L_g phase will depend on the number of interfering modes, which is strongly influenced by crustal thickness. To some extent, this issue has not been carefully considered in many of the investigations of wave-guide effects on L_g.

L_g Synthetics for 1D Models

In this section, we explore further the effects of gross one-dimensional homogeneous wave-guide structure on L_g wave propagation. We do not introduce intrinsic attenuation or small-scale scattering in our calculations, although these are undoubtedly important effects for L_g in the Earth. Following Xie and Lay (1994), a Gaussian derivative source-time history, $(t - t_s)\exp[-(t - t_s)^2/\tau^2]$, is used for all of the finite-difference calculations, where t_s is a reference time and τ is the characteristic width of the source pulse. We use $\tau = 0.5$ sec in all the calculations. The main energy of this source-time history is between 0.1 and 1.0 Hz, which is the frequency band relevant to the majority of observational studies of L_g propagation. Press and Ewing (1952) originally

defined L_g within the 0.17- to 2.0-Hz band, and many of the applications of L_g for magnitude measures (e.g., Nuttli, 1986) use 1-Hz L_g amplitudes. Many early theoretical studies of L_g (e.g., Knopoff *et al.*, 1973; Panza and Calcagnile, 1975) compute synthetics for the frequency range less than 1 Hz, similar to the calculations given in the following section.

Layer over Half-Space Models

In the previous section, we showed that wave-guide thickness influences the number of modes in a given frequency band. While it makes sense that there will be a corresponding effect on the time-domain amplitude of L_g, it is important to assess how strong this effect is. We perform finite-difference calculations for the same crustal models used for the earlier dispersion calculations, in order to construct complete seismograms for a realistic source. Normal-mode calculations could have been used to produce the synthetic seismograms, but the finite-difference approach has the advantage of readily including all of the body-wave phases that provide references for the L_g amplitudes. For all models explored in this article, the source is located at the

left end of the model at a depth of 5 km. The source is a 45° dip-slip dislocation for all finite-difference calculations. Synthetic seismograms are calculated at 18 locations with spacing of 20 km on the free surface, starting 100 km away from the source and ending at 440 km. In this distance range, L_g evolves from discrete crustal reverberations to a complex interference pattern.

Figure 3 shows synthetic seismograms for both radial and vertical components for a constant velocity ("basalt" parameters), single-layer, 32-km-thick crust model. The two reference lines indicate the group velocity window 3.7 to 3.1 km/sec, which is commonly used for RMS L_g calculation (e.g., Israelson, 1992; Zhang and Lay, 1994a, 1994b; Zhang et al., 1994). This is called the "L_g window," although in a strict sense, it may only be valid for typical continental crust, given that overtone group velocities in oceanic structure may differ from those in the continents. The two major regional surface-wave phases, R_g and L_g, overlap within the L_g win-

dow because the group velocity of the fundamental mode Airy phase is only slightly lower than that of the higher modes (Fig. 2a). The R_g phase is dominated by lower-frequency energy and has the largest amplitudes in the L_g window, with the vertical component being stronger than the radial component. The mix of Rayleigh wave arrivals in the L_g window has amplitudes comparable to the P_g phase on the radial components.

To verify the coexistence of the two phases (L_g and R_g), we consider particle motions for the arrivals within the L_g window (Fig. 4). Figure 4a shows waveforms of the two components in the L_g window. Treating the radial amplitudes as x coordinates and vertical amplitudes as y coordinates, we convert the (x, y) pairs to (r, θ) polar coordinates and show the variation of θ with time in Figure 4b. If the particle motions are retrograde ellipses, the phase angle θ must increase monotonically from 0 to 2π, then wrap around. The early part of the seismogram segment shown in Figure 4a
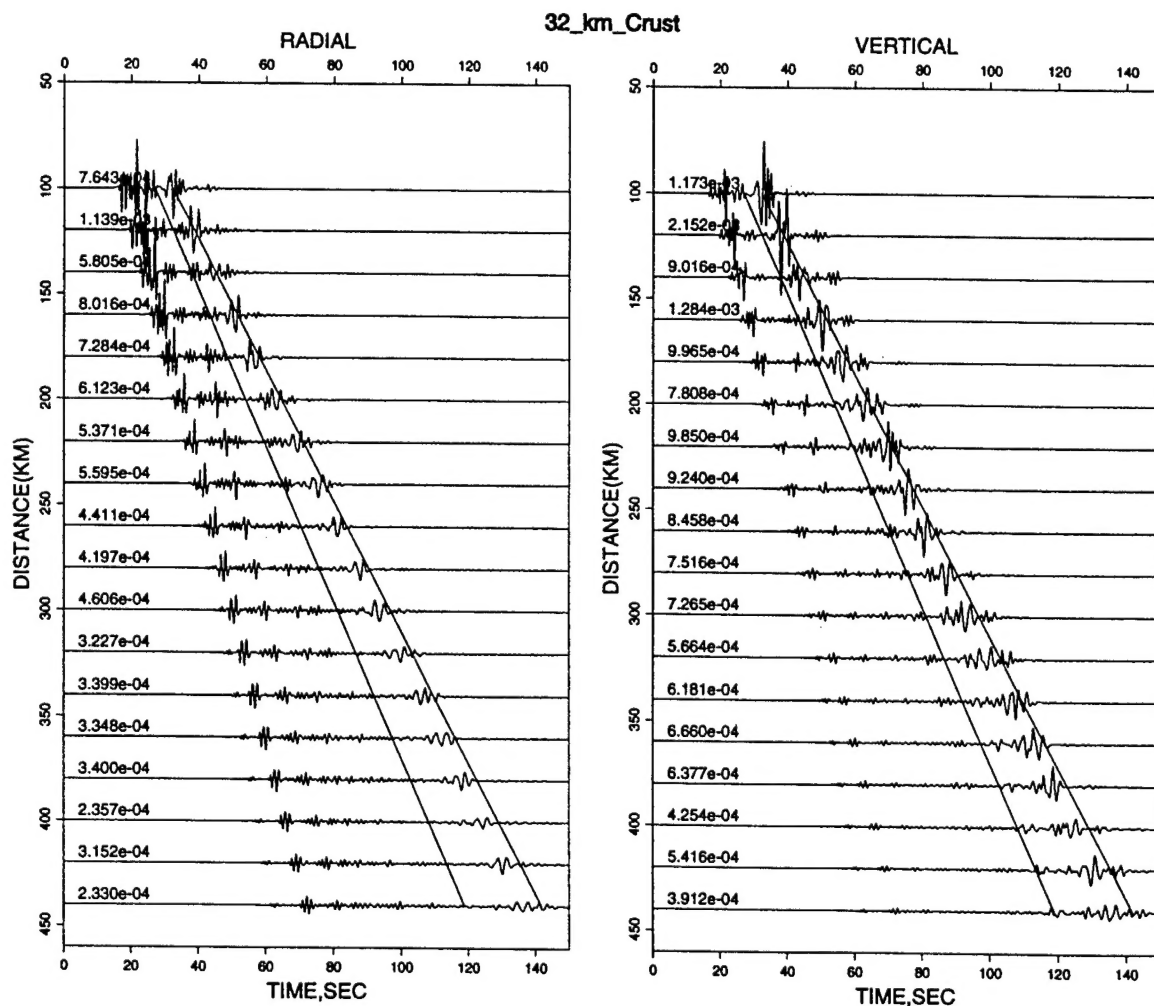

Figure 3.   Synthetic seismograms for a layer over half-space model with 32-km-thick crust. Both radial and vertical components are shown. Two lines mark the group velocity window 3.7 to 3.1 km/sec used for calculation of RMS L_g amplitudes (called the L_g window). The RMS amplitude values in the L_g window are shown for each waveform.
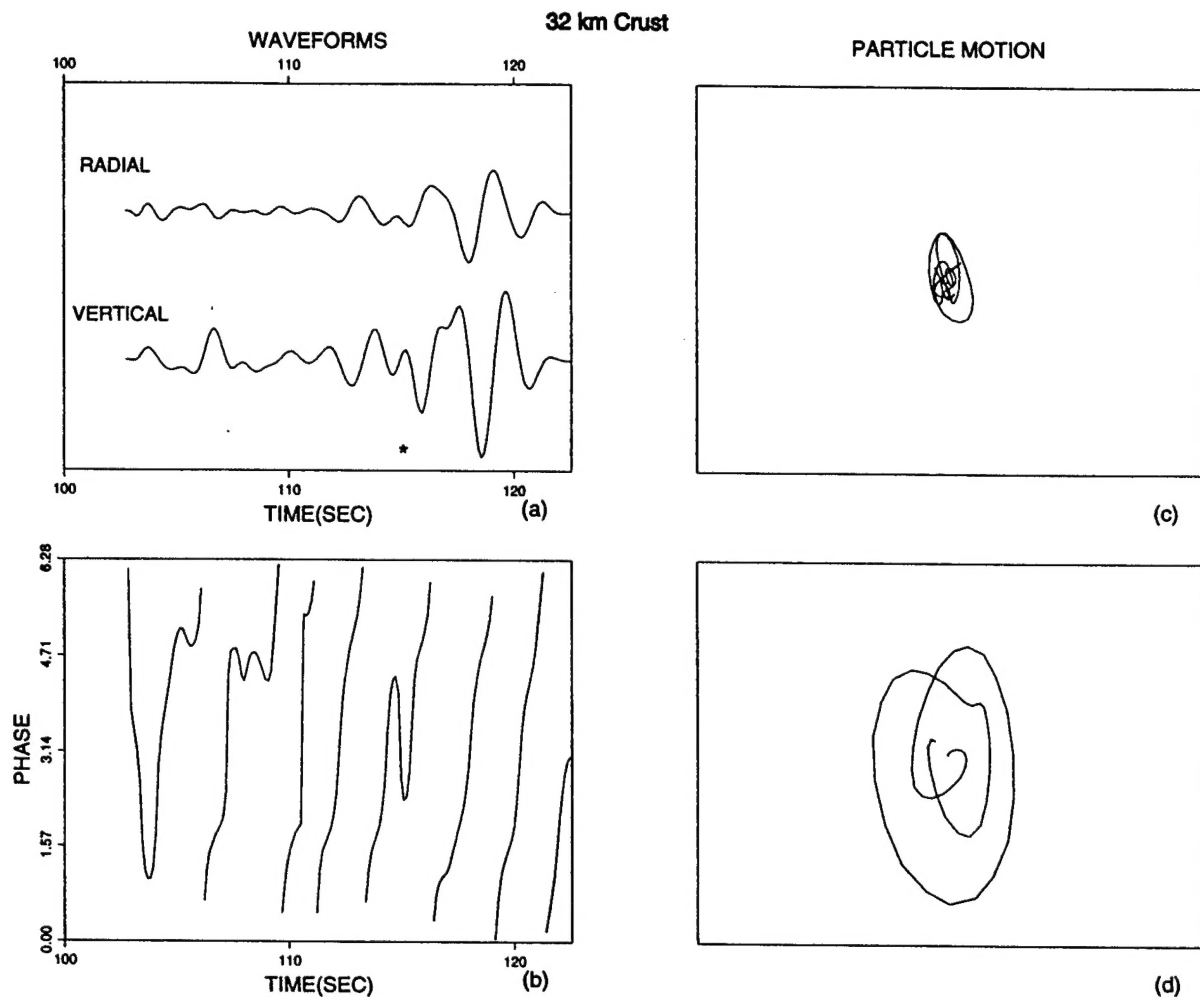
32 km Crust

WAVEFORMS

PARTICLE MOTION

Figure 4. Particle motions in the L_g window for the waveform at 380-km distance in Figure 3: (a) shows the radial and vertical components in the L_g window. The asterisk marks a transition in characteristic particle motion, and (b) is the polarization angle as a function of time (see text). Both (c) and (d) are the particle motions of the early part of the L_g window before the asterisk and the late part of the L_g window, respectively. R_g dominates the late part, while higher modes dominate the early part.

exhibits complex phase, while the later part is predominantly retrograde elliptical, with smoothly increasing phase (Fig. 4b). The asterisk on Figure 4a marks the approximate transition between the two domains. The particle motions for the two separate waveform intervals are shown in Figures 4c and 4d. The later part is predominantly the R_g arrival, but there is some higher-mode energy present, which makes the ellipses irregular. The early part shows complex, interfering motions that imply the presence of the multiple arrivals constituting L_g, but there is some elliptical motion indicating contribution from the fundamental mode within the L_g window. We calculate RMS amplitudes for the L_g window, recognizing that in some models, there is contamination by R_g.

We constructed synthetic profiles for models with crustal thicknesses of 25 and 15 km, finding that although the reduction of number of Rayleigh wave overtones is considerable (Fig. 2), the RMS amplitude values within L_g win-

dow are not much different than for the 32-km-thick model. The reasons are (1) R_g dominates in this window, and (2) the most important contributions to the L_g phase come from the first few modes (Knopoff *et al.,* 1973). There may be a tendency for the lower modes to enhance in strength when fewer modes fit into the system, but the overall overtone energy must begin to drop off when the number of modes becomes very small. This appears to occur as the crustal thickness becomes as small as for oceanic structure. The synthetics for a 6-km-thick crustal model (model I in Table 2) shown in Figure 5 illustrate this effect. There is almost no energy in the L_g window. Only five modes and three overtone Airy phases exist in the 0- to 2-Hz frequency range (Fig. 2d), and only one overtone has an Airy phase in the band 0 to 1 Hz. The arrivals just after the L_g window are R_g, which does not stay in the L_g window in the 6-km-thick crust case. The short-period fundamental mode energy has be-

Table 2

Six Crustal Models Used in This Model*

	Layer 1 (H/V_p)	Layer 2 (H/V_p)	Layer 3 (H/V_p)	Layer 4 (H/V_p)	Layer 5 (H/V_p)	Layer 6 (H/V_p)
I	6.0/6.2	∞/8.2				
II	2.0/4.5	4.0/6.2	∞/8.2			
III	1.0/2.10	5.0/6.41	∞/8.1			
IV	0.34/2.10	1.21/5.15	4.57/6.82	∞/8.15		
V	0.5/2.08	0.95/4.46	1.15/6.0	1.70/6.74	2.90/7.47	∞/8.28
VI	10.0/6.06	20.0/6.35	20.0/7.05	∞/8.17		

*H is the layer thickness in kilometers, V_p is the P-wave velocity in km/sec. Model I stands for a single-layer oceanic crust; II is the oceanic crust model with a 2-km-thick low-velocity layer on the top; III is the worldwide ocean crust model from Meissner (1986); IV and V are two Pacific crust models from Shor *et al.* (1970) and Hussong (1972); VI is the worldwide continent model from Meissner (1986).

come stronger relative to the body waves compared to the thicker crustal models due to the shift of the Airy-phase frequency (Fig. 2). However, with a group velocity of about 2.8 km/sec, most of this energy is now outside the L_g window. This calculation demonstrates that a thin uniform wave guide, approximating the oceanic crust, is very inefficient for the transmission of 0- to 1-Hz L_g waves, relative to the body wave and fundamental mode energy. We obtain this result without introducing a continent-ocean transition.

The RMS L_g amplitudes along profiles from 200 to 440 km for several different models are summarized in Figure 6. The solid circles and squares indicate the results for the 32- and 6-km-thick crustal models, respectively. The L_g signal is very weak in 6-km-thick crust, especially when the distance is greater than 300 km. The beating of the fundamental mode and overtones in the thicker crustal models causes the fluctuations with distance.

Crustal Models with a Sediment Layer

The presence of R_g in the L_g window, as in the synthetics in the previous section, is rarely observed. When present at all, R_g is typically significantly later than L_g, with a characteristic continental path group velocity of 3.05 ± 0.07 km/
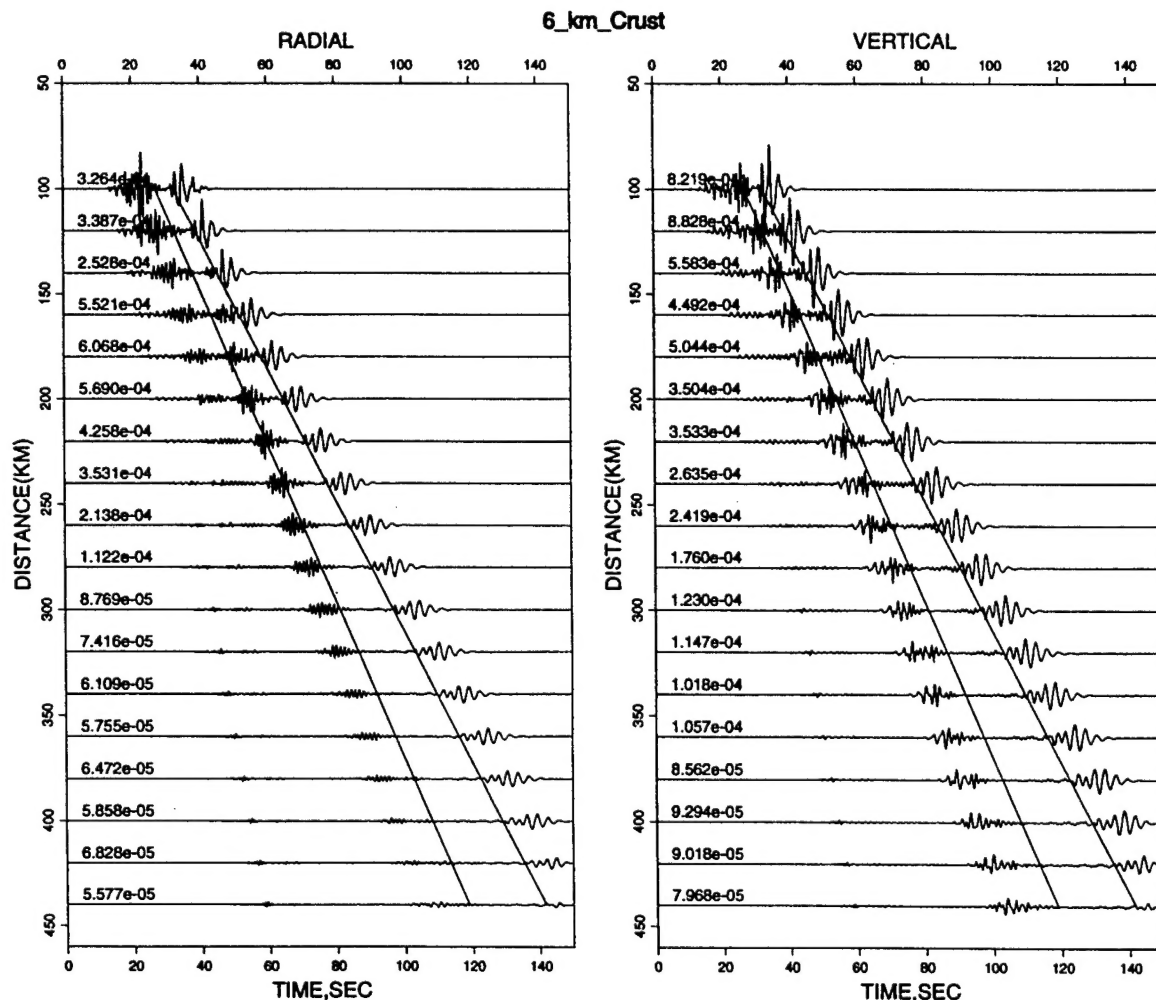

Figure 5. Synthetic seismograms for a layer over half-space model with 6-km crustal thickness. The arrivals within the L_g window are weak. The R_g waves are delayed, and most of their energy is outside the L_g window.

sec (Press and Ewing, 1952). This low group velocity is largely due to layering of the crust, in particular the presence of low-velocity surface layers. To include this in the synthetics, we add a 2-km-thick low-velocity layer at the top of each crustal model, as illustrated in Figure 1b and model II in Table 2. The velocities and density of the "sediment" layer are listed in Table 1.

The low-velocity surface layer has two effects on the Rayleigh wave modes. First, it lowers the group velocities of the Airy phases of all the modes. Second, it tends to trap shorter-period fundamental-mode energy within the shallow crust, slowing it down considerably. The dispersion curves of the fundamental mode have two minima for these three-layer models (Fig. 7). The low-frequency Airy phase is basically the same as for the single-layer crust, with a slight reduction in group velocity, because the average crustal velocities are reduced (see Fig. 2 for comparison). The second Airy phase involves the energy trapped in the surface layer and has quite low velocity over a range of periods from 2 to 1 sec. The short-period R_g amplitudes are now quite strong, as illustrated by the synthetic seismograms for a 32-km-thick crustal model shown in Figure 8. From the dispersion curves for different crustal thicknesses (Fig. 7), we find that the first higher mode has a similar double minima at higher frequency, but other modes do not change much compared with models without the sediment layer in the 0 to 2 Hz range. As a result of the low-velocity layer, L_g and R_g are separated in the time domain. This separation eliminates the overlap of L_g and R_g in the L_g window. Analysis of the particle motions now shows complex interfering motion throughout the L_g window (Figs. 9b and 9c), implying the clustering of higher modes. The R_g arrival, concentrated in the following time interval, shows stable retrograde elliptical motion (Figs. 9b and 9d). Aside from this delay of R_g, the behavior of the RMS L_g amplitudes as a function of overall wave-guide thickness is very much the same as described for the single-layer crust. Using synthetic profiles computed for each of the crustal thicknesses in Figure 7, RMS L_g amplitudes were computed at each distance and are shown by open symbols in Figure 6. While RMS amplitudes in the L_g window are systematically reduced relative to the single-layer crustal models, the result of R_g being delayed out of the window, the L_g amplitudes are still much higher (by a factor of 4 to 5) for the thicker crusts than for the oceanic-type crust. Figure 7 suggests that the reason for this is still the reduction of the number of overtones with which to build up the L_g phase. The beating patterns with distance are reduced in Figure 6 because there is much less interference between L_g and R_g.

The oceanic crustal model with 2-km-thick sediment and 4-km-thick basalt layers generates strong R_g but almost no L_g (Fig. 10). It is apparent from Figures 7 and 10 that this is in part due to the absence of Airy phases in the 3.1- to 3.7-km/sec L_g window, but it is also clear that what overtones are present do not have clustered Airy phases as do the thicker crustal models. This means that the absence of

L_g is not just for the conventional window, but there is simply little possible oceanic L_g phase as a result of the wave-guide structure. The large amplitude of R_g implies an effect of trapping most of the fundamental mode energy in a narrow low-velocity layer, with the energy flux being much greater than that in the continental cases. In these theoretical calculations, which lack attenuation and scattering, R_g is predicted to be a dominant arrival for both oceanic and continental paths. In actuality, near-surface heterogeneities and attenuation tend to greatly reduce the short-period fundamental mode energy. Some of the R_g energy is probably scattered into the L_g phase (e.g., Gupta *et al.*, 1992), but even for the large amplitude R_g in the oceanic crust, this is not expected to significantly enhance L_g because the overtone modes simply do not exist to accommodate the scattered energy. For the oceanic structure, the S_n phase before the L_g window is very strong, especially for the radial component. We put in much effort to distinguish between L_g and R_g phases, because some researchers have neglected this problem in their simulations of L_g.

More Complex 1D Crustal Models

We have so far only considered the variation of crustal thickness and the effects of a single sediment layer. While we do not desire to be exhaustive in our analysis of complex wave-guide structures, it is instructive to consider somewhat more realistic models than used earlier. This is done using the normal-mode method for stratified media, with the waveforms filtered with a 0.3- to 1-Hz bandpass filter, so our synthetics are consistent with those of the finite-difference method.

First, we consider the "average" continental and oceanic models of Meissner (1986, p. 40), simplified to omit layering in the upper mantle. The corresponding continental *P*-wave velocity model is labeled model VI in Table 2. The waveforms calculated for this crustal model (Fig. 11a) have pulse-like L_g for vertical and tangential components with almost the same arrival time. Almost all of the guided wave energy, including fundamental-mode Rayleigh and Love waves, arrives within the L_g window. This is because there is no low-velocity surface layer in this model. The average oceanic model (Meissner, 1986) is shown as model III in Table 2, with the water layer being omitted. The energy distribution in the waveforms calculated for this model (Fig. 11b) is very different from that for the continental model. Because the sediment layer is thin (1 km) and has a very low velocity ($v_s = 1$ km/sec), significant energy is trapped in this layer. As a result, there is a very dispersed, complex fundamental mode signal for this structure. The wave train is very long. While our synthetics do not include attenuation, much of this short-period fundamental mode will be strongly attenuated in actual oceanic crust. There is no impulsive L_g phase in the conventional L_g window for the vertical component. For the *SH* component, there is considerable energy in this window, which involves the first two Love wave overtones.
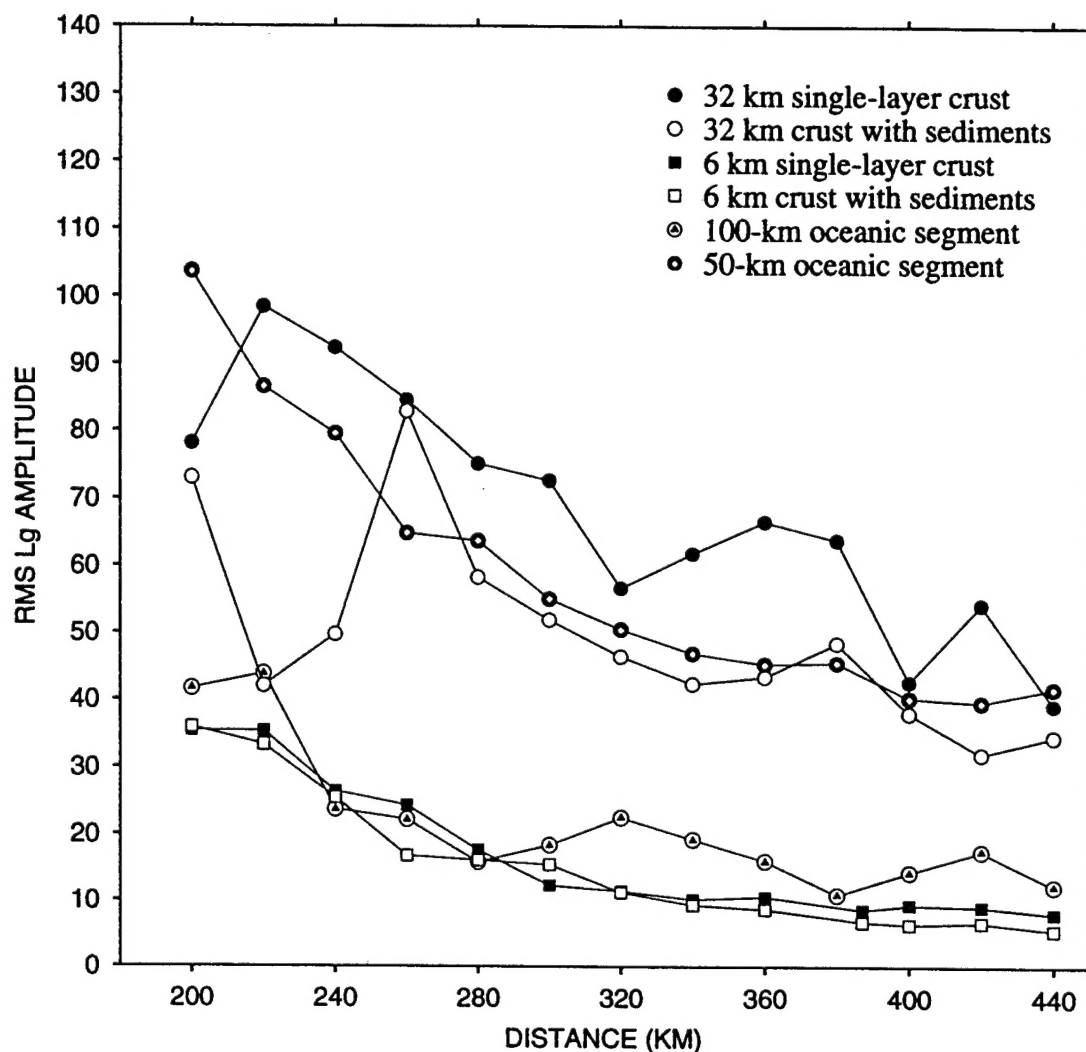
Figure 6. RMS amplitudes in the L_g window for vertical components for various models. The solid symbols are for the layer over half-space models. Circles and squares are for crustal thicknesses of 32 and 6 km. The open symbols are for the corresponding two-layer crustal models with low-velocity surface layers. The results of crustal thinning models are shown with other symbols. The open circles with solid triangles are for the 100-km-long oceanic segment model, measured in 3.7 to 3.2 km/sec window. The solid circles with white diamonds are for the 50-km-long oceanic segment model.

The group velocities are such that this energy does not separate clearly from the fundamental-mode Love wave.

We also considered oceanic crustal models with additional layers, to determine whether more complex structures could enhance oceanic L_g arrivals. Two models for the Pacific Ocean are shown as models IV and V in Table 2. The waveforms computed for these structures are shown in Figures 11c and 11d, identified as Pacific 1 (the four-layer crustal model of Shor *et al.*, 1970) and Pacific 2 (the five-layer crustal model of Hussong, 1972). The dispersion of low-velocity fundamental-mode energy is not as dramatic as for model III. The basic characteristics of the waveforms are similar: there is relatively little energy in the L_g window for the vertical component. However, the energy in this window

for the *SH* component is substantial. The greater relative strength of the Love wave overtone energy in the oceanic crust may be part of the reason why transverse component calculations tend to underpredict L_g blockage, which is usually based on vertical component recordings.

These calculations with more complex crustal models indicate that the number of modes is not simply controlled by the layering of the structure. What is most important is the strength of velocity contrasts in the wave guide, and additional modes can be introduced by including larger internal velocity contrasts. If the deepest boundary has the strongest velocity contrast, the maximum number of normal modes is determined by the phase difference between a ray that has not suffered reflection and a ray that has suffered
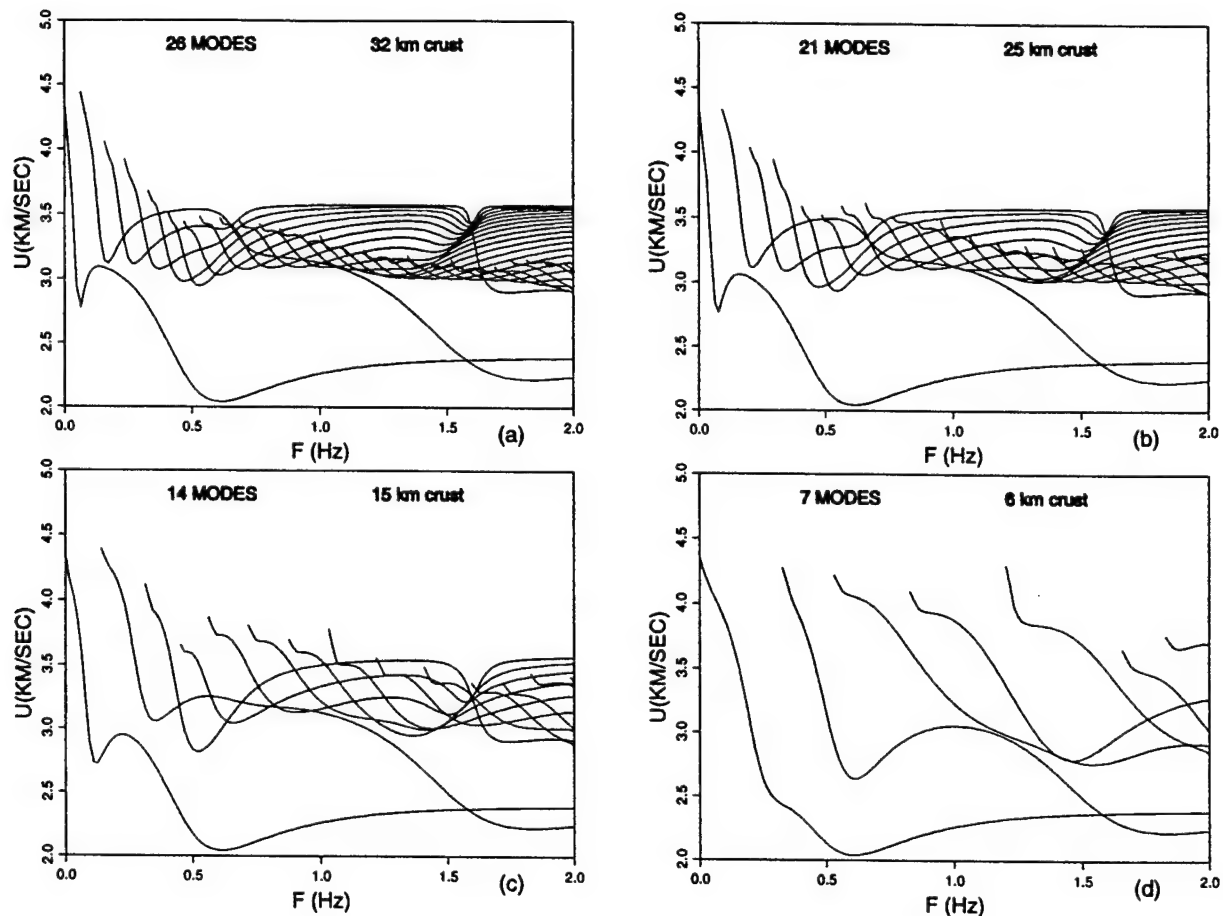
Figure 7.   Dispersion curves for Rayleigh waves in two-layer crustal models with total crustal thicknesses of 32, 25, 15, and 6 km, with each model having a 2-km-thick low-velocity surface layer. Notice the additional Airy phase for the fundamental mode relative to Figure 2.

two total internal reflections. The relation is (Marcuse, 1991, p. 6)

$$(s_2 - s_1)k + \phi_2 + \phi_3 = 2N\pi, \qquad (3)$$

where s_1 is the distance traveled by the direct ray and s_2 is the distance traveled by the reflected ray, k is the wavenumber, $\phi_2 + \phi_3$ is the phase change resulting from the two total reflections, and N is the ordinal number of a normal mode. If the maximum phase difference increases to more than 2π, the number of modes will increase. The addition of extra layers could increase or decrease the maximum phase difference, so it may increase or decrease the number of normal modes. We calculated Love wave phase velocity dispersion curves in the frequency range 0 to 5 Hz for the four oceanic crustal models that we used to generate the synthetic seismograms in Figures 10 and 11. The numbers of crustal layers for each used model are 2, 2, 3, and 5. The corresponding numbers of normal modes are 19, 16, 13, and 15. Thus, there is not a simple increase in number of modes associated with more detailed layering.

The Effect of Crustal Thinning along a Path

In the previous section, we demonstrated that there is a fundamental difference in the modal structure for crust of different thickness, and this prevents stable propagation of L_g over long paths in oceanic structure. However, this leaves unclear the effect of a limited segment of thin oceanic crust along a continental path. We will explore this using the same two-dimensional finite-difference program used for the one-dimensional models considered previously.

We consider a crustal thinning model like that shown in Figure 1c. This model is almost the same as in Figure 1b of Cao and Muirhead (1993), except that our total model is shorter (450 km versus 600 km). The crustal thinning starts 50 km from the left of the model and reaches a minimum thickness of 6 km at 150 km from the left. The thin crust persists for the next 100 km. From 250 to 350 km, the thickness of the crust gradually increases to its original value of 32 km.

The finite-difference synthetics for a 5-km-deep source on the left side of this model are shown in Figure 12. If we compare this figure with Figure 3, the calculations for a uni-
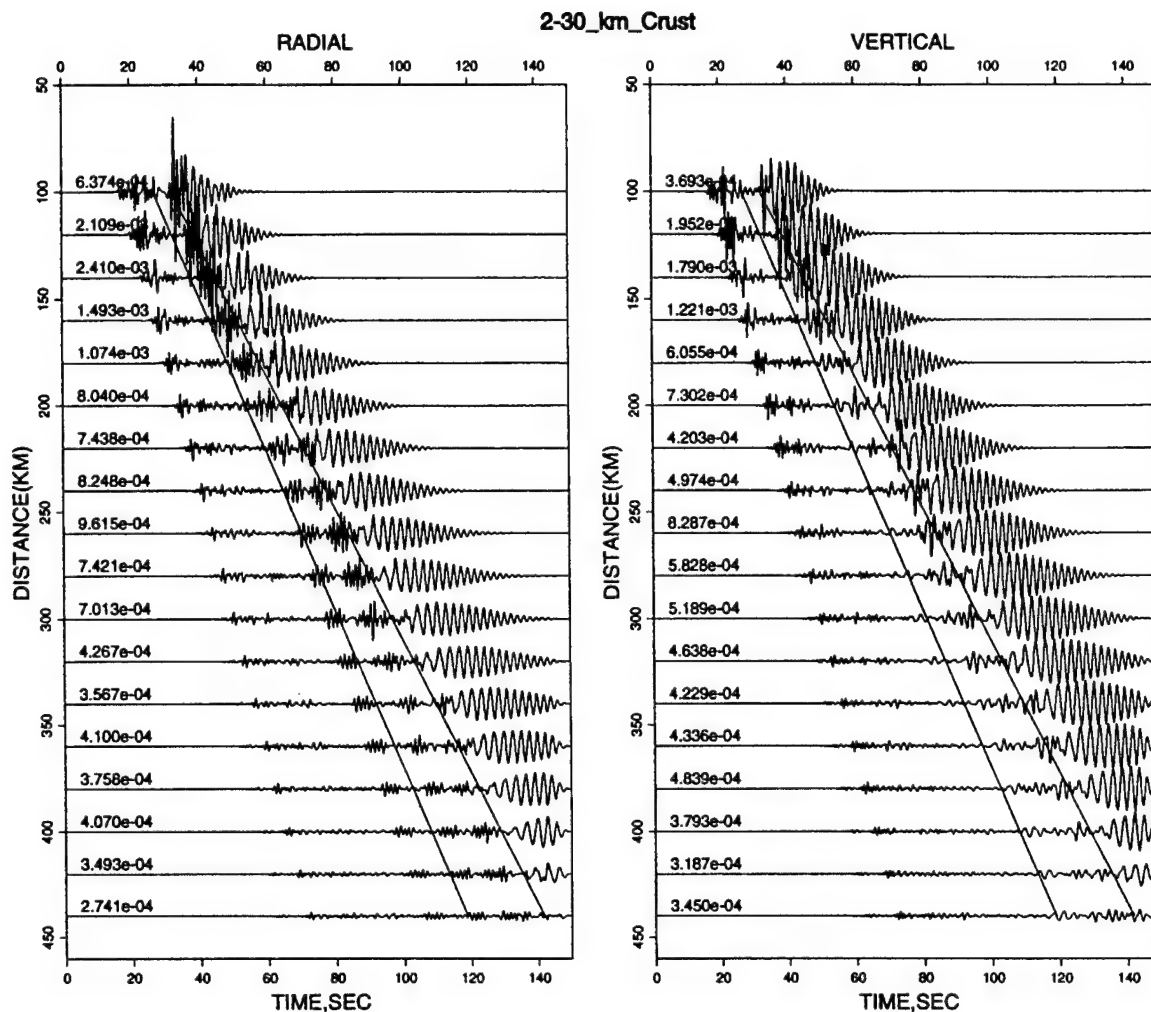
Figure 8.   Synthetic seismograms for a two-layer crustal model with a thickness of 32 km, including a 2-km-thick sediment layer at the surface.

form 32-km-thick crust, and with Figure 5, the calculations for a uniform 6-km-thick crust, we find that the synthetics for the laterally varying structure are somewhat intermediate. There is slightly more energy within the L_g window in the laterally varying crustal model than for the purely oceanic structure, but not as much as for the uniform 32-km-thick model. For this single-velocity crustal model, R_g overlaps the latter part of the L_g window, especially within the stretches of thick crust. One has to carefully recognize the effects of R_g when assessing L_g blockage. If the window is slightly adjusted to avoid the R_g arrival (from 3.7 to 3.1 km/sec to 3.7 to 3.2 km/sec) the L_g amplitude reduction is seen to be stronger. There is about a factor of 4 reduction in the L_g amplitudes relative to the uniform 32-km-thick crust (Fig. 6). Cao and Muirhead (1993) correctly indicate that in a similar model, "higher modes of L_g are muted by the mantle uplift while the fundamental mode is left almost unchanged." However, they proceed to introduce a water column that effectively damps out R_g and indicate that this enhances the blockage of L_g. There is no need to introduce the water

layer to affect L_g, because L_g has been largely disrupted by the crustal thinning alone. The dramatic effect on the overall waveform of scattering or attenuating R_g is easily misinterpreted as an affect on L_g. Using polarization analysis and frequency filtering allows the effects on L_g to be isolated.

As found in the last section, we can separate the L_g and R_g signals by introducing a low-velocity layer at the top of the crust. We consider models like Figure 1d, with a 2-km-thick sediment layer along the entire structure. In the zone of thinned crust, the basalt is 4-km thick. As expected, the R_g waves separate from the L_g window, L_g is blocked, and the resulting seismogram profile is quite similar to Figure 10 (the two-layered oceanic crustal model), so it is not shown here. If the segment of oceanic crust is only 50 km in length, there is much less attenuation of L_g, as shown by the RMS amplitudes in Figure 6 for a corresponding model. Since our results are quite consistent with those of Cao and Muirhead (1993), we do not explore the additional models that they considered, such as including a water layer.

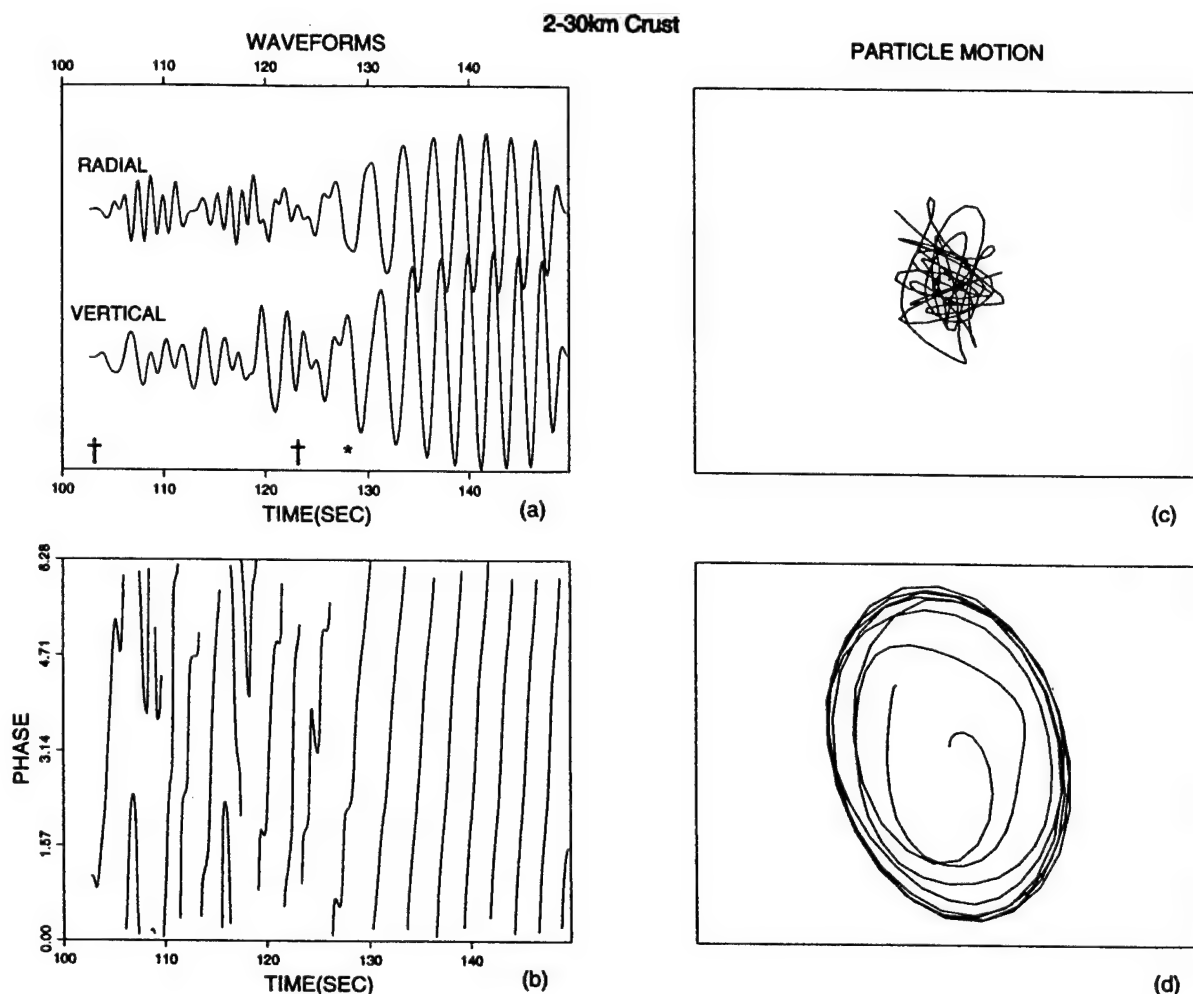It is clear that a 100-km-long segment of oceanic path

Figure 9. Particle motions of surface-wave arrivals for the waveforms at 380-km distance in Figure 8: (a) shows the waveforms of radial and vertical components. The asterisk marks a transition in characteristic particle motion. The L$_g$ window is marked by two † symbols, and (b) is the polarization angle as a function of time. Both (c) and (d) are the particle motions before and after the asterisk. The latter shows almost perfect retrograde ellipse motion (R_g). The early window contains higher modes (L$_g$), characterized by the complex motion.

along an otherwise continental path can block *P–SV* type L$_g$ rather efficiently.

Conclusions

Finite-difference and normal-mode calculations for simple crustal models clearly demonstrate that wave-guide structure, especially the overall thickness of the crust and the presence of any low-velocity surface layer, strongly affect the propagation of regional waves like L$_g$ and R$_g$. For oceanic crust, due to the thin wave guide, the number of overtones is limited to only a few in a given frequency range. As a result, L$_g$ is weak in oceanic structure because the higher-mode Airy phases do not cluster in group velocity to the extent that they do in thicker crust. The contribution of low-order overtones is somewhat higher for *SH* L$_g$ than for *P–*

SV L$_g$, in the 0- to 2-Hz passband. Our calculation shows that for crustal thicknesses in the range 15 to 32 km, L$_g$ amplitudes are rather stable despite the variation of number of modes.

The presence of a low-velocity surface layer has several important effects. Because much of the short-period fundamental mode energy can be concentrated in a low-velocity surface layer, the R_g phase tends to separate from L$_g$ for both oceanic and continental crusts with a sediment layer. Attenuation-free synthetics tend to be dominated by the strong dispersion and large amplitudes of R_g, but actual seismograms tend to show much weaker R_g. This is attributed to combined effects of strong attenuation and scattering in the shallow layer. While the scattered continental R_g phase may contribute to the L$_g$ phase, this will not work very efficiently in an oceanic structure since the overtones are sparse.

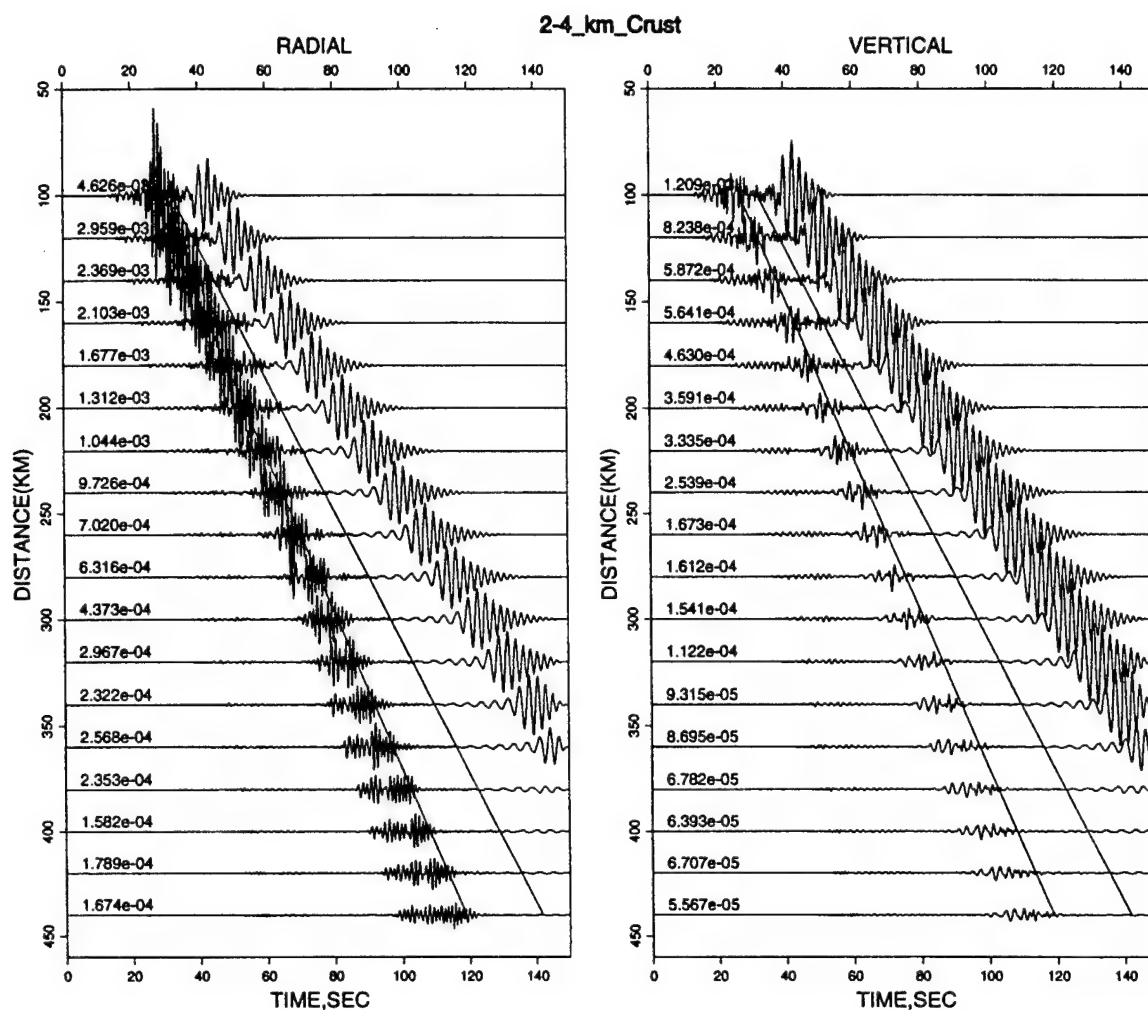Our calculations indicate that the lack of L$_g$ signals for

Figure 10.   Synthetic seismograms for a two-layer crustal model, an overall 6-km crustal thickness including a 2-km sediment layer at the surface. The arrivals within the L_g window are weak. The R_g waves are delayed more for the two-layer model in Figure 5.

oceanic paths is primarily a gross structural effect, intrinsic to the thin wave guide. If frequencies higher than 2 Hz are considered, the presence of more overtones in the oceanic crust does allow L_g to develop, but there have not been very many observations of high-frequency oceanic L_g with which to assess the actual propagation efficiency. Two-dimensional models show that a 100-km-long segment of oceanic crust can reduce L_g amplitudes significantly, whereas a 50-km-long segment does not. This is consistent with previous modeling of $SH\ L_g$ and indicates that there is a minimum path length required for the stabilization of the crustal modal structure, with the 100-km-long path being sufficient to act as a high pass filter on the regional signals.

Acknowledgments

References

Aki, K. and P. G. Richards (1980). *Quantitative Seismology: Theory and Methods,* Vol. I, W. H. Freeman and Co., San Francisco, p. 264.

Birkeland, P. W. and E. E. Larson (1989). *Putnam's Geology.* Oxford University Press, Oxford.

Bostock, M. G. and B. L. N. Kennett (1990). The effect of 3-D structure on L_g propagation patterns, *Geophys. J. Int.* **101,** 355–365.

Brekhovskikh, L. M. (1980). *Waves in Layered Media,* Academic Press, New York.

Campillo, M. (1990). Propagation and attenuation characteristics of the crustal phase L_g, *Pure Appl. Geophys.* **132,** 1–19.

Campillo, M., B. Feignier, M. Bouchon, and N. Bethoux (1993). Attenuation of crustal waves across the Alpine range, *J. Geophys. Res.* **98,** 1987–1996.

Cao, S. and K. J. Muirhead (1993). Finite difference modeling of L_g blockage, *Geophys. J. Int.* **116,** 85–96.
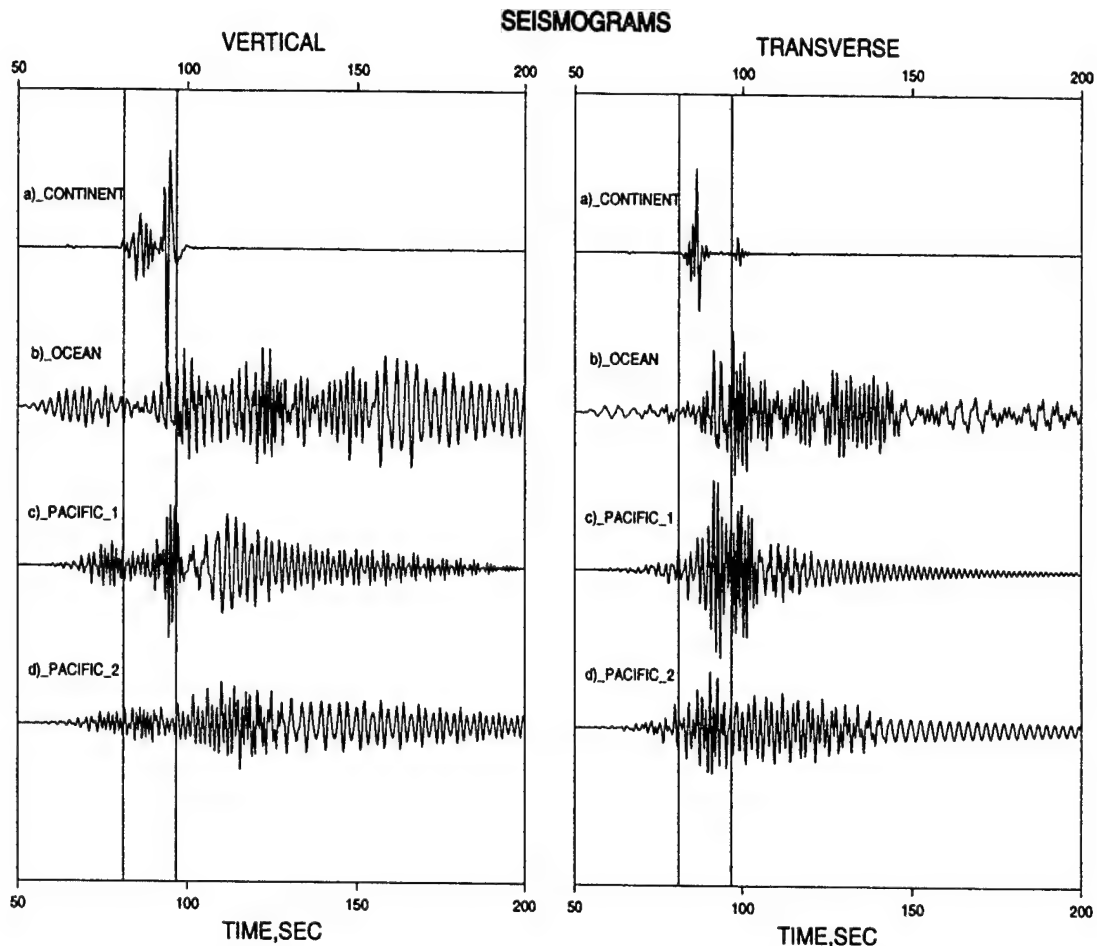
SEISMOGRAMS

Figure 11.   Synthetic seismograms for four crustal models at a distance of 300 km. They are (a) average continental crust from Meissner (1986), corresponding to model VI in Table 2; (b) average oceanic crust from Meissner (1986), corresponding to model III in Table 2; (c) a model for Pacific Ocean from Shor *et al.* (1970), IV in Table 2; and (d) another model for Pacific from Hussong (1972), V in Table 2.

Chazalon, A., M. Campillo, R. Gibson, and E. Garnero (1993). Crustal wave propagation anomaly across the Pyrenean Range—comparison between observations and numerical simulations, *Geophys. J. Int.* **115,** 829–838.

Ewing, M., W. S. Jardetsky, and F. Press (1957). *Elastic Waves in Layered Media,* McGraw-Hill, New York.

Gibson, R. L. Jr. and M. Campillo (1994). Numerical simulation of high- and low-frequency L_g-wave propagation, *Geophys. J. Int.* **118,** 47–56.

Gupta, I. N., W. W. Chan, and R. A. Wagner (1992). A comparison of regional phases from underground nuclear explosions at East Kazakh and Nevada test sites, *Bull. Seism. Soc. Am.* **82,** 352–382.

Herrmann, R. B. and C. Y. Wang (1985). A comparison of synthetic seismograms, *Bull. Seism. Soc. Am.* **75,** 41–56.

Hussong, D. M. (1972). Detailed structural interpretations of the Pacific oceanic crust using ASPER and ocean-bottom seismometer methods, *Ph.D. Dissertation,* 165 pp., University of Hawaii.

Israelson H. (1992). RMS L_g as a yield estimation in Eurasia, Final Report for AF Phillips Laboratory, Hanscom AFB, MA 01731–5000.

Kennett, B. L. N. (1986). L_g waves and structural boundaries, *Bull. Seism. Soc. Am.* **76,** 1133–1141.

Knopoff, L, R. G. Mitchel, E. G. Kausel, and F. Schwab (1979). A search for the oceanic L_g phase, *Geophys. J. Roy. Astr. Soc.* **56,** 211–218.

Knopoff, L., F. Schwab, and E. Kausel (1973). Interpretation of L_g, *Geophys. J. R. Astron. Soc.* **33,** 389–404.

Kock, W. E. (1965). *Sound Waves and Light Waves,* Anchor Books, New York.

Kovach, R. L. and D. L. Anderson (1964). Higher mode surface waves and their bearing on the structure of the Earth's mantle, *Bull. Seism. Soc. Am.* **54,** 161–182.

Marcuse, D. (1991). *Theory of Dielectric Optical Waveguides,* Academic Press, New York.

Maupin, V. (1989). Numerical Modeling of L_g wave propagation across the North Sea Central Graben, *Geophys. J. Int.* **99,** 273–283.

Meissner, R. (1986). *The Continental Crust,* Academic Press, New York.

Nuttli, O. W. (1986). Yield estimates of Nevada test site explosions obtained from seismic L_g waves, *J. Geophys. Res.* **91,** 2137–2151.

Panza, G. F. and G. Calcagnile (1975). L_g, L_i and R_g from Rayleigh modes, *Geophys. J. Roy. Astr. Soc.* **40,** 475–487.

Press, F. and M. Ewing (1952). Two Slow Surface Waves across North America, *Bull. Seism. Soc. Am.* **42,** 219–228.

Regan, J. and D. G. Harkrider (1989a). Numerical modelling of *SH* L_g waves in and near continental margins, *Geophys. J. Int.* **98,** 107–130.

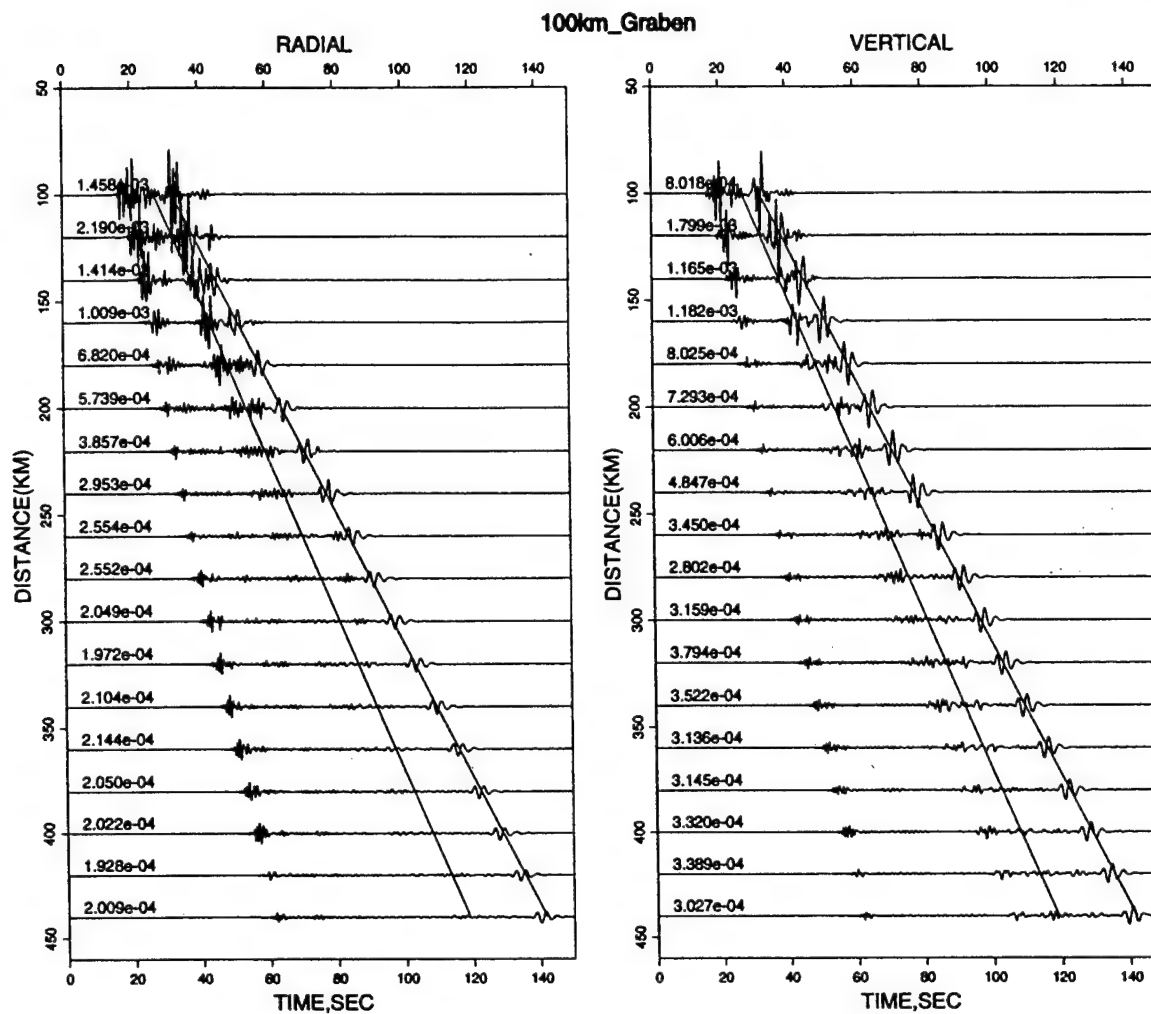Regan, J. and D. G. Harkrider (1989b). Seismic representation theorem

Figure 12.   Synthetic seismograms for a one-layer crust model with variable crustal thickness as shown in Figure 1c. The crust is initially 32-km thick, then it begins to thin starting at 50 km from the left, becoming 6-km thick by 150 km from the left. This thickness persists from 150 to 250 km, then the crust begins to thicken from 250 to 350 km, recovering a 32-km thickness by 350 km.

coupling: synthetic SH mode sum seismograms for non-homogeneous paths, *Geophys. J. Int.* **98**, 429–446.

Shor, G. G. Jr., H. W. Menard, and R. W. Raitt (1970). Structure of the Pacific basin, in *The Sea,* A. E. Maxwell (Editor), vol. 4, part 2, Wiley-Interscience, New York.

Xie, X. B. and T. Lay (1994). The excitation of L_g waves by explosions: a finite-difference investigation, *Bull. Seism. Soc. Am.* **84**, 324–342.

Xie, X. B. and Z. X. Yao (1988). P-SV wave responses for a point source in two-dimensional heterogeneous media: finite-difference method, *Chinese J. Geophys.* **31**, 473–493.

Zhang, T. and T. Lay (1994a). Analysis of short-period regional phase path effects associated with topography in Eurasia, *Bull. Seism. Soc. Am.* **84**, 119–132.

Zhang, T. and T. Lay (1994b). Effects of crustal structure under the Barents and Kara seas on short-period regional wave propagation for Novaya Zemlya explosions: empirical relations, *Bull. Seism. Soc. Am.* **84**, 1132–1147.

Zhang, T., S. Y. Schwartz, and T. Lay (1994). Multivariate analysis of waveguide effects on short-period regional wave propagation in Eurasia and its application in seismic discrimination, *J. Geophys. Res.* **99**, 21929–21945.

Institute of Tectonics
University of California
Santa Cruz, California 95064
   (T.-R.Z., T.L.)

Variation of Regional Seismic Discriminants with Surface Topographic Roughness in the Western United States

by Tian-Run Zhang, Thorne Lay, Susan Schwartz, and William R. Walter

Abstract Regional distance P and S waves behave differently with propagation distance due to complex elastic and anelastic effects in the crustal wave guide and uppermost mantle. It is well recognized that seismological discriminants based on P/S ratios or individual phase spectral ratios must be corrected for regionally dependent path effects for successful discrimination to be achieved. Such corrections usually involve only distance-dependent decay, parameterized to account for geometric spreading and attenuation factors averaged over some geographic region. However, large scatter persists in distance-corrected discriminants, which degrades their performance, and strategies are needed to further reduce the scatter by accounting for individual path variability. We demonstrate that characterizing some of the path variability by the readily measured surface topographic roughness along each path allows reduction of the scatter in some regional discriminants. P_g/L_g and P_n/L_g ratios and P_g, P_n, and L_g low-frequency/high-frequency spectral ratios for 80 earthquakes in the Western United States recorded at four stations of the Livermore NTS Network are analyzed for path effects. While all of these discriminants display distance dependence, $\log P_g/L_g$ is also found to be significantly correlated with average surface roughness along each path. The correlation is emphasized when the product of distance and roughness is used as an independent variable, and the data in the frequency range 1 to 6 Hz have the strongest trends. Corrections based on the correlations with distance and roughness can reduce the variance of the $\log P_g/L_g$ discriminant by 22 to 25% in the 2- to 4-Hz band. Log P_n/L_g and individual phase spectral ratios have stronger distance dependence than $\log P_g/L_g$, but the correlation with surface roughness is weak for those measurements. It appears that interchange of P_g and L_g energy that reverberates in the crust accounts for the sensitivity to the gross wave-guide properties that are manifested in the surface roughness parameterization. The results support the concept of pursuing path corrections beyond purely range-dependent trends.

Introduction

Amplitude ratios and spectral shapes of various types of P and S waves recorded at regional distances have been explored as potential discriminants for identifying seismic sources for decades (e.g., Pomeroy *et al.,* 1982). Lateral variations in the elastic and anelastic structure of the crust and uppermost mantle produce regional differences in the amplitude and spectral behavior of regional phases, and the associated path effects must be accounted for both to reduce the scatter in the discriminants and to transport discriminant behavior from one region to another (e.g., Baumgardt and Young, 1990; Taylor and Denny, 1991; Lynnes and Baumstark, 1991; Bennett *et al.,* 1992; Kennett, 1993; Baumgardt and Der, 1994). Reducing the scatter in promising regional seismic discriminants has thus become a major element in strategies for monitoring a comprehensive test ban treaty, because many regions with no prior nuclear explosions must be monitored. It is much more likely that a surreptitious nuclear event will be detected (i.e., recognized as an outlier event) if the earthquake population has a tightly defined range of discriminant behavior (Fisk, 1994).

Given the complex suite of factors that influence seismic radiation from explosion and earthquake sources, and the great heterogeneity in global crustal properties, it is not clear that any single regional phase discriminant will perform well in all regions. For example, one of the most promising discriminants is based on high-frequency ratios of P_g/L_g, yet this is a fairly poor discriminant in the Western United States (e.g., Murphy and Bennett, 1982; Bennett and Murphy,

1986; Taylor *et al.,* 1988, 1989; Lynnes and Baumstark, 1991; Walter *et al.,* 1995). Low-frequency/high-frequency L_g spectral ratios work fairly well in the Western United States but do poorly in areas with more stable continental crust (e.g., Baumgardt and Young, 1990; Lynnes and Baumstark, 1991). Regional path effects contribute to the variability of discriminant performance, but well-controlled studies with common paths for explosions and earthquakes (e.g., Bennett *et al.,* 1992; Walter *et al.,* 1995) indicate that source radiation effects related to source medium properties also produce scatter that degrades the discriminants (Taylor and Denny, 1991; Walter *et al.,* 1995). While some effects, such as radiation pattern variations, may be reduced by combining discriminants for multiple stations or using several types of discriminants simultaneously, such strategies may fail to overcome systematic regional path effects.

Most efforts to account for path effects on regional phases have empirically estimated the geometric spreading and attenuation terms for each relevant phase using frequency-dependent variations with propagation distance. A wide range of procedures are available for estimating the distance-dependent corrections, including simple regressions of discriminant measures as a function of distance (e.g., Taylor *et al.,* 1988) or smoothly combining discriminant measures from station pairs at different distances to reduce scatter from source spectral differences (e.g., Chun *et al.,* 1987; Baumgardt and Der, 1994). When sufficient numbers of observations are available for a given region, applying these corrections should be a standard practice, as there are sound theoretical reasons for the wave-field behavior. Applications have demonstrated that significant regional differences in the corrections are found. But this process is not always adequate to account for propagation effects. The common occurrence of effects such as L_g blockage on certain paths will enhance scatter in a discriminant population that usually cannot be reduced by smooth, regionally averaged amplitude decay trends. Systematic mapping out of regions and paths on which total blockage occurs is essential, particularly for areas with little monitoring history. This effectively can alert the discrimination algorithm to a source of possible failure. Somewhat more difficult is the development of individual path corrections for those propagation effects other than total blockage that are not accounted for by regional amplitude-distance curves. This is required to tighten up the discriminant population.

The L_g phase is prominent in most regional discriminants, in part due to its intrinsic stability imparted by the complex scattering of multiple S reflections in the crust and in part due to its typically good signal-to-noise ratio. In most continental regions, L_g is the largest phase in regional waveforms. While amplitude-distance curves can account for much of the typical variation of L_g phases, wave-guide irregularities, often involving very localized portions of the path, can strongly affect the phase on a path-by-path basis. For example, abrupt thinning of the crust can weaken the L_g phase (see Zhang and Lay, 1995, for a discussion), while

sedimentary basins or mountain ranges on the path can partially or totally block the phase (e.g., Baumgardt, 1990; Zhang and Lay, 1994b). Independent knowledge of the path properties may allow these effects to be accounted for; although at present, we are constrained to empirical approaches since it is very difficult to quantitatively predict any of the wave-guide effects. Of course, our knowledge of crustal properties is very limited, and we have at best rudimentary models for the variable crustal wave guide on any given path, even for use in empirical approaches. Nonetheless, it may be possible to use observable parameters such as surface topography and sediment basin distribution as measures that characterize some portion of the wave-guide heterogeneity (e.g., Baumgardt, 1990; Zhang and Lay, 1994a, 1994b; Zhang *et al.,* 1994).

In addition to L_g, P_g and P_n are important regional phases that may be influenced by wave-guide complexity. P_g can be viewed as guided P waves within the crust (Haskell, 1966), and one may expect it to have some similarities to L_g in terms of its sensitivity to geometric spreading, attenuation, and wave-guide irregularities. P_n can involve some energy transiting the crust more than once, but it should generally be sensitive to different crustal characteristics than P_g and L_g. In this article, we seek to establish whether any of the common regional discriminants using P_n, P_g, and L_g phases correlate with localized path properties parameterized in terms of mean variance (roughness) of the surface topography on the associated path. Topography may influence P_g and L_g propagation both directly as a source of scattering and indirectly as a manifestation of wave-guide structure and thermal variations. This approach is motivated by the results of Zhang and Lay (1994a), who observed correlations of log P/L_g and log S_n/L_g with RMS surface roughness for narrow band, hand-digitized data at upper mantle distances from Eurasian explosions. That study was limited to frequencies less than 3 Hz, and most of the data were from upper mantle distances ($>$1200 km), so the P waves were not purely crustal phases. A recent study by Baumgardt and Der (1994) has shown that path properties like topography may produce strong effects on regional phases at frequencies greater than 3 Hz for some paths in central Eurasia. We analyze broadband digital data for earthquakes in the Western United States, where large scatter in regional discriminants is observed, and assess whether empirical relationships with the most observable of path properties, surface elevation and roughness, hold promise for reducing the scatter in regional discriminants.

Data

We analyze vertical-component seismograms from earthquakes (using the data set of Mayeda and Walter, 1995) in the Western United States recorded at four stations of the broadband Livermore NTS Network to determine path effects on regional discriminants. Figure 1 shows the event and station locations, with our primary path coverage being
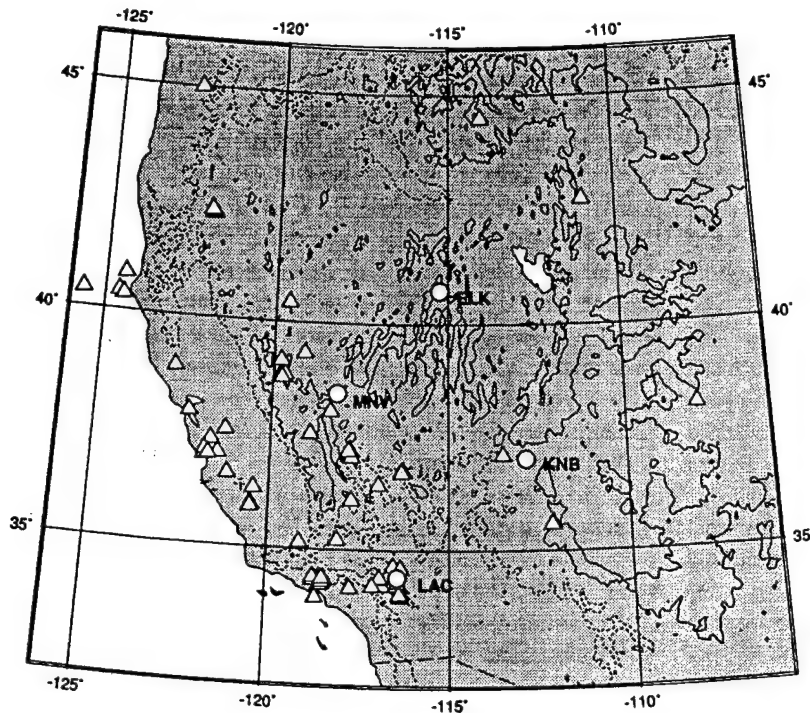
Figure 1. Map showing the locations of earthquakes (triangles) and LLNL stations (circles) used in this study. The surface topography is contoured, with dashed lines indicating the 1000-m elevation, and solid lines, the 2000-m elevation.

in California and the southern basin and range. The events include most of the magnitude 4 and larger events since 1990, which provides fewer paths in the basin and range than sampled by older data sets used by Taylor *et al.* (1989) and Lynnes and Baumstark (1991). We inspected signals from a total of 127 events, retaining those 80 events with good signal-to-noise level and uniform sample rates. Waveforms from distances less than 100 km are omitted, and our most distant observations are about 1200 km from the sources. A total of 193 broadband waveforms are used in calculation of P_g/L_g and P_g and L_g spectral ratios after elimination of waveforms with low signal-to-noise ratios, clipping, glitches, telemetry dropout, or other problems. P_n does not develop as well as P_g in the Western United States, reducing the data to 148 waveforms used in the calculation of P_n/L_g and P_n spectral ratios. The small number of useable recordings for each event precludes any attempt to determine source corrections, but it is generally believed that source corrections are very unreliable for regional phases that reverberate in the wave guide. Following Walter *et al.* (1995), the P_n window begins at the onset of the signal and ends at the start of P_g. The P_g window runs from the onset of a group velocity of 6.0 km/sec to a group velocity of 5.0 km/sec. The L_g window is between group velocities of 3.6 and 3.0 km/sec. For each phase, the vertical-component velocity seismograms were tapered with a 10% cosine taper, fast-Fourier transformed, and a log-averaged spectral amplitude calculated over six frequency bands: 0.3 to 1 Hz, 1 to 2 Hz, 2 to 4 Hz, 4 to 6 Hz, 6 to 8 Hz, and 8 to 10 Hz. Instrument correction is not necessary in our calculation, because for most data, we use very broadband channels for which the instrument response

is flat to velocity over the passband used, and our primary results involve ratios of phases at a given frequency. For low-frequency/high-frequency discriminants, we restrict our data to those recordings with very broadband response. Horizontal-component records are available for many of the events but were not used since they generally have lower signal quality.

The Western United States is tectonically active, and path properties are expected to be quite heterogeneous. In particular, the topographic relief is strong, as illustrated in Figure 1. It is only 128 km between the lowest elevation in Death Valley (-86 m) and the highest peak of the Sierra Nevada Mountains (4418 m). However, we do not observe total L_g blockage in our data set, even on paths traversing the Sierra Nevada. This does not preclude partial blockage, or systematic regional patterns of greater or lesser propagation efficiency, as detected by Lynnes and Baumstark (1991). L_g is the largest amplitude phase in all of our waveforms, except for four, which have relatively large P_g, and those are all at distances less than 200 km. We use topographic data from database TOPO30 (a 30-sec point elevation file developed by the Defense Mapping Agency Topographic Center and the National Telecommunications and Information Administration), with the profile of topography between each source and station being extracted using the GMT software of Wessel and Smith (1991). This data set provides about 1 km spatial sampling, so there is some potential for aliasing of topographic effects for the highest frequency signals considered here, but this is much better sampling than has been used in previous studies of topographic effects (e.g., Zhang *et al.*, 1994).
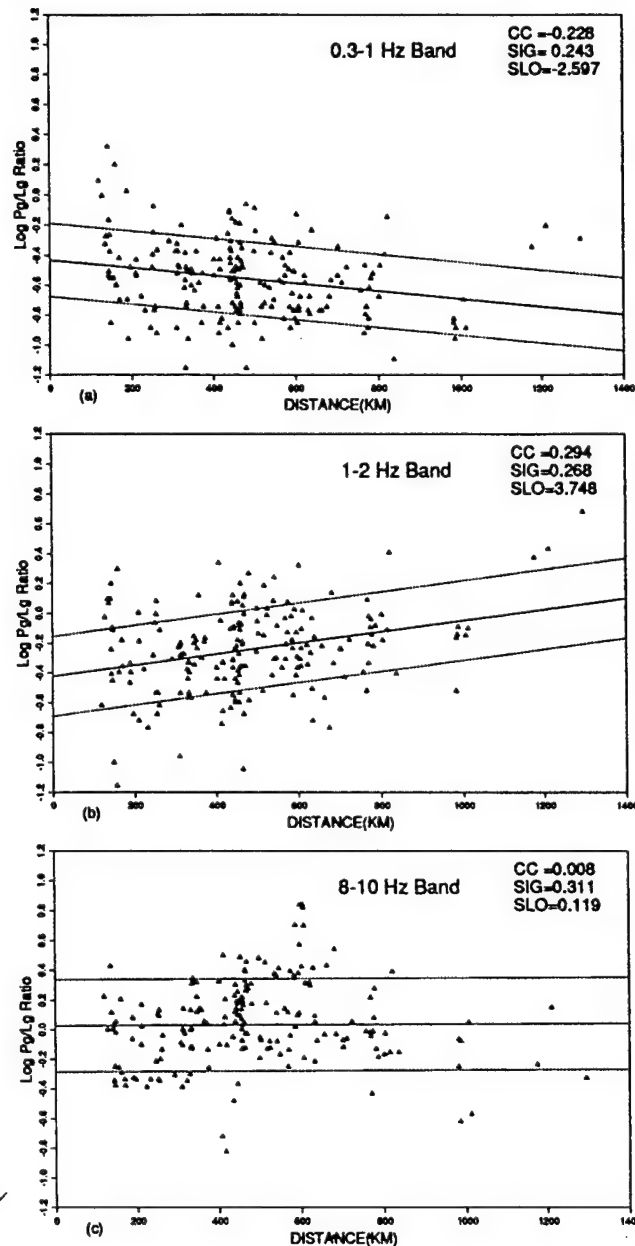
Figure 2. Log (P_g/L_g) as a function of distance in various frequency bands: (a) 0.3 to 1.0 Hz, (b) 1.0 to 2.0 Hz, (c) 8.0 to 10.0 Hz. CC indicates the correlation coefficient, SIG is the standard deviation of the regression, and SLO is the slope of the regression line.

Table 1
(a) Regression Results for P_g/L_g with Distance

Band (Hz)	Slope ($\times 10^4$)	S.E. ($\times 10^4$)	C.C.	CD
0.3–1.0	−2.60	0.80	−0.23	0.0521
1.0–2.0	3.75	0.88	0.29	0.0863
2.0–4.0	3.84	0.73	0.35	0.1255
4.0–6.0	3.40	0.86	0.27	0.0751
6.0–8.0	2.02	0.98	0.15	0.0218
8.0–10.0	0.12	1.02	0.01	0.0001

(b) Regression Results for P_g/L_g with Roughness

Band (Hz)	Slope	S.E.	C.C.	CD
0.3–1.0	−0.089	0.086	−0.08	0.0063
1.0–2.0	0.149	0.090	0.12	0.0143
2.0–4.0	0.326	0.073	0.31	0.0937
4.0–6.0	0.482	0.081	0.40	0.1568
6.0–8.0	0.400	0.093	0.30	0.0890
8.0–10.0	−0.033	0.100	−0.02	0.0006

(c) Regression Results for P_g/L_g with Roughness $\times$ Distance

Band (Hz)	Slope ($\times 10^4$)	S.E. ($\times 10^4$)	C.C.	CD
0.3–1.0	−2.72	1.16	−0.17	0.0282
1.0–2.0	5.30	1.26	0.29	0.0852
2.0–4.0	7.17	0.99	0.47	0.2162
4.0–6.0	7.56	1.15	0.43	0.1837
6.0–8.0	4.57	1.37	0.23	0.0551
8.0–10.0	−1.27	1.45	−0.06	0.0040

Slope is slope of the regression line. S.E. is standard error of the slope. C.C. is correlation coefficient. CD is coefficient of determination.

Path Effects for P_g/L_g Phase Ratios

We consider both the distance behavior and path roughness behavior of P_g/L_g ratios at different frequencies. Since we lack reliable theoretical models for the range dependence of the separate phases, and attenuation and geometric spreading effects are difficult to separate, we seek a simple general distance dependence. Correction for the net propagation effects requires only a reliable knowledge of the frequency-dependent distance dependence of the ratio, not the separate

behavior of the different phases. For parameterizing the distance decay, several different functional forms have been proposed, such as the power law (Δ^γ) and exponential ($e^{\gamma\Delta}$) forms. Sereno (1991) used the power-law form, while Baumgardt and Der (1994) suggest that the exponential form be used for representing the distance dependence. In fact, within a limited range of distances, these two forms give about equal variance reduction, whereas the relatively large distance range spanned by our data is slightly better parameterized with an exponential model. Following Baumgardt and Der (1994), we use an exponential form, but we take 10 as the exponential base, since we lack an explicit functional form appropriate for effects of wave-guide irregularity. We assume

$$R(\Delta) = 10^{\gamma\Delta}, \qquad (1)$$

where R is the P_g/L_g ratio, Δ is the distance in km, and γ is the slope of the empirical regression line between $\log R$ and Δ. The choice of base 10 in (1) has little effect on our results, given the large scatter in the data.

The distance dependence of P_g/L_g for the frequency band 0.3 to 1 Hz for our Western U.S. paths is shown in Figure 2a. In this passband, γ is negative, which is consistent

with the strong geometrical spreading effect for low-frequency P_g relative to L_g (Campillo *et al.*, 1984), but the overall trend is quite weak, as noted by Taylor *et al.* (1989) for data in the Basin and Range. Most of the waveform energy is within this low-frequency band, so the unfiltered data give a similar pattern. There appears to be some minor structure in the data near 500 km, but overall, a simple exponential distance dependence adequately represents what little trend is present.

In the passband 1 to 2 Hz, γ is slightly positive (Fig. 2b), and it remains positive up through the 8 to 10-Hz passband (Fig. 2c). An increase of this slope with frequency was noted by Lynnes and Baumstark (1991). We find that the slope has a substantial jump around 1 Hz, where it changes from negative to positive, but it begins to decrease beyond about 5 Hz, as shown in Table 1. Given the strong attenuation present in the western United States, there is concern about the signal-to-noise ratio at frequencies above 5 Hz. Inspection of the signal levels indicates that for many signals, there is reasonable high-frequency energy, but there is no doubt that the reliability of any trends with distance or other path parameters must diminish as a result of decreasing signal-to-noise ratios. The positive values for γ at frequencies above 1 Hz are most readily attributable to strong attenuation effects on short-period L_g offsetting the geometric effects on P_g. This behavior does show some abrupt transition near a distance of 400 km, and if only closer distance data are considered, the ratios tend to decrease slightly with distance at all frequencies for the range 150 to 400 km. McCormack *et al.* (1995) found slight negative slopes in the same limited distance range for dense profiles in western Nevada and estimated attenuation parameters from this behavior. The abrupt increase in ratios near 400 km suggests that such attenuation parameters cannot be extended to ratios at larger ranges, and it appears that the geometric spreading is more complicated than the smooth power-law decay that is usually assumed.

We now consider the path effects characterized by roughness (as measured by the RMS value) of the surface topography along each path. The RMS path roughness is one of many characterizations of the topography that can be considered, but simple gross path averages, such as average elevation or average elevation gradient, have high correlations with roughness (e.g., Zhang and Lay, 1994a), and it is not possible to uniquely identify an optimal measure. We use the RMS value since it is easily computed, robust, and it works as well as any of the measures that we considered. Log R correlates with RMS surface roughness about as strongly as with distance. The behavior of the 2 to 4-Hz band is shown in Figure 3, with the correlations with distance (Fig. 3a) and surface roughness (Fig. 3b) displaying similar overall trends. The two independent variables, distance and roughness, have a correlation coefficient of only 0.08, so these are not redundant effects.

One can proceed to define corrections based on these separate parameters, but we explore whether a combination
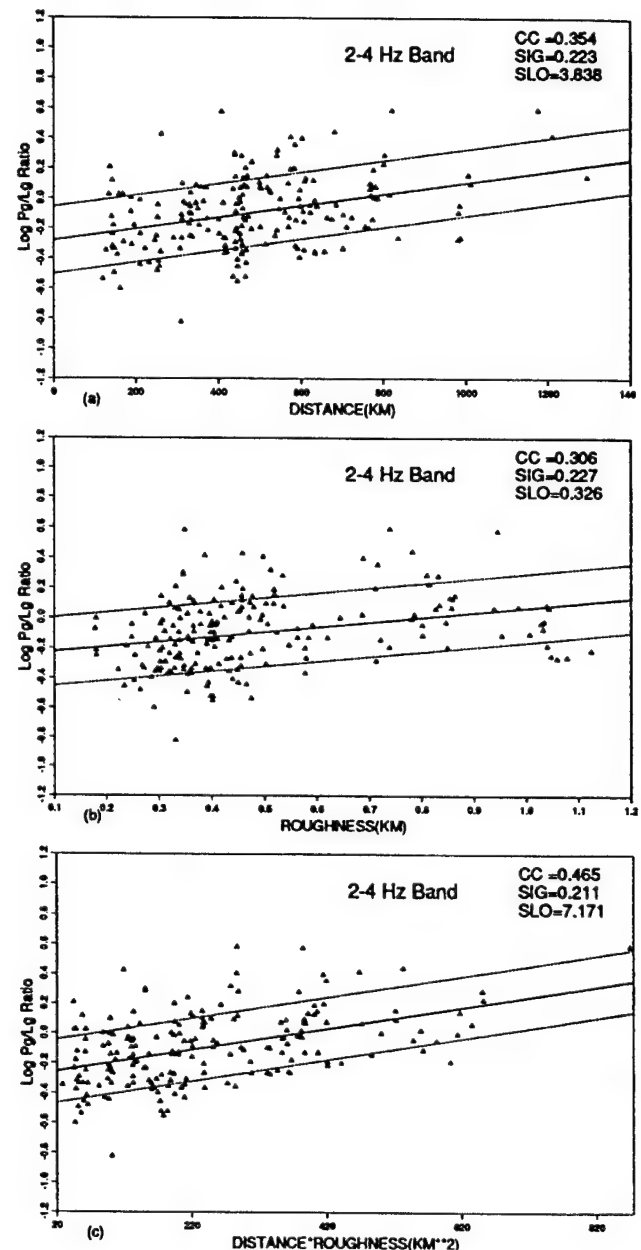

Figure 3.   Log (P_g/L_g) as a function of (a) distance, (b) roughness, and (c) distance $\times$ roughness for Western U.S. data in the frequency band 2 to 4 Hz.

of parameters is superior. Multiple-regression analysis on linear combinations of distance and roughness parameters gave almost identical results to the separate inversions, a result of the low correlation of those parameters, so we explored models in which distance and roughness are combined. We consider an end-member case in which the distance behavior of P_g and/or L_g is controlled by path roughness. As a simple assumption, we let γ be a linear function of roughness; i.e.,

$$\gamma(\mu) = a\mu, \qquad\qquad (2)$$
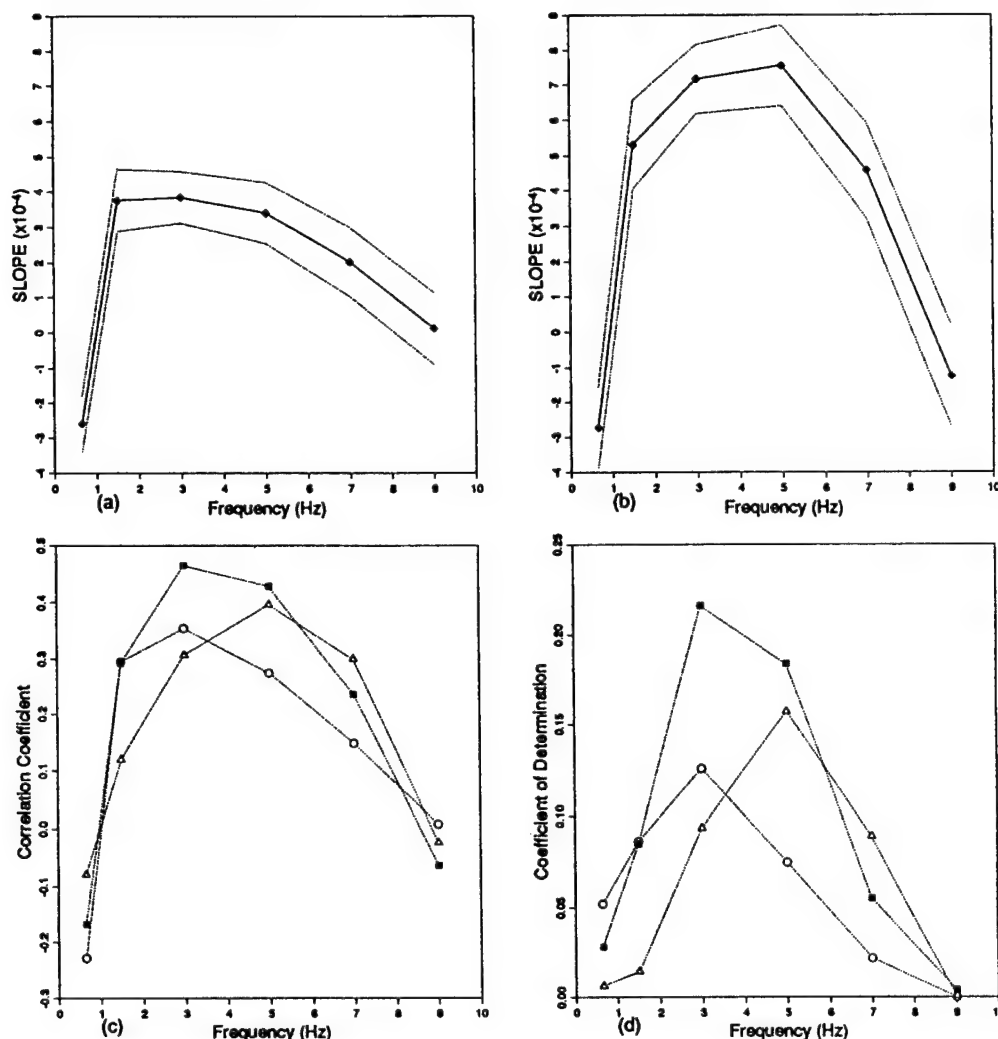
Figure 4. Summary of the regression results of log (P_g/L_g) with distance, roughness, and distance × roughness. (a) Slopes of the regression lines of log (P_g/L_g) with distance in various frequency bands. The dashed lines indicate the standard error of each slope estimate. (b) Slopes of regressions on distance × roughness. The dashed lines indicate the standard error of each slope estimate. (c) The correlation coefficients of log (P_g/L_g) with distance (circles), roughness (triangles), and distance × roughness (squares). (d) The coefficients of determination of the regressions of log (P_g/L_g) with distance (circles), roughness (triangles), and distance × roughness (squares).

where μ indicates RMS topographic roughness, and a is a constant coefficient. Then (1) becomes

$$R(\Delta) = 10^{a(\mu\Delta)}. \tag{3}$$

Figure 3c shows the correlation of log R with the product of distance and roughness, $\mu\Delta$. The correlation coefficient is higher than that for each variable separately. The variable $\mu\Delta$ can also reduce more scatter in the data than the separate terms in this frequency band. It appears that the distance dependence, γ, not only is region dependent but also is dependent on the specific path in a given region. This may partially explain the complexity of log R in the Western United States. We also considered more general forms for γ

such as $\gamma = \beta + a\mu$, using multivariate regression to evaluate both β and a from the following equation:

$$\log R = \beta\Delta + a\mu\Delta \tag{4}$$

However, Δ and $\mu\Delta$ are so strongly correlated (correlation coefficient >0.8) that the estimation of both a and β is not reliable due to collinearity. From previous studies, we know that the distance dependence is usually weak in relatively flat areas like Scandinavia, so that assuming β is a small coefficient generally should not introduce much error.

Fisk (1994) expresses the distance-dependence exponent as a linear function of frequency $\gamma = a + bf$, but this does not characterize the behavior of our data, as summa-

rized in Figure 4a, very well, except for frequencies above 1 Hz. In addition, our observations are actually not very well characterized by straight lines at each frequency. The variance in the data is very large and increases with frequency. The lack of any distance dependence for the 6 to 8-Hz band may simply reflect the overwhelming effects of strong small-scale scattering of both phases and the low signal-to-noise ratio.

The slopes (a) for regressions in various frequency bands of log R on $\mu\Delta$ are summarized in Figure 4b, while Figure 4c shows the correlation coefficients for regressions on distance, roughness, and distance $\times$ roughness in each frequency band (see also Table 1). The correlation of log R with distance peaks at 2 to 4 Hz (circles), while correlation with roughness has a maximum at 4 to 6 Hz (triangles). The correlation with distance $\times$ roughness is significantly higher than that with distance in three bands spanning 2 to 8 Hz.

The objective of all path corrections is to reduce the variance in the discriminant population so that subtle source effects can be detected. Figure 4d illustrates the variations of the coefficient of determination (CD), which gives the variance reduction achieved by the regression on each independent variable (see Zhang *et al.*, 1994). The variance of the uncorrected and corrected values of log R are plotted in Figure 5 (lower set of curves) to further illustrate the effect of path corrections. The variances are reduced to variable extent at different frequencies for each parameter. In the frequency range 2.0 to 6.0 Hz, log R shows the greatest distance and roughness dependence, and the largest variance reduc-

tions (up to 22%) upon path correction. On the whole, the product of distance and roughness explains more variability than either distance or roughness alone in the passband 1 to 8 Hz.

The foregoing analysis utilized measurements with no station corrections, and it is important to assess whether individual station behavior controls any of the trends seen in the data. We considered each station separately, finding that all four stations exhibit similar behavior with distance, roughness, and distance $\times$ roughness, with the exception of LAC, for which the range in path roughness is too limited to define a trend. The correlations and variance reduction for each path variable vary with frequency in a similar way to Figure 4, although some individual stations (e.g., MNV and ELK) have stronger trends with distance than does the composite data set. While the commonality of the trends gives us confidence that the path effects are real, there are some baseline shifts in the individual station behavior that suggest frequency-dependent site effects. We estimated the site effects by comparing log R observations for each station relative to those for the best-sampled station, MNV, fitting a

Figure 5. Summary of the reduction of the variances of log (P_g/L_g) and log (P_n/L_g) data after correction for distance, roughness, and distance $\times$ roughness. Filled circles indicate the variance of log (P_g/L_g) (lower group) and log (P_n/L_g) (higher group) before correction. Squares indicate the variance after the correction just for distance. Triangles indicate the variance just corrected for roughness. Diamonds indicate the variance corrected for distance $\times$ roughness.

Table 2

(a) Regression Results for P_g/L_g with Distance after Station Correction

Band (Hz)	Slope ($\times 10^4$)	S.E. ($\times 10^4$)	C.C.	CD
0.3–1.0	−1.59	0.79	−0.14	0.0205
1.0–2.0	4.79	0.81	0.39	0.1534
2.0–4.0	4.49	0.69	0.43	0.1810
4.0–6.0	3.73	0.81	0.32	0.0996
6.0–8.0	2.55	0.92	0.20	0.0382
8.0–10.0	0.49	0.99	0.04	0.0013

(b) Regression Results for P_g/L_g with Roughness after Station Correction

Band (Hz)	Slope	S.E.	C.C.	CD
0.3–1.0	−0.187	0.078	−0.17	0.0296
1.0–2.0	0.061	0.087	0.05	0.0026
2.0–4.0	0.286	0.072	0.28	0.0762
4.0–6.0	0.450	0.077	0.39	0.1505
6.0–8.0	0.365	0.089	0.29	0.0816
8.0–10.0	−0.051	0.097	−0.04	0.0014

(c) Regression Results for P_g/L_g with Roughness $\times$ Distance after Station Correction

Band (Hz)	Slope ($\times 10^4$)	S.E. ($\times 10^4$)	C.C.	CD
0.3–1.0	−2.53	1.13	−0.16	0.0256
1.0–2.0	5.62	1.19	0.32	0.1044
2.0–4.0	7.50	0.94	0.50	0.2495
4.0–6.0	7.71	1.08	0.46	0.2097
6.0–8.0	4.88	1.29	0.26	0.0694
8.0–10.0	−0.95	1.40	−0.05	0.0024

Slope is slope of the regression line. S.E. is standard error of the slope. C.C. is correlation coefficient. CD is coefficient of determination.
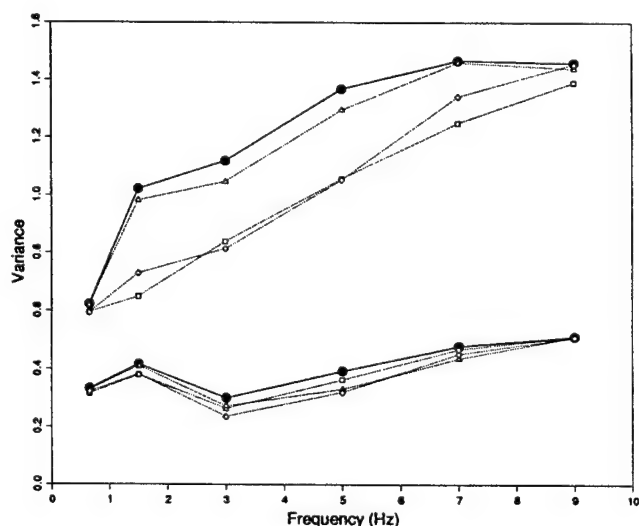
curve with a slope of 1 to the data set in each passband. These baseline shifts, generally being quite small, were then applied as station corrections in each passband for the combined data, and regressions were performed on distance, roughness, and distance × roughness.

For the station-corrected regressions, the reduced scatter causes the correlation coefficients with distance to increase by 0.04 to 0.1 in the passband from 1 to 6 Hz, with improved variance reductions of CD = 0.153 (1 to 2 Hz), 0.18 (2 to 4 Hz), and 0.10 (4 to 6 Hz). These results are summarized in Table 2. The correlations with roughness and variance

reductions for that variable were all within a few percent of the results for no station corrections. The correlations with distance × roughness increased by several percent in the 1- to 6-Hz band, and the maximum variance reduction (25%) was found for the 2- to 4-Hz data. The lack of effect on the roughness correlations and systematic improvement in the distance correlations raises the possibility that the station corrections may be biased by the nonuniform path coverage in the region (Fig. 1). Nonetheless, we are confident that the basic results of this article are not effects of station behavior.

Path Effects for P_n/L_g Phase Ratios

We made similar calculations for log P_n/L_g data. P_n is not a stable phase in this region, hence the variance of log P_n/L_g in all frequency bands (upper set of filled circles in Fig. 5) is much greater than for log P_g/L_g, by up to an order of magnitude. However, log P_n/L_g has stronger distance behavior than log P_g/L_g. Figure 6 shows the behavior of the 2- to 4-Hz passband. The correlation coefficient with distance (Fig. 6a; Table 3) is larger than for log P_g/L_g, and the slope is larger. The data at distances less than 400 km again display a slightly negative slope, consistent with the work of McCormack *et al.* (1995), but there is a significant increase at larger distances, again associated with abrupt increase near 500 km. The correlation with roughness is not very strong
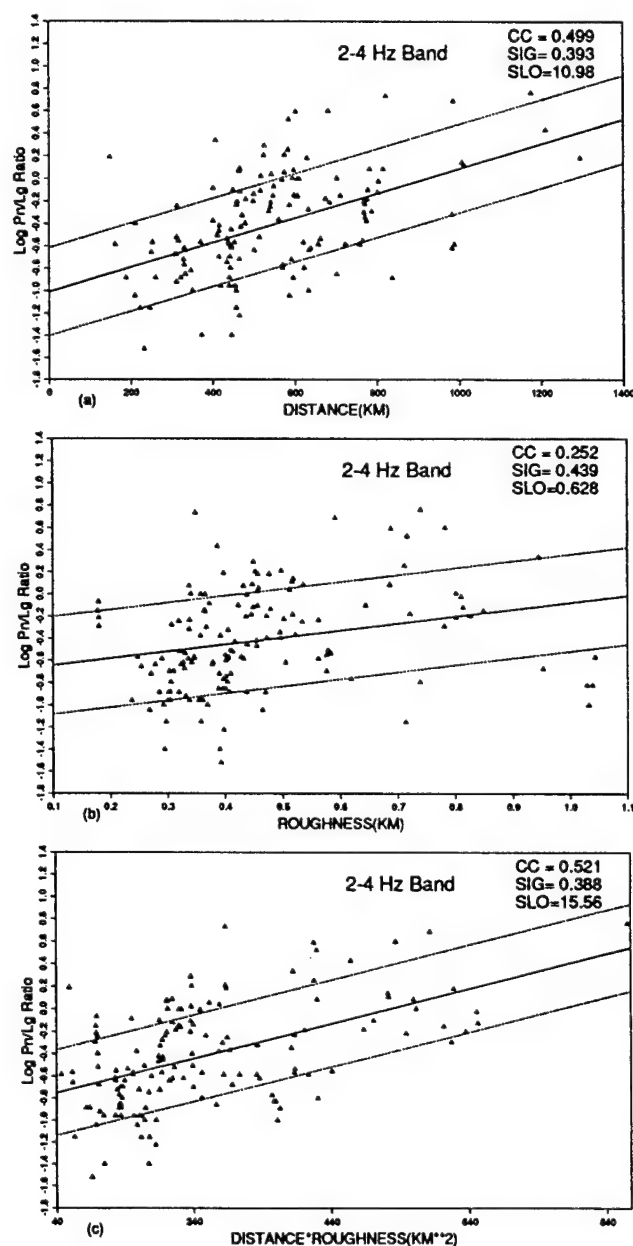

Figure 6. Log (P_n/L_g) as a function of (a) distance, (b) roughness, and (c) distance × roughness for Western U.S. data in the frequency band 2 to 4 Hz.

Table 3

(a) Regresion Results for P_n/L_g with Distance

Band (Hz)	Slope (× 10⁴)	S.E. (× 10⁴)	C.C.	CD
0.3–1.0	3.43	1.32	0.21	0.0442
1.0–2.0	12.68	1.38	0.60	0.3652
2.0–4.0	10.98	1.58	0.50	0.2495
4.0–6.0	11.65	1.78	0.48	0.2268
6.0–8.0	9.78	1.94	0.38	0.1481
8.0–10.0	5.48	2.05	0.22	0.0466

(b) Regression Results for P_n/L_g with Roughness

Band (Hz)	Slope	S.E.	C.C.	CD
0.3–1.0	0.123	0.153	0.07	0.0044
1.0–2.0	0.466	0.193	0.20	0.0384
2.0–4.0	0.628	0.199	0.25	0.0635
4.0–6.0	0.643	0.223	0.23	0.0538
6.0–8.0	0.200	0.238	0.07	0.0048
8.0–10.0	−0.336	0.237	−0.12	0.0136

(c) Regression Results for P_n/L_g with Roughness × Distance

Band (Hz)	Slope (× 10⁴)	S.E. (× 10⁴)	C.C.	CD
0.3–1.0	4.75	1.79	0.21	0.0458
1.0–2.0	15.26	1.99	0.54	0.2864
2.0–4.0	15.56	2.11	0.52	0.2713
4.0–6.0	15.93	2.41	0.48	0.2298
6.0–8.0	10.12	2.73	0.29	0.0858
8.0–10.0	2.01	2.85	0.06	0.0034

for log P_n/L_g (Fig. 6b). This makes sense in that P_n travels primarily below the crustal wave guide and is not influenced by the surface roughness as much as P_g. This also indicates that the roughness effect is not isolated to just the L_g phase. The product of distance and roughness gives a slightly stronger correlation than just using distance, but not at a significant level (Fig. 6c). The results for log P_n/L_g in various frequency bands are summarized in Figure 7 and Table 3. These patterns are similar to those for log P_g/L_g in Figure 3, except that the correlations with roughness are much lower. In this case, simple distance corrections are adequate and, in fact, necessary given the relatively strong trends.

Path Effects for Spectral Ratio Discriminants

While we might expect that crustal wave-guide roughness effects on individual phases should be similar to scattering attenuation, it might be possible to reduce the scatter on a path-by-path basis. This would be valuable for spectral ratio discriminants, which have been found to work quite well in tectonically active areas or for explosions in weak, porous material. Analysis of the P_g and L_g spectra is summarized in Figure 8, where strong distance dependence is found for the ratios (1 to 2 Hz)/(6 to 8 Hz), as previously observed (Taylor *et al.,* 1988). Note that the spectral ratios
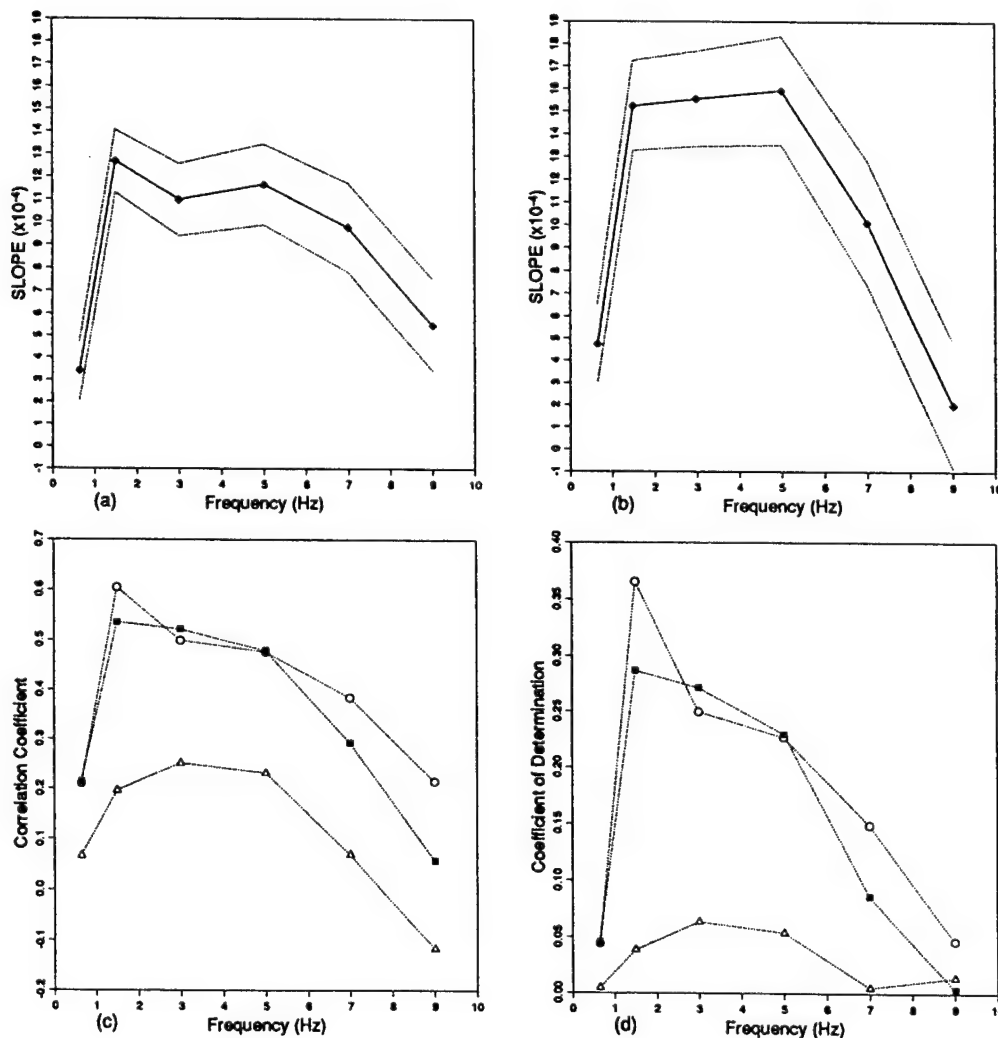

Figure 7.   Summary of the regression results of log (P_n/L_g) with distance, roughness, and distance $\times$ roughness. (a) Slopes of the regression lines of log (P_n/L_g) with distance in various frequency bands. The dashed lines indicate the standard error of each slope estimate. (b) Slopes of regressions on distance $\times$ roughness. The dashed lines indicate the standard error of each slope estimate. (c) The correlation coefficients of log (P_n/L_g) with distance (circles), roughness (triangles), and distance $\times$ roughness (squares). (d) The coefficients of determination of the regressions of log (P_n/L_g) with distance (circles), roughness (triangles), and distance $\times$ roughness (squares).
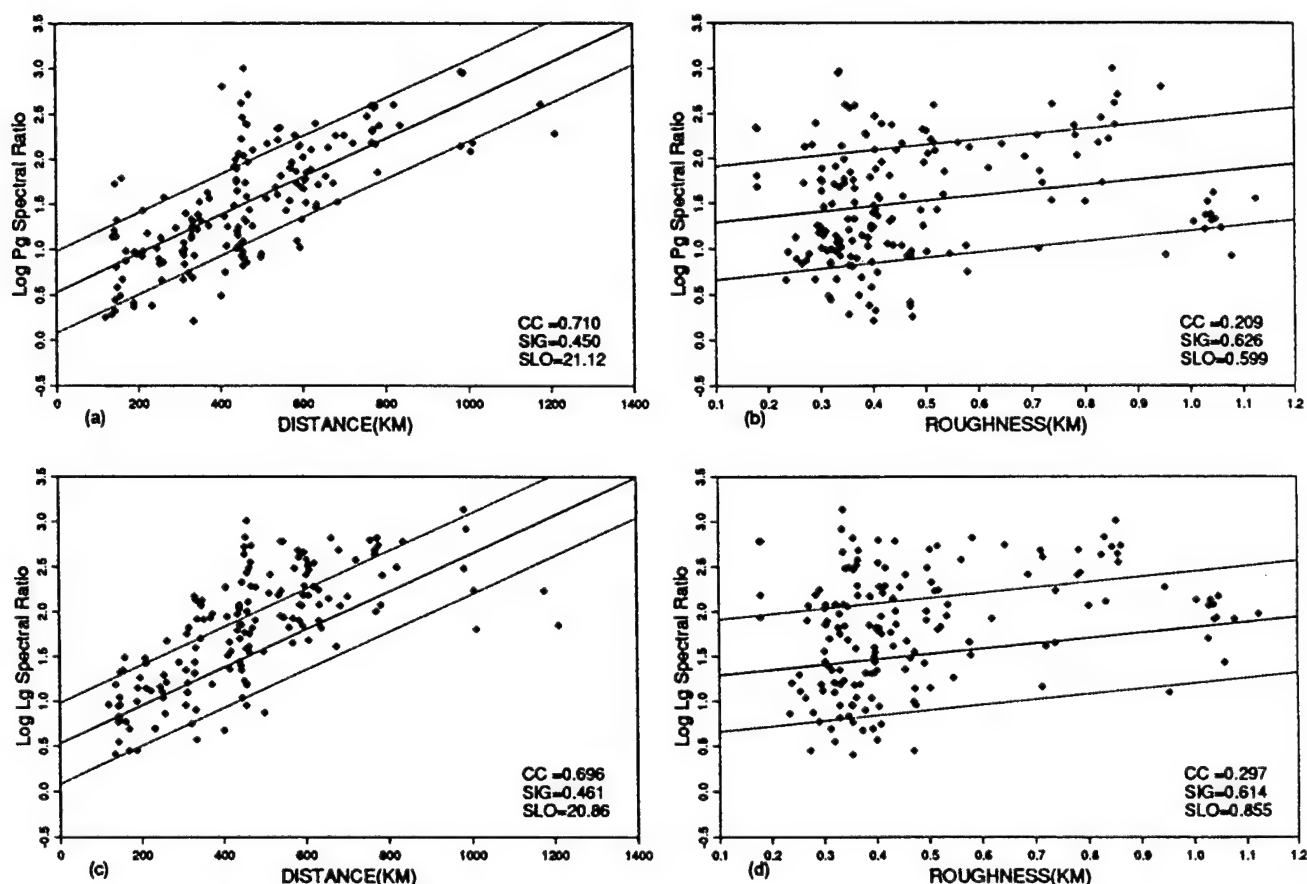
Figure 8. Spectral ratio (1 to 2)/(6 to 8) Hz for P_g (top) and L_g (bottom), versus distance (a) and (c) and topographic roughness (b) and (d).

show some abrupt structure near 500 km, with an increase in low-frequency energy for both P_g and L_g. The P_n data have very similar behavior to that in Figure 8. The correlations with surface roughness are relatively weak for all three phases, but some variance reduction could be achieved by making a correction. The results for P_g and L_g (Figs. 8b and 8d, respectively) have very large scatter, but clearly, some trend is present. Ratios for other frequency bands were considered, with generally similar patterns. Table 4 summarizes the variance reduction achieved for various path corrections for the spectral ratio discriminants.

Conclusions

Path effects on regional phases involve geometric spreading, attenuation, scattering, and blockage effects. Previously, we studied two types of path effects on P/L_g ratios: large-scale wave-guide structure and small-scale topographic roughness. Examples of the former are the necking of the crust and consequent thick sediment basins in the Barents and Kara Seas (Zhang and Lay, 1994b) and near the Caspian Sea and Arial Sea and their peripheral depressions (Zhang *et al.,* 1994). These structures cause L_g blockage or

Table 4
Low-Frequency/High-Frequency Discriminant Variance Reduction, CD

Corrected for	P_n	P_g	L_g
Roughness	0.0720	0.0437	0.0882
Distance	0.4608	0.5047	0.4846
Distance × roughness	0.3666	0.3939	0.4103

at least strong amplitude reductions and involve localized path effects. Our previous work on topographic roughness involved the Northern Eurasia region (Zhang and Lay, 1994a), where no L_g blockage is observed. In that case, the influence of surface roughness and statistics of other properties along the entire propagation paths become notable. In this study of regional phases in the Western United States, although the topographic roughness is even stronger than in the region studied by Zhang and Lay (1994a), there is no total blockage of L_g. We have again found that topographic roughness of the paths provides a readily quantifiable parameter that can reduce the variance in some regional discriminants. While the regional average behavior could be char-

acterized to allow discriminants in the Western United States to be transported to other regions (as in the work of Baumgardt and Der, 1994), the primary value of the present article is that the scatter within a given region can be reduced, presumably enhancing the performance of the discriminants.

The corrections based on distance and roughness dependence of the P_g/L_g ratio can reduce 22% of the data variance in the 2- to 4-Hz band (up to 25% for the station-corrected data). The P_n/L_g ratio does not have much correlation with surface roughness; however, the correction for distance alone (or distance $\times$ roughness; Figure 5) can reduce the variance by up to 36% for the 1- to 2-Hz band. Since these discriminants do not work very well on a regional basis in the Western United States due to large scatter in the data, these variance reductions are significant, particularly in the passband from 1 to 6 Hz, which tends to have more overlap in discriminant populations than at higher frequencies. The physical basis for why path corrections based on surface topography should work at all is not fully developed. Essentially, the topography may provide a surrogate for internal wave-guide structure that controls the partitioning of energy into different portions of the regional wave field (for example, scattering P_g into L_g). This may include the direct effect of surface scattering or effects of crustal thickness variations associated with isostatic compensation of the topography. Coupling of wave-guide attenuation structure and surface topography could also arise from tectonic processes. It does appear that some of the scatter for explosion observations is due to near-source effects such as depth and gas-filled porosity, so one should not expect path corrections to reduce all overlap in the discriminant populations.

We have considered only a very simple form of path property, and there is good reason to expect that other path characterizations such as sedimentary basin thickness, crustal thickness, or gradients in these parameters (e.g., Zhang et al., 1994; Baumgardt and Der, 1994) may provide comparable or additional variance reduction in the discriminants. However, surface topography is by far the highest resolution, most precise information that will ever be available for any given region, and thus it is very encouraging that reasonably strong variance reductions can be achieved in some cases using this simple characterization of the path. Simulation of the effect by numerical computations is underway and will be important if the empirical trends are to be placed on a sound physical basis, but additional research along this direction is worth pursuing.

Acknowledgments

References

Baumgardt, D. R. (1990). Investigation of teleseismic Lg blockage and scattering using regional arrays, Bull. Seism. Soc. Am. 80, 2261–2281.

Baumgardt, D. R. and Z. Der (1994). Investigation of the transportability of the P/S ratio discriminant to different tectonic regions, Scientific Report No. 1, PL-TR-94-2299. ENSCO, Inc., Springfield, Virginia.

Baumgardt, D. R. and G. B. Young (1990). Regional seismic waveform discriminants and case-based event identification using regional arrays, Bull. Seism. Soc. Am. 80, 1874–1892.

Bennett, T. J. and J. R. Murphy (1986). Analysis of seismic discrimination capabilities using regional data from western United States events, Bull. Seism. Soc. Am. 76, 1069–1086.

Bennett, T. J., A. K. Campanella, J. F. Scheimer, and J. R. Murphy (1992). Demonstration of regional discrimination of Eurasian seismic events using observations at Soviet IRIS and CDSN stations, Final Technical Report, PL-TR-92-2090, Maxwell Laboratories, Inc., S-Cubed Division, La Jolla, California.

Campillo, M., M. Bouchon, and B. Massinon (1984). Theoretical study of the excitation, spectral characteristics, and geometrical attenuation of regional seismic phases, Bull. Seism. Soc. Am. 74, 79–90.

Chun, K., G. F. West, R. J. Kokoski, and C. Samson (1987). A novel technique for measuring Lg attenuation: results from eastern Canada between 1 to 10 Hz, Bull. Seism. Soc. Am. 77, 398–419.

Fisk, M. D. (1994). Identification and event characterization—getting down to the outliers, in Proceedings of the ARPA CTBT Monitoring Technologies Conference, 26–29 September 1994, Carmel Highland Doubletree, San Diego, California.

Haskell, N. A. (1966). The leakage of continental crustal P waves, J. Geophys. Res. 71, 3955–3967.

Kennett, B. L. N. (1993). The distance dependence of regional phase discriminants, Bull. Seism. Soc. Am. 83, 1155–1166.

Lynnes, C. and R. Baumstark (1991). Phase and spectral discrimination in North America, Final Technical Report, PL-TR-91-2212(II). Teledyne Geotech, Alexandria, Virginia.

Mayeda, K. and W. R. Walter (1995). Source parameters of western U.S. earthquakes: moment, energy, stress drop and source spectra from regional coda envelopes, J. Geophys. Res., submitted.

McCormack, D. A., K. F. Priestley, and H. J. Patton (1995). Distance effects on regional discriminants along a seismic profile in northwest Nevada; NPE and nuclear results, Bull. Seism. Soc. Am., submitted.

Murphy, J. R. and T. J. Bennett (1982). A discrimination analysis of short-period regional seismic data recorded at Tonto Forest Observatory, Bull. Seism. Soc. Am. 72, 1351–1366.

Pomeroy, P., W. Best, and T. McEvilly (1982). Test ban treaty verification with regional data—a review, Bull. Seism. Soc. Am. 72, S89–S129.

Sereno, T. J. (1991). Simulation of the detection and location capability of regional seismic networks in the Soviet Union, Final Report, SAIC-91/1061, San Diego, California.

Taylor, S. R. and M. D. Denny (1991). An analysis of spectral differences between Nevada Test Site and Shagan River nuclear explosions, J. Geophys. Res. 96, 6237–6245.

Taylor, S. R., N. W. Sherman, and M. D. Denny (1988). Spectral discrimination between NTS explosions and western United States earthquakes at regional distances, Bull. Seism. Soc. Am. 78, 1563–1579.

Taylor, S. R., M. D. Denny, E. S. Vergino, and R. E. Glaser (1989). Regional discrimination between NTS explosions and western U.S. earthquakes, Bull. Seism. Soc. Am. 9, 1142–1176.

Walter, W. R., K. M. Mayeda, and H. J. Patton (1995). Phase and spectral ratio discrimination between NTS earthquakes and explosions. Part 1: Empirical observations, Lawrence Livermore Natl. Lab. Rep., UCRL-JC-118551.

Wessel, P. and W. H. F. Smith (1991). Free software helps map and display data, EOS 72, 441, 445–446.

Zhang, T.-R. and T. Lay (1994a). Analysis of short-period regional phase path effects associated with topography in Eurasia, Bull. Seism. Soc. Am. 84, 119–132.

Zhang, T.-R. and T. Lay (1994b). Effects of crustal structure under the Barents and Kara seas on short-period regional wave propagation for Novaya Zemlya explosions: empirical relations, *Bull. Seism. Soc. Am.* **84,** 1132–1147.

Zhang, T.-R., S. Y. Schwartz, and T. Lay (1994). Multivariate analysis of waveguide effects on short-period regional wave propagation in Eurasia and its application in seismic discrimination, *J. Geophys. Res.* **99,** 21929–21945.

Zhang, T.-R. and T. Lay (1995). Why the Lg phase does not traverse oceanic crust, *Bull. Seism. Soc. Am.* **85,** 1665–1678.

Institute of Tectonics and W. M. Keck
Seismological Laboratory
University of California, Santa Cruz
Santa Cruz, California 95064
  (T.-R.Z., T.L., S.S.)

Earth Sciences Division
Lawrence Livermore National Laboratory
Livermore, California 94550
  (W.R.W.)

Seismic Wave-Field Observations at a Dense, Small-Aperture Array Located on a Landslide in the Santa Cruz Mountains, California

by Zhengyu Xu, Susan Y. Schwartz, and Thorne Lay

Abstract   A rectangular (4 by 5) array of short-period three-component seismometers with 15-m spacing was deployed to record several U.S. Geological Survey calibration explosions detonated around the Santa Cruz Mountains. The array was located at a site where an earlier station had recorded frequency-dependent polarized site resonances for aftershocks of the 1989 Loma Prieta earthquake. The site is on a hillside believed to be a landslide structure, with the near surface consisting of poorly sorted sediments and weathered rocks with dipping subsurface layers. The primary objective was to explore the site effects in this complex three-dimensional soft-rock environment, characteristic of much of the Loma Prieta source region. The direct P waves from four nearby (15 to 20 km) explosions at easterly azimuths from the array show counterclockwise arrival azimuth anomalies of 30° to 50°. These deflections are attributed to the presence of more than one dipping velocity contrast beneath the array, with dips of from 10° to 50° and dip directions generally toward the south. One such boundary may correspond to the landslide slip surface, and the presence of dipping velocity contrasts underlying the site is probably responsible for some of the observed directional site resonance. A slowness vector analysis demonstrates that arrivals early in the P coda have similar azimuthal anomalies, while later scattered arrivals come from many azimuths. Particle motions indicate that the more coherent arrivals in the coda are comprised of scattered P waves and Rayleigh waves, probably associated with scattering from the rough topography in the region. The coda displays greater spatial coherency along the hill strike than down the slope, consistent with a wedge-shaped landslide. The overall wave-field spatial coherence, $CCC(f, \Delta x)$, decreases with increasing frequency, f, and spatial offset, Δx, and on average can be well represented by $CCC(f, \Delta x) = e^{-cf\Delta x}$, with $c = 0.6 \text{ km}^{-1} \text{ Hz}^{-1}$ for the vertical P wave in the first 1-sec window. This behavior is comparable to that found for previously studied hard-rock locations.

Introduction

High-frequency seismic wave propagation in the crust tends to be very complicated, and it is useful to analyze recordings from dense, small-aperture seismic arrays (station spacing from tens to hundreds of meters) to quantify the source and propagation effects that are relevant to earthquake engineering (e.g., Menke *et al.,* 1990; Vernon *et al.,* 1991; Frankel *et al.,* 1991; Hartzell *et al.,* 1994; Mori *et al.,* 1994). Array recordings allow the deterministic features of the short-period wave field to be characterized, including the slowness vector and polarization of discrete plane-wave phases that sweep across the array (e.g., Dainty and Toksöz, 1990; Gupta *et al.,* 1990; Bannister *et al.,* 1990; Wagner and Owens, 1993). Localized scattering effects within the array must be treated differently than remote scattering effects, but the scatterers can still be analyzed deterministically (e.g., Hedlin *et al.,* 1991). Identification of the coherent arrivals

can constrain the large-scale structures and scattering heterogeneities in the crust between the source and the receivers and in the vicinity of the array. Seismic wave coda generally becomes progressively more complex with time, with many interfering arrivals scattered from different directions. Even for small-aperture arrays, there is a transition to an incoherent wave field in which individual arrivals cannot be reliably tracked across the array because of interference from multiple arrivals. Statistical measures of the wave field such as spatial coherence are then used to characterize the overall signal complexity and associated scattering properties of the medium, recognizing that the deterministic substructure of the coda is simply not fully resolvable.

The transition from deterministic to incoherent wave field is a fuzzy one, influenced by the signal frequency content, the limitations of the array response, and the local scat-

tering properties in the crust. For isolated three-component stations, little can be done other than to monitor the signal polarization as a function of time using the event backazimuth as a reference frame. When an array is located in a homogeneous hard-rock region, the short-period ($T < 1$ sec) signal coherence drops off significantly over station spacing of just tens of meters (e.g., Menke *et al.,* 1990; Vernon *et al.,* 1991), presumably due to intense scattering from shallow heterogeneity. Even more complex behavior is expected in heterogeneous soft-rock environments. For example, sediment-filled valleys cause frequency-dependent amplifications relative to hard-rock sites (e.g., King and Tucker, 1984; Tucker and King, 1984; Tucker *et al.,* 1984), while rough-surface topography causes short-period signal amplifications (e.g., Geli *et al.,* 1988; Hartzell *et al.,* 1994; Pederson *et al.,* 1994). Many earthquake engineering issues are associated with complex soft-rock sites in tectonically active regions.

This article considers three-component recordings of four shallow explosions from a dense, small-aperture array located in the Santa Cruz Mountains above the 1989 Loma Prieta earthquake rupture zone. The objective is to study the short-period wave field in a geologically complex region with rough-surface topography and dipping geological structures. This contrasts with earlier deployments of dense small-aperture arrays in geologically simple environments and provides insight into the possible site effects for isolated sensors deployed for aftershock recordings or earthquake engineering purposes.

We initially analyze the deterministic features of the explosion recordings, emphasizing the first arrivals. Many studies of direct *P*-wave backazimuths have revealed biases of up to tens of degrees (e.g., Niazi, 1966; Buchbinder, 1987, 1990; Magotra *et al.,* 1987; Menke *et al.,* 1990; Suteau-Henson, 1990, 1991; Zhang and Langston, 1992). These deflections are commonly attributed to lateral velocity gradients (e.g., Buchbinder, 1987), dipping surface geometry (e.g., Buchbinder and Haddon, 1990), or dipping velocity contrasts beneath the receiver (Niazi, 1966; Cassidy, 1992; Langston, 1977, 1979; Zhang and Langston, 1992). Unusually large backazimuth anomalies are found in our case, which we attribute to dipping subsurface boundaries. We extend the analysis of arrival direction to the *P* coda using a plane-wave slowness vector procedure (analogous to frequency-wavenumber analysis), along with consideration of the polarization. The local crustal heterogeneity appears to cause significant scattering; longitudinally polarized arrivals impinge on the array from many azimuths.

Statistical characteristics of the coda are also considered for comparison with previous work using similar instrumentation and station spacing on hard-rock sites (Menke *et al.,* 1990; Vernon *et al.,* 1991). The influence of the deterministically constrained larger-scale structure on the incoherent signal is examined, along with a consideration of the likely causes of the preferred *S*-wave polarizations observed in the region. The latter issue will be discussed at greater length in another study (Bonamassa and Vidale, in preparation). The

general conclusion is that shallow structure beneath the site exerts a profound affect on the short-period wave field that would be almost unrecognizable without the advantage of a dense array. This suggests caution in the analysis of isolated station signals for aftershock studies and earthquake engineering applications.

The Zayante Dense Array

The Santa Cruz Mountains are a tectonically active, geologically complex region with rough-surface topography, contorted sedimentary structures, and relatively low-velocity near-surface rock types. This environment offers many earthquake engineering challenges, including the variability of ground-motion amplification observed for hilltops (Geli *et al.,* 1988; Hartzell *et al.,* 1994) and in sediment-filled valleys (King and Tucker, 1984; Tucker and King, 1984; Tucker *et al.,* 1984). Among the many interesting site-response characteristics observed in recordings of aftershocks of the 1989 Loma Prieta earthquake, frequency-dependent preferred resonance directions, independent of earthquake location and focal mechanism, were observed in ground shaking at several locations (Bonamassa and Vidale, 1991; Bonamassa *et al.,* 1991). These resonances tend to be spatially highly variable, based on observations from nested tripartite mini-arrays with station spacing of 25 and 300 m.

One of the sites that displayed strong frequency-dependent preferred *S*-wave polarizations was selected as a study area (Fig. 1). The earlier ZAYA mini-array deployed in this region (Bonamassa and Vidale, 1991) exhibited directional resonances at four of six stations, with general consistency in frequency-dependent behavior (Fig. 1c), but the other two nearby stations showed no resonances, suggesting very shallow control on the ground motions. To improve our understanding of such site effects, we deployed a small-aperture array, which we call the Zayante array, near the location of the Z5 element of the ZAYA array. The Z5 recordings displayed westerly to northwesterly directions of preferred *S*-wave vibration, loosely paralleling the trend of a nearby ridge.

The Zayante array consisted of a 4 by 5 grid of short-period Mark Products L-22 three-component geophones with a grid spacing of 15 m (Fig. 1d). The signals from the 2-Hz seismometers were sampled at 200 samples per second. The performance of these seismometers is quite good in the 2- to 15-Hz range but deteriorates above this (Menke *et al.,* 1991). The signal-to-noise ratio in our data is highest below 15 Hz, but we do consider the higher-frequency information recognizing that it may have some contamination from instrument nonlinearity. The array was situated on a landslide surface (Gerry Weber, personal comm., 1992) with the hillside dipping about 10° toward the south-southwest. The surrounding structure is the San Lorenzo syncline, a Tertiary structure, with the Lambert shale (Brabb and Dibblee, 1979) underlying the soil in the immediate vicinity of the array. The geometry and depth of the landslide slip surface are not
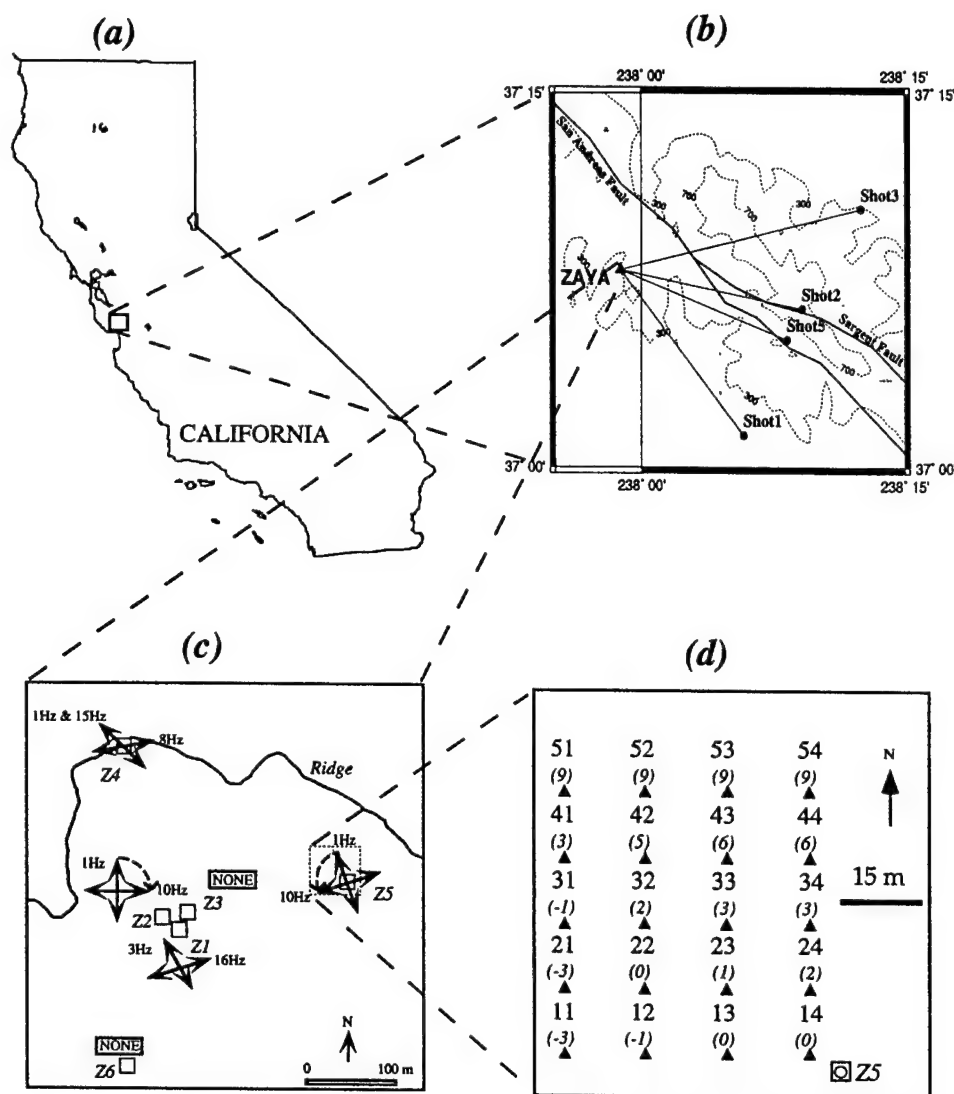
Figure 1. Maps of the ZAYA and Zayante arrays. (a) Base map indicating the location of the study area in the Santa Cruz Mountains of California. (b) Local topography near the San Andreas fault and locations of the ZAYA array and four explosion shotpoints for the U.S. Geological Survey calibration shots. (c) Locations of the six elements of the ZAYA array along with frequency-dependent directions of preferred S-wave ground shaking (if any) indicated by the arrows (Bonamassa and Vidale, 1991). The small Zayante array was deployed near element Z5 of the ZAYA array. A nearby ridgetop is indicated. (d) Geometry of the Zayante array, with stations names given by row/column numbering with rows trending east–west and columns, north–south. The 20-element array has 15-m sensor spacing. The numbers in parentheses are the relative elevations of the array elements in meters.

known, but presumably, there is a southerly dip. A shallow refraction survey was subsequently conducted in the array vicinity (Bonamassa *et al.,* 1993), finding that the near-surface layer varies in thickness from 1 to 20 m with a *P* velocity of about 550 m/sec, while the velocity below this layer is about 1250 m/sec. The quasi-planar velocity discontinuity dips about 20° toward the southwest.

The Zayante array was deployed to record several explosions detonated by the U.S. Geological Survey as part of an effort to calibrate shallow velocity structure in the Santa

Cruz Mountains (Eberhart-Phillips and Michael, 1991). Four of the explosions (Table 1; Fig. 1b) were recorded with good signal-to-noise ratio. These events are at distances of 15 to 20 km from the array and have easterly backazimuths varying by about 63°. While some ambient noise time intervals were also recorded, no events at other azimuths were detected during the short deployment of the array. The array was primarily intended to explore variability of local ground motions in the vicinity of the site with polarized resonances and was not designed to include outlying elements that

Table 1
Explosion Source Information

| Shot ID	Lat (°N)	Lon (°W)	Distance (km)	Backazimuth	Elevation (m)
1	37.02	121.90	16.14	139.76°	79
2	37.11	121.85	15.55	100.80°	1034
3	37.17	121.79	20.64	77.29°	175
5	37.09	121.86	15.08	110.32°	530

Figure 2. Vertical-component seismograms from 12 stations in the Zayante array for event 2. The signals are shown with true relative amplitudes, and the station names follow the labeling in Figure 1.

would have enhanced the resolution of plane waves traversing the array, but the high sample rate and good signal-to-noise quality of the recordings still allow a limited use of the recordings as a dense small-aperture array.

Analysis of Direct-Arrival Backazimuth Anomalies

The signals recorded at the Zayante array provide a high-quality data set for four nearby explosions of precisely known location. Some of the waveforms for one of the explosions (event 2) are shown in Figure 2, with the station labeling defined in Figure 1d. Only minor instrument amplification variability is expected among the sensors, but the emplacement sites were all in pits in the sediments no deeper than 1 m, so ground coupling variability is definitely possible. Our analysis uses normalized amplitudes at each sensor, and we focus on relative waveform characteristics rather than absolute amplitudes.

As is the case for all four explosions, the seismograms for event 2 (Fig. 2) have good signal-to-noise ratios, especially on the vertical components, and the first P arrival on each trace is readily identifiable, allowing it to serve as a reference phase. The horizontal components tend to exhibit more waveform variability, but even the vertical components show some waveform changes over 15-m separations (compare traces 21 and 22). The early portion of the waveforms is enriched in higher frequencies. For this event, there is significant signal amplitude for about 9 sec after the P arrival, with longer-period energy arriving about 5 sec after P. It is worth noting that there is slightly greater visual coherence among the arrivals on a given row of the array than between rows, suggesting that local structure under the array varies down the hillside. We will quantify this tendency later.

The bandwidth of the signals is indicated by Figure 3, which shows the average spectra from all vertical-component stations using 9-sec windows for two separate shots, along with the average spectra from an eventless interval of microtremor. The explosion recordings have reasonable signal-to-noise ratios from 3 to 22 Hz, with little signal above 22 Hz, especially later in the recording. The stronger explosions, such as event 2, have good signal-to-noise ratios at frequencies as low as 1 Hz. The array-averaged microtremor spectra are fairly smooth, but individual spectra vary substantially.
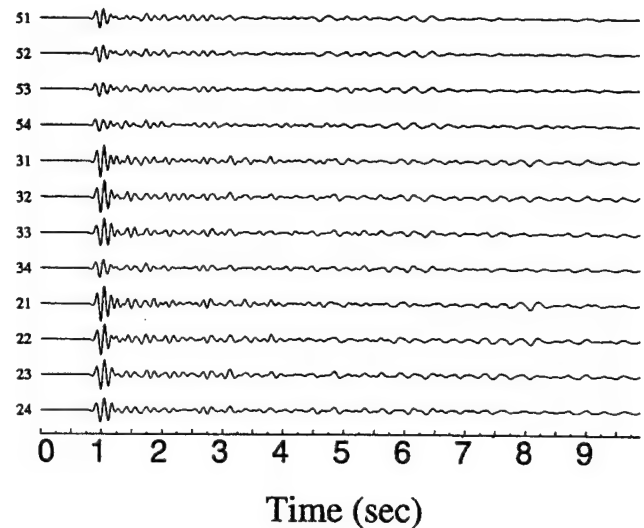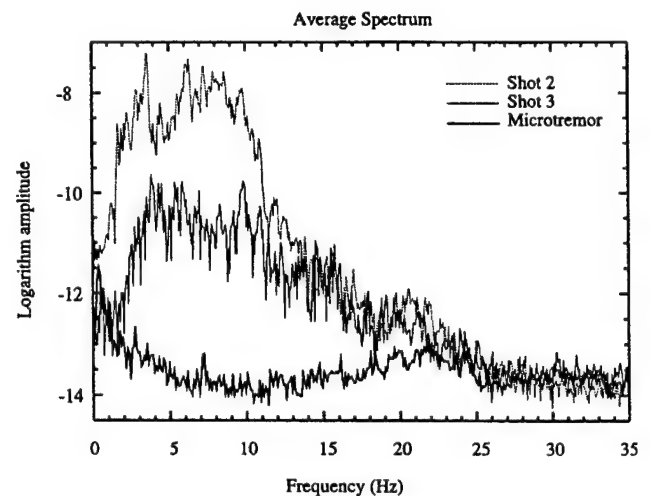

Figure 3. Amplitude spectra of 9-sec windows of vertical-component seismograms (approximately proportional to ground velocity) averaged across the Zayante array for two explosions and an event-free interval of microseismic noise.

We analyze two attributes of the direct P arrivals from each explosion to characterize any backazimuth anomaly. The particle motions of the horizontal components are used to estimate the backazimuth (Fig. 4b). The P-wave polarity measurement is made at each station using the unfiltered recordings, with the backazimuth estimates being averaged across the array for each event. An independent estimate of the backazimuth is provided by the relative arrival times of the P signals. Cross-correlation of a short time window (Fig. 4a) spanning the direct arrival is used to measure the tiny travel-time differences across the array, with the vertical
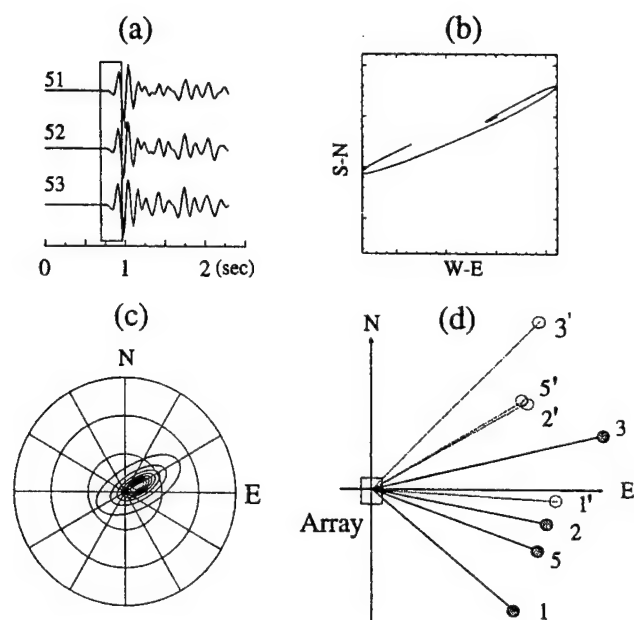
Figure 4. Procedures used to estimate the propagation direction of the initial *P* wave. (a) Vertical-component seismograms for shot 2, illustrating the time window used for frequency-wavenumber (*f-k*) analysis. A very short, highly coherent interval is used. (b) Horizontal particle motion for station 11 for shot 2. The nearly linear motion in the first cycle of the *P* arrival is used to estimate the apparent backazimuth. (c) Broadband *f-k* analysis of the direct *P*-wave power spectrum for shot 2 in the window shown in (a). A maximum likelihood method is used, with the spectrum contoured in the wavenumber domain. The peak contour indicates the northeasterly backazimuth. (d) Summary of estimated (open circles) and actual (filled circles) backazimuths for the four shots. The average estimates from the particle motion and *f-k* methods are shown. Biases of 30° to 50° are found for all four events, with systematic counterclockwise rotations.

components providing the more stable differential times due to their waveform coherence. These differential times are fit with a plane wave to estimate the backazimuth, but the angle of incidence of the wavefront cannot be separately resolved due to the planar array geometry. The relative timing also controls the backazimuths inferred from frequency-wavenumber analysis. Results of this analysis (Fig. 4c) confirm the values of backazimuth obtained from fitting a plane wave to the relative arrival times. In each case, the direction that is obtained is an "apparent" backazimuth, uncorrected for dip of the surface under the array.

The apparent backazimuths estimated by the particle motion and relative arrival time methods differ by no more than 7° for the four sources. For each event, large counterclockwise biases of the apparent backazimuths are observed, as illustrated in Figure 4d. Several factors may contribute to these biases, and we consider simple models to explain the systematic 30° to 50° backazimuth anomalies.

Effects of the Dipping Surface on Apparent Backazimuth Estimates

The surface topography at the Zayante array is approximately planar with a 10° dip and a dip direction of S14°W. This dip causes arrival-time variations that bias the backazimuth estimated by *f-k* or wave-front fitting procedures. By transforming the ray projections from the dipping plane to a horizontal plane, we can correct for the effects of the surface dip, without needing to know the shallow velocity structure. The geometry is such that the predicted bias in backazimuth is clockwise by about 20° to 30° for all four shots. This is opposite to the bias in the observations, indicating that structure beneath the array is responsible for the backazimuth deviations. Before we can determine subsurface structure consistent with our backazimuth observations, the large effects of the free surface must be corrected for.

A dipping surface also affects polarization estimates of backazimuth when the wave front sweeps obliquely across the surface, because the dipping surface defines the boundary controlling the receiver function that partitions amplitude onto the locally defined (i.e., relative to the dipping surface) vertical and horizontal components (Buchbinder and Haddon, 1990). The extent of backazimuth bias varies with the angle of incidence, dip of the surface, and ratio of *S* velocity to *P* velocity. We can estimate the angle of incidence from the particle motions, but this is also an apparent angle, influenced by the free-surface interaction. For a horizontal free surface, the relationship of the true incidence angle (relative to the vertical), i_p', to the measured incidence angle, i_p' ($i_p' = \tan^{-1} P_h/P_v$; where P_h is the horizontal-component amplitude of the *P* wave and P_v is the vertical-component amplitude), is given by

$$\cos i_p' = 1 - 2V_s^2/V_p^2 \sin^2 i_p, \qquad (1)$$

where V_s and V_p are the *S*-wave and *P*-wave velocities near the surface, respectively (Bullen, 1963). The velocity terms enter into the calculation through the receiver function. Using (1), it is possible to infer the true incidence angle based on the surface motions. An additional correction is needed to account for the coordinate rotation when the surface dips. For the two cleanest events, the measured values of i_p' are 11° to 19°. For a Poisson ratio of 0.25 ($V_p = 1.732 V_s$), this indicates true subsurface incidence angles that are a few degrees smaller. One can compute the effects of the dipping surface on polarization azimuths for a given incidence angle of the *P*-wave vector by rotating to the coordinate system orthogonal to the dipping surface, calculating the *P*-wave motions in that coordinate system, and then projecting the motions to the geographic coordinate system. Unlike the large arrival-time backazimuth bias of 20° to 30° caused by surface topography, the 10° dip of the Zayante array predicts a very small polarization backazimuth bias. For a typical soft-rock ratio of $V_p/V_s = 2.0$, we find that the surface effect on polarization azimuths actually goes to zero. Uncertainty

in the precise near-surface V_p/V_s ratio will always make it difficult to reliably correct polarizations for surface dip.

Effects of Dipping Interfaces beneath the Array

A likely cause of large backazimuth anomalies is the presence of a dipping interface with a strong velocity contrast below the array. Niazi (1966) considered the effects of a dipping Moho on array measurements at the surface and provided expressions for calculating the bias in backazimuth as a function of velocity contrast and dip of the interface. We use his results with minor corrections for inconsistencies in sign convention. Aside from plausibility, there are two lines of evidence to suggest that dipping interfaces below the array are present. The first is the geological structure, with the array lying on a southwestward dipping landslide deposit located in the southwestward dipping flank of a synclinal structure. The second is more direct, with the shallow reflection/refraction survey in the area, indicating that there is an interface separating layers with P velocities of 550 m/sec and 1250 m/sec with a dip angle of 20° and a dip direction of S29°W (Bonamassa *et al.,* 1993). A schematic of the shallow structure under the Zayante array is indicated in Figure 5. For specified true backazimuths and incidence angles, the biasing effect of the shallow dipping interface was cal-
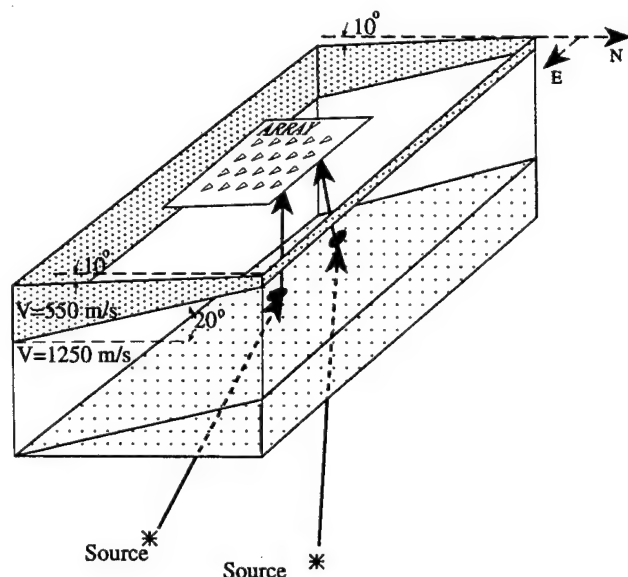
culated and found to cause an azimuthally varying counterclockwise bias for sources that lie eastward from the array. This is illustrated in Figure 6 for a generic dipping discontinuity. The near-surface dipping interface produces counterclockwise backazimuth biases on the order of 10° for the travel-time method. This has the correct sign but is much smaller than the observed biases and, at most, compensates the opposing bias induced by the surface dip. It appears that at least one more dipping interface, probably with a larger velocity contrast, exists below the array, as indicated in Figure 5. We seek simple models with an additional deeper interface that yields backazimuth biases for both travel-time and polarization methods consistent with the observed biases.

Modeling Results

Any modeling effort is complicated by our ignorance of the ray-path effects between the sources and receivers, with the ray paths not penetrating very deeply into the heterogeneous crust. We therefore calculated apparent backazimuths using arrival-time and polarity methods for a wide range of incident ray parameters below the modeled structure, assuming all the bias is due to local structure under the array. The limited class of models considered includes the known surface geometry; the geometry and velocities of the shallowest low-velocity layer; and one additional dipping interface below the array, separating material with a P velocity of 1250 m/sec from deeper structure with P velocity varying up to

Figure 5.   Block diagram of the shallow structure under the Zayante array as viewed from the northeast. The array is located on a 10° dipping surface plunging S14°W and overlies a 20° dipping plane (S29°W) with a P velocity increase from 550 to 1250 m/sec. This interface is from 3 to 10 m below the surface and is constrained by shallow refraction surveying. The deeper structure inferred to cause the array backazimuth bias is a southward-dipping plane with a stronger velocity contrast. The deflection of ray paths from sources east of the array are schematically indicated to suggest the counterclockwise sense of the bias in backazimuth.
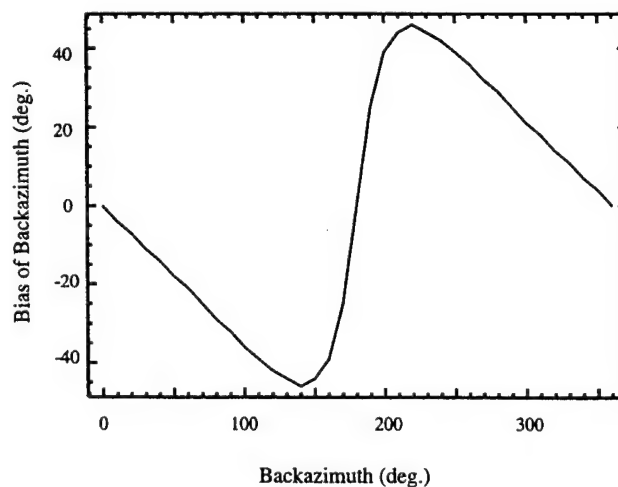

Figure 6.   The azimuthally varying pattern of bias in backazimuth resulting from a dipping velocity contrast beneath an array where the shallow layer is lower velocity. The up-dip direction is assigned a reference backazimuth of 0°, and there is no bias. Arrivals from azimuths of 0° to 180° will have negative (counterclockwise) backazimuth biases, while those from 180° to 360° will have positive biases. The pattern of backazimuth perturbation can constrain the dip if the velocity contrast is known, or vice versa. The pattern is not unique when both dip and velocity contrast are varied.

around 4300 m/sec. We include corrections for the surface dip and the shallow-dipping interface.

We have nine reliable observations of angles: four apparent backazimuths from the arrival time method, two apparent incidence angles, and three apparent backazimuths from the polarity method. In order to stabilize the modeling, we impose two constraints. First, differences between predicted and observed incidence angles and backazimuths are not allowed to exceed the estimated measurement uncertainties of 3° and 7°, respectively. The second constraint is on the minimum velocity at the turning point of the ray path. This velocity must exceed the average velocity from source to receiver. The average velocity is close to 4 km/sec for shots 1, 2, and 5 (all with epicentral distances near 15 km) and close to 5.7 km/sec for shot 3 at a distance of 21 km. We make a first-order approximation that the turning point velocity, V_t, is directly proportional to the average velocity, V_a. The higher the turning point velocity, the smaller the ray parameter and the steeper the incidence angle. Variations in V_a between events are used to scale differences in their incidence angles proportionally.

We perform a grid search on four parameters: wave incidence angles just below the deep interface for the four shots, velocity contrast across the deep interface, dip angle, and dip direction of the deep interface. For the polarization measurements, we must also consider the near-surface V_p/V_s ratio to correct for the effects of the dipping surface. We calculate the turning-point velocity and the contributions to each measurement from the deep discontinuity, the shallow discontinuity, and the dipping surface. The subsurface discontinuities contribute identically to the travel-time and polarization measurements in that they simply cause refraction of the ray paths. Thus, the key to finding a consistent model for the overall data set is the behavior of the surface contributions. But here we run into a problem; while our observations of backazimuth for the two methods agree, the dipping surface causes a large clockwise azimuth bias for the travel-time method, while it predicts either a counterclockwise or at most a small clockwise bias for the polarization method, depending on the V_p/V_s ratio. For hard-rock ratios such as $V_p/V_s = 1.732$, we obtain the maximum clockwise-valued bias, but it is only about 3° (compared to 20° to 30° for arrival times), thus a unique model compatible with all of the observations is not possible.

We found combinations of model parameters that satisfy the arrival-time backazimuths and incidence angles within their measurement bounds (Table 2), models that satisfy the polarization backazimuths and incidence angles (Table 3), but no models fitting the complete set of observations within their measurement bounds. Both data sets indicate that a deeper interface dips toward the S or SSE with poorly resolved dip ranging from 7° to 51°. A strong velocity contrast across a shallow-dipping (7° to 20°) deeper interface is preferred, as this makes the most sense geologically. The sets of models fitting each data set do not overlap, which may reflect our underestimation of the measurement uncer-

tainty or possibly an intrinsic failure of the ray method to account for finite-frequency effects. The fact that the raw backazimuth measurements from polarizations and arrival times are similar is fortuitous, as they actually are expected to differ due to the geometry of the problem. One possible factor is that the free-surface interaction controlling the polarizations involves finite-frequency arrivals that may effectively sense average near-surface properties rather than the very shallowest structure. We have higher confidence in the results based on relative arrival times, as these are insensitive

Table 2
Models Based on Relative Arrival Times (all models satisfying measurement bounds on each datum).

Deep Interface Geometry		Velocity Contrast	Incidence Angle	Error*
Dip Angle	Dip Azimuth			
15°	140°	0.29	65°	0.63
15°	140°	0.29	70°	0.62
15°	150°	0.29	70°	0.59
15°	140°	0.29	75°	0.59
15°	150°	0.29	75°	0.57
15°	140°	0.29	80°	0.56
15°	150°	0.29	80°	0.54
15°	140°	0.29	85°	0.56
19°	140°	0.39	45°	0.67
19°	140°	0.39	50°	0.70
19°	150°	0.39	50°	0.55
19°	150°	0.44	35°	0.62
23°	140°	0.49	35°	0.67
27°	150°	0.59	30°	0.54
31°	140°	0.64	25°	0.68
35°	140°	0.69	25°	0.65
39°	140°	0.74	20°	0.76
43°	140°	0.79	20°	0.65
43°	150°	0.79	20°	0.66
51°	140°	0.84	20°	0.60

*Error is an uncertainty weighted variance of the misfit to the relative arrival time backazimuths and angle of incidence measurements.

Table 3
Models Based on *P*-Wave Polarizations (all models satisfying measurement bounds on each datum). The V_p/V_s is 2.1.

Deep Interface Geometry		Velocity Contrast	Incidence Angle	Error*
Dip Angle	Dip Azimuth			
7°	180°	0.69	25°	0.73
7°	190°	0.69	25°	0.70
7°	150°	0.84	20°	0.75
7°	160°	0.84	20°	0.73
7°	170°	0.84	20°	0.69
7°	180°	0.84	20°	0.66
7°	190°	0.84	20°	0.65
11°	170°	0.84	20°	0.75
11°	180°	0.84	20°	0.72
11°	190°	0.84	20°	0.70
15°	190°	0.84	20°	0.72

*Error measure is an uncertainty weighted variance of the misfit to the polarization backazimuths and angle of incidence measurements.

to the precise near-surface Poisson ratio. For V_p/V_s ratios greater than 2.1, no model could be reconciled with the polarization-based observations, because the azimuthal pattern of backazimuth biases could not be matched. Results of the refraction experiment (Bonamassa *et al.*, 1993) indicate V_p/V_s ratios of up to 2.1, and we conclude that the polarization observations may have been contaminated in some manner. The models fitting the arrival-time data attribute large backazimuth anomalies on the order of 50° to 60° to a deeper interface, which may correspond to the slip surface of the landslide that underlies the Zayante array. Of course, several interfaces could actually be involved. While some ambiguity remains, and only simple models have been considered, the robust aspect of the analysis is that the very shallow subsurface effects produce large backazimuth biases that are difficult to predict *a priori*.

Array Analysis of *P* Coda

Analysis of secondary arrivals in the seismograms can further reveal the very near receiver effects of the site. First, we attempt to identify coherent secondary arrivals and their trajectories across the array. We do this using a slowness vector analysis (Xie and Lay, 1994) that is basically similar to *f-k* analysis. The procedure calculates the signal power distribution in the horizontal slowness plane in discrete time intervals. Figure 7 shows the summed power distributions for all three components of motion for shot 2, in 1-sec time windows (see Fig. 2 for time scale). The first window contains the onset of the *P* arrival, and the peak energy has a slowness vector pointing at an azimuth of 240° (i.e., incident at an azimuth of 60°, which is 40° counterclockwise of the true backazimuth of 100°), which is consistent with the corresponding *f-k* analysis shown in Figure 4c. The strongest coherent plane-wave energy is in the window from 1 to 2 sec (Fig. 7a) with a northeasterly arrival azimuth; this is the main *P*-wave motion. For later windows, the peak energy has highly variable propagation directions, although there is some tendency for energy to arrive from the northeast, clearly seen in the individually normalized plots (Fig. 7b). As the lag time increases to about 4 to 5 sec, the energy spreads more uniformly in the slowness plane, indicating increased levels of scattering from various directions. After 4 to 5 sec, there is some stability in the energy distribution over the slowness plane, with relatively well-defined peak arrivals that come from different directions. This corresponds to a transition to somewhat longer-period arrivals in the waveforms (Fig. 2), which presumably involve a larger percentage of scattered surface-wave energy. The patterns for the other events are similar but differ in detail. We can analyze the polarization of the coda to help identify the coda constituents.

The power distributions in the horizontal slowness plane for different particle motion directions for shot 2 are shown in Figure 8. For this analysis, the two horizontal components were projected onto the indicated particle motion azimuths,

and the resulting signals were processed using the slowness method. By considering all polarization directions and the associated array slowness analysis, we can consider the correspondence between sense of ground motion and direction of wave propagation, which can help to identify the wave type. Of course, the presence of overlapping phases scattered from different directions can confuse this simple polarization analysis, but our impression is that much of the coda involves scattered, but relatively coherent, surface waves. In the first two time windows, the strongest energy has a polarization of N60°E, arriving from the same azimuth, and there is almost no signal in the orthogonal direction of N150°E. This reflects the nearly linear polarization of the direct *P* wave, along the biased backazimuth. The next few seconds of coda have little coherent polarized energy, perhaps due to strong near-receiver scattering of the direct *P* phase that does not produce coherent plane waves across the array. The 4- to 5-sec window shows an energy peak for east–west polarized motion propagating toward the west across the array. This is consistent with a Rayleigh-wave arrival, arriving about 20° off the true backazimuth. Polarization analysis of the full ground motion supports this interpretation. This is probably the onset of the direct surface wave from the source, arriving with a velocity near 2 km/ sec, but may also involve *P* to Rayleigh scattered energy from the nearby topography. Later coda intervals, as well as similar polarization analysis for the other three shots, reveal similar behavior, azimuthally deflected direct *P* waves with coda that is dominated by *P-SV*-wave-type arrivals. More sophisticated methods to decompose the coda into distinct particle motion contributions exist (e.g., Wagner and Owens, 1993, 1995), but we do not pursue this given strong variability observed in the event-to-event behavior. This indicates that near-receiver scattering is very sensitive to the source azimuth, and our limited attempts to do any further deterministic imaging of the scattering structure were not encouraging. We turn our attention to the statistical aspects of the data.

Waveform Coherence

Spatial coherence of waveforms can be quantified using the cross-correlation coefficient (CCC) for pairs of seismograms as a function of the receiver spatial offset. The CCC can be computed in either the time or frequency domains. Similar to previous studies (Menke *et al.*, 1990, Vernon *et al.*, 1991), we use a conventional squared coherence measure. In the time domain, the CCC between two waveforms $s(x_1, t)$ and $s(x_2, t)$ at location x_1 and x_2 is

$$CCC\ (t, \Delta t, \Delta x) = \langle s(x_1, t) \cdot s(x_2, t) \rangle^2 / \langle s(x_1, t) \cdot s(x_1, t) \rangle \cdot \langle s(x_2, t) \cdot s(x_2, t) \rangle,$$

where $\langle\ \rangle$ denotes the average value of the enclosed function over a time interval Δt centered on t; the offset $\Delta x = |x_1 - x_2|$.
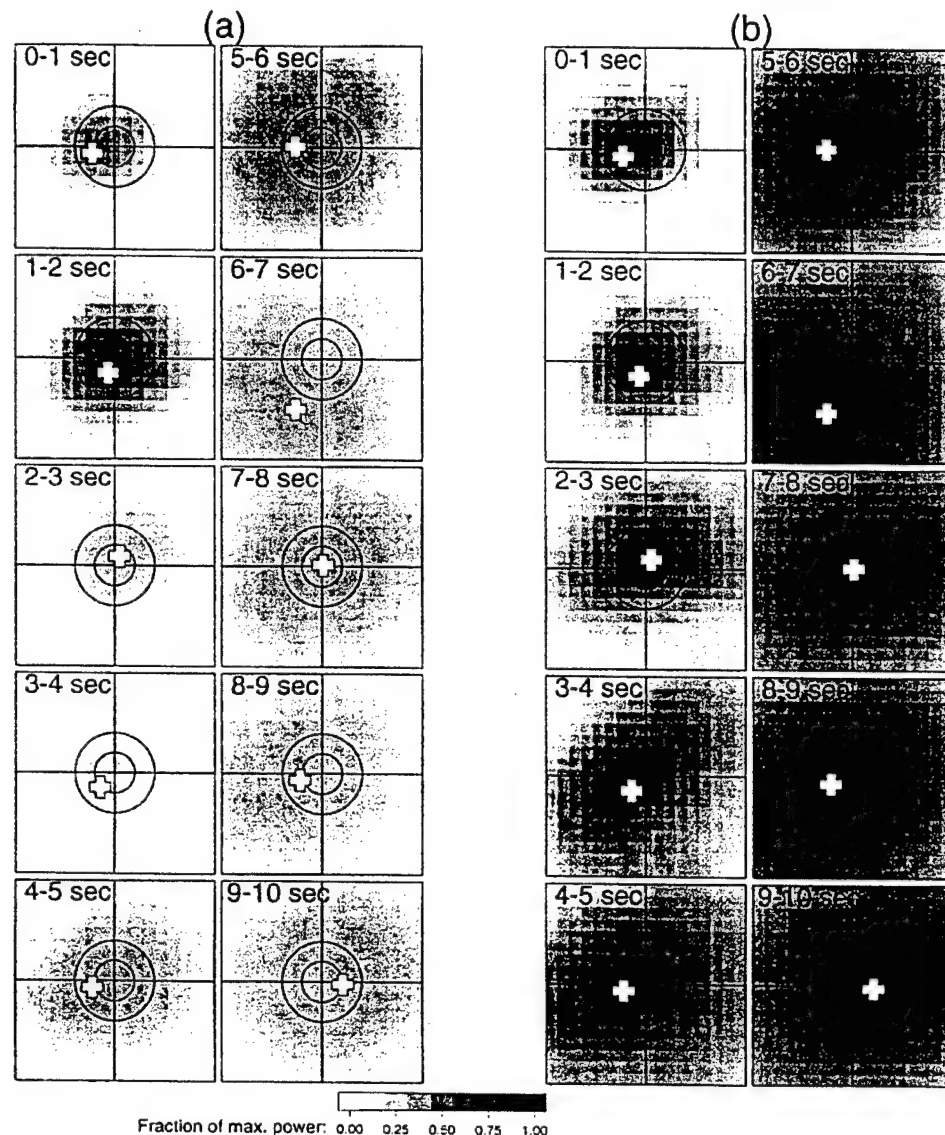
Figure 7.   Slowness vector analysis for shot 2. The summed power distributions in the horizontal slowness plane (up is north, right is east) for three components of ground motion are shown in 1-sec time windows. (a) Relative power (indicated by shading, with darker shades indicating relatively higher power) normalized to the largest value in the 10-sec window. (b) The same results normalized separately in each 1-sec window. Crosses indicate the peak power. Note that the slowness vector indicates the direction the plane wave is traveling as it traverses the array, not the backazimuth, which is opposite to the convention of *f-k* plots such as Figure 4c. The larger and smaller circles correspond to horizontal velocities of 1 and 2 km/sec, respectively. The true backazimuth is 101°, but few arrivals have slowness vectors near 281°.

Before calculating the CCC for a pair of waveforms, one must contend with the difficult issue of time shifts. With overlapping signals arriving from many possible azimuths, one cannot assume an appropriate move-out velocity for alignment, yet failing to shift the traces should bias the coherence measure low. For our alignments, we used relative time shifts among the array channels based on broadband cross-correlations of the traces. We select one of the stations near the center of the array as a reference trace. For each array element, a cross-correlation function is computed using a time window of 0.25 sec with sliding steps of 0.2 sec. The time lags for each window for all stations relative to the reference are applied to shift the data to common alignment when interstation correlations are computed. This procedure emphasizes the dominant frequencies in the signals and effectively shifts the signals to optimal coherence for the larger
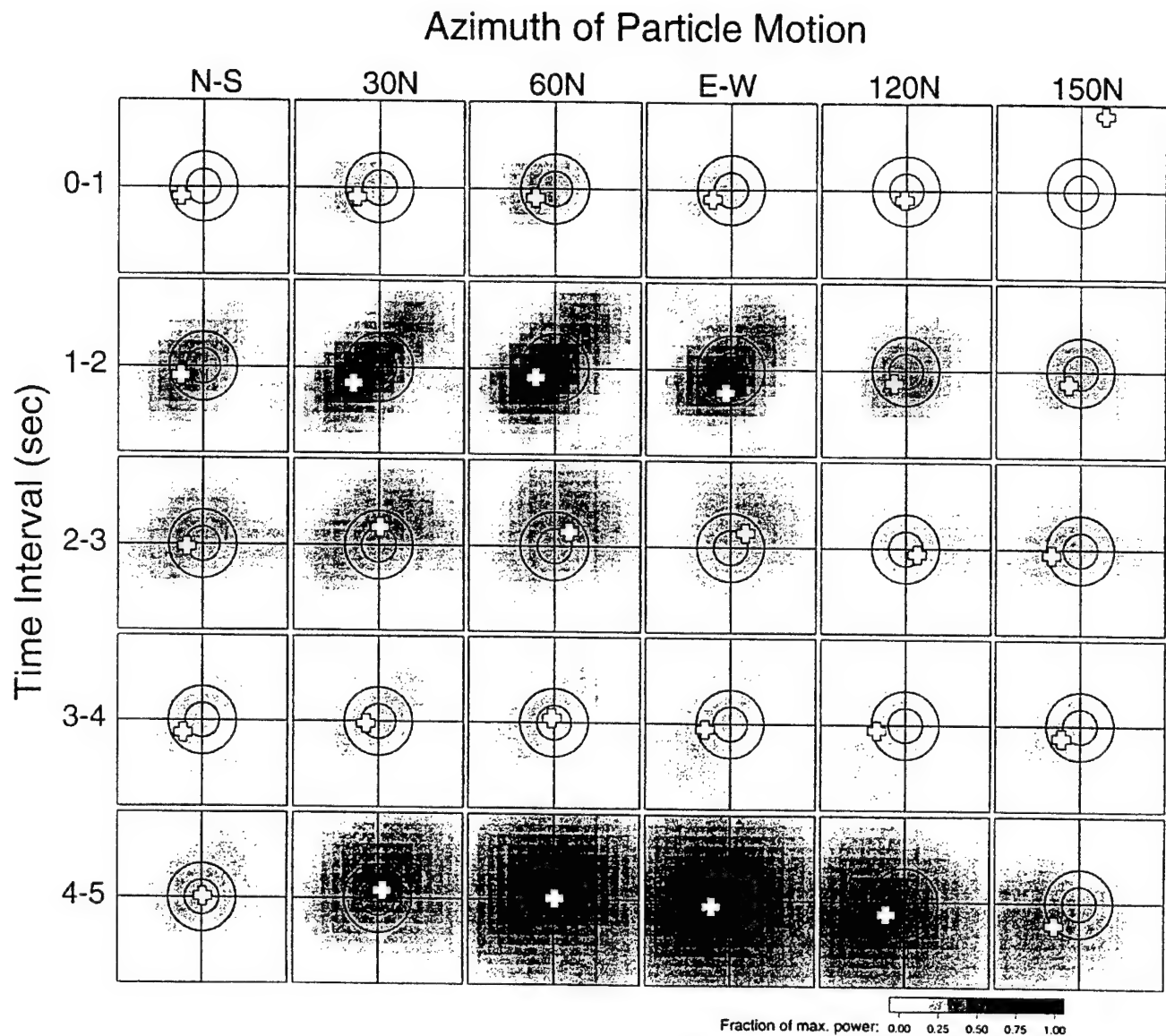
Azimuth of Particle Motion

Figure 8. Horizontal slowness vector power distributions for shot 2 (as in Fig. 7) using the horizontal components along different particle motion directions (obtained by rotating the north–south and east–west recordings onto various directions ranging from 0° (N–S) to 150° with 30° intervals. The relative power in all of the panels is normalized to the largest amplitude arrivals. The stronger (darker) arrivals have propagation directions roughly aligned with the particle motion, indicating that these are longitudinally polarized *P*- or Rayleigh-wave arrivals with backazimuth of 60° to 80°. The true backazimuth is 101°.

arrivals that could be traversing the array in each time window.

Each of our seismograms is filtered into a set of traces using Butterworth zero phase filters with a 5-Hz passband, moving steps of 3 Hz, and a total bandwidth from 3 to 33 Hz. The alignments found for the broadband signals are held fixed for correlation of the narrowband filtered traces, rather than optimizing the correlation in each passband, which could involve many cycle slips relative to the stronger arri-

vals. For each frequency band, we consider 0.5-sec portions of the waveforms with moving steps of 0.2 sec, aligned by the cross-correlation shifts. We compute the CCC between all record pairs for variable time lengths, T_w. T_w depends on the center frequency of the band, F_c:

$$T_w = 0.5 \times 5.5/F_c \text{ (sec)},$$

where 5.5 is the F_c of the lowest passband of 3 to 8 Hz and

0.5 is the time segment width for alignment. For example, $T_w (F_c = 5.5 \text{ Hz}) = 0.5$ sec; $T_w(F_c = 30.5 \text{ Hz}) = 0.09$ sec. Thus, for a center frequency of 5.5 Hz, there is one window for calculating the CCC, while for a center frequency of 30.5 Hz, we calculate the average CCC from five windows.

Menke *et al.* (1990) have considered the possible bias due to frequency-dependent alignment decisions and find that it is relatively small for time windows like those we used, which we confirmed by following their exact procedure for some of our data. Our procedure estimates the frequency-dependent decrease in coherence relative to the stronger broadband arrivals in each time window, which is right at the transition from the deterministic array analysis to the statistical behavior. This approach is valid given the weak frequency-dependent behavior we found in an *f-k* analysis of the data, which did not reveal the presence of strong plane-wave arrivals with distinct frequency content and differing arrival directions in each time window.

Variations of Coherence Down the Hillside

We noted earlier that Figure 2 suggests stronger waveform similarity along rows of the array than down the columns. To test this quantitatively, we calculated the average CCC between elements on rows, CCC_{row}, and between elements on columns, CCC_{col}. The mean value for 2-sec time windows for the vertical components from all four shots was computed for the 3- to 9-Hz frequency band as a function of the receiver spatial offset. We then computed the fractional difference in coherence:

$$CCC_{fcd} = 2 * (CCC_{row} - CCC_{col})/(CCC_{row} + CCC_{col}),$$

which is shown in Figure 9. This effectively measures the anisotropy in waveform coherence, with positive values indicating stronger coherence along rows. For spatial offsets of 15 and 30 m, the CCC_{fcd} is positive, confirming the statistical tendency for receivers at relatively uniform elevations (Fig. 2d) to record more similar waveforms. This is consistent with the presence of the southward-dipping surface and subsurface interfaces discussed in the previous section. A wedge-shaped structure will cause more similar reverberations at stations overlying comparable depths to interfaces. The fact that the array is not perfectly aligned with the structure, and the irregularity of the structure itself, causes the 45-m offsets to be less coherent and to have less spatial pattern. This spatial pattern in the statistical measure indicates that we are again measuring right at the level of transition from deterministic control on the array signals to a stochastic wave field. While supporting the general expectations of the near-surface structural effects, it is difficult to further constrain the structure with such statistical measures.
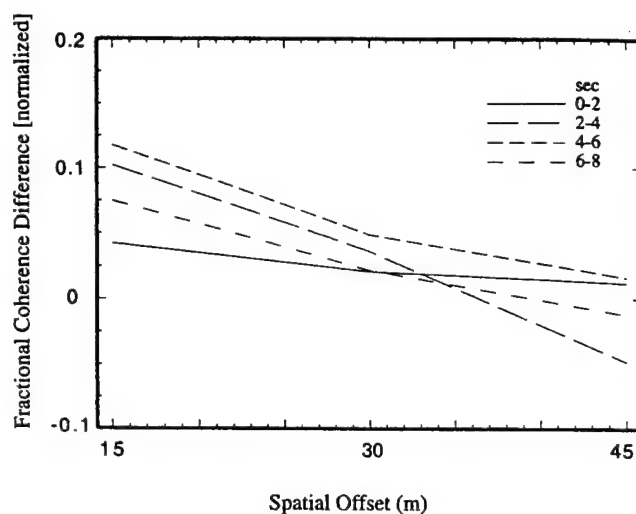

Figure 9. The difference in signal coherence on vertical components between east–west and north–south sensor offsets averaged for four shots. The difference is normalized by the mean coherence at each offset. Results are shown for four time windows in the signals, and the frequency band used is 3 to 9 Hz.

Variation of Coherence with Frequency, Spatial Offset, and Time Lag

Generally, the spatial coherence across the Zayante array reduces with increasing frequency, sensor offset, and time lag for recordings of all four shots. Average coherence versus spatial offset in various frequency bands and time windows for vertical-component seismograms for the four shots, for microtremor intervals, and for synthetic Gaussian noise are shown in Figure 10. The Gaussian noise has an average coherence value of 0.1 and the coherence is never more than 0.2. Therefore, coherence values for the data of less than 0.2 are not considered significant. The microtremor coherence has an average value of about 0.3, and there is less variance in the 3-sec microtremor window than in the 1-sec window. The coherence is not very dependent on the frequency band or the spatial offset for microtremor and Gaussian noise. The microtremor spectrum is relatively flat (Fig. 3), and the weak coherence suggests that the wave field involves much localized scattering of the signals traversing the array. For the high-frequency energy (>15 Hz) in the four shots, especially in the 3 to 9-sec window, the coherence approaches the level of the microtremor. This probably reflects the low energy level (Fig. 3), and the scattered nature of the coda (Fig. 7), which is comparable to the microtremor signal. We infer that coherence greater than about 0.3 reflects the presence of more coherent signals traversing the array than is typical of microseism.

Following Menke *et al.* (1990), the array coherence can be expressed by a simple empirical equation, $e^{-cf\Delta x}$, where c is a constant determined from the data. For the first 1-sec window for the vertical-component signals of the four shots $c = 0.6 \text{ km}^{-1} \text{ Hz}^{-1}$. This value is similar to the values of
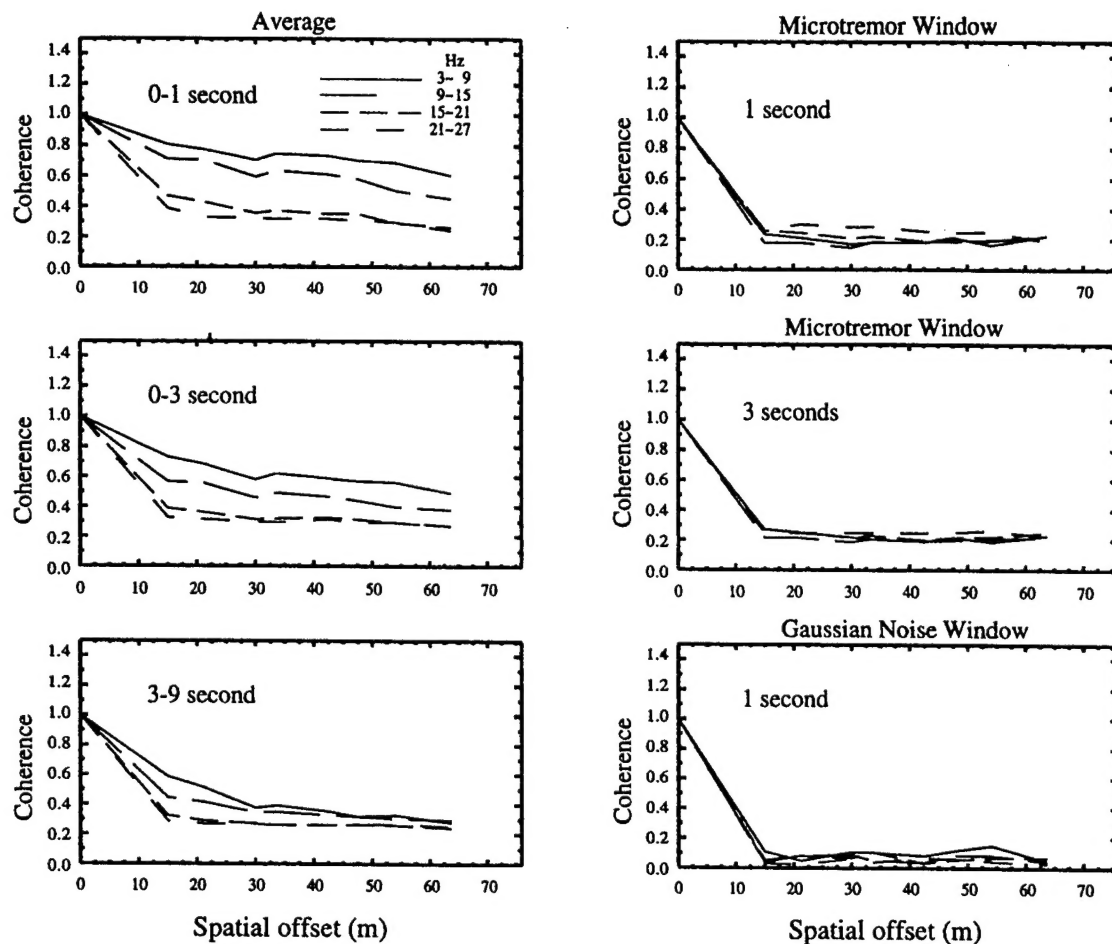
Figure 10. Average coherence versus spatial offset in various frequency bands and time windows for vertical-component seismograms of four shots (left) and microtremor noise (upper and middle right), as well as for synthetic Gaussian noise (bottom right). The coherence of the Gaussian noise is less than 0.2, and observed values below this level are considered to be noise.

0.4 to 0.7 km^{-1} Hz^{-1} found for direct arrivals at hard-rock sites (Menke *et al.*, 1990). This may imply that in the frequency range of 2 to 20 Hz, the coherence at wavelengths from tens to hundreds of meters may be controlled by similar heterogeneities below the surface for both soft- and hard-rock environments.

Averaging all CCC(t, Δt, Δx) for a given offset, we obtain the average spatial coherence as a function of time, frequency, and spatial offset for the Zayante array (Fig. 11). Results are shown for both the vertical (Z) components and the north–south (N–S) components of motion for shot 2, the average of all shots, and the microtremor windows. The microtremor coherence on vertical and N–S components has similar patterns with time and frequency and defines the background signal level. The first 1 to 2 sec of the shot signals have the highest coherence in all frequency bands, up to frequencies of about 27 Hz. The N–S components are always somewhat less coherent than the Z component, but the explosion signals display a similar general decrease of

coherence with time lag, frequency, and offset. The coherence values and trends with time, frequency (in the band 2 to 21 Hz, which has good signal to noise), and offset for the shots are similar to those at the hard-rock sites analyzed by Menke *et al.* (1990) and Vernon *et al.* (1991). While the Zayante array is located in a more complex geological environment, it appears that the small-scale near-surface heterogeneity induces comparable signal complexity to that found in other environments.

Discussion and Conclusions

The Zayante array recordings demonstrate the important role of site effects for the short-period seismic wave field. The site of this array is very typical of the geological environment in the Santa Cruz Mountains, and the host of complicated earthquake engineering issues raised by the 1989 Loma Prieta earthquake provide an important context for examining the high-frequency wave-field phenomena in this
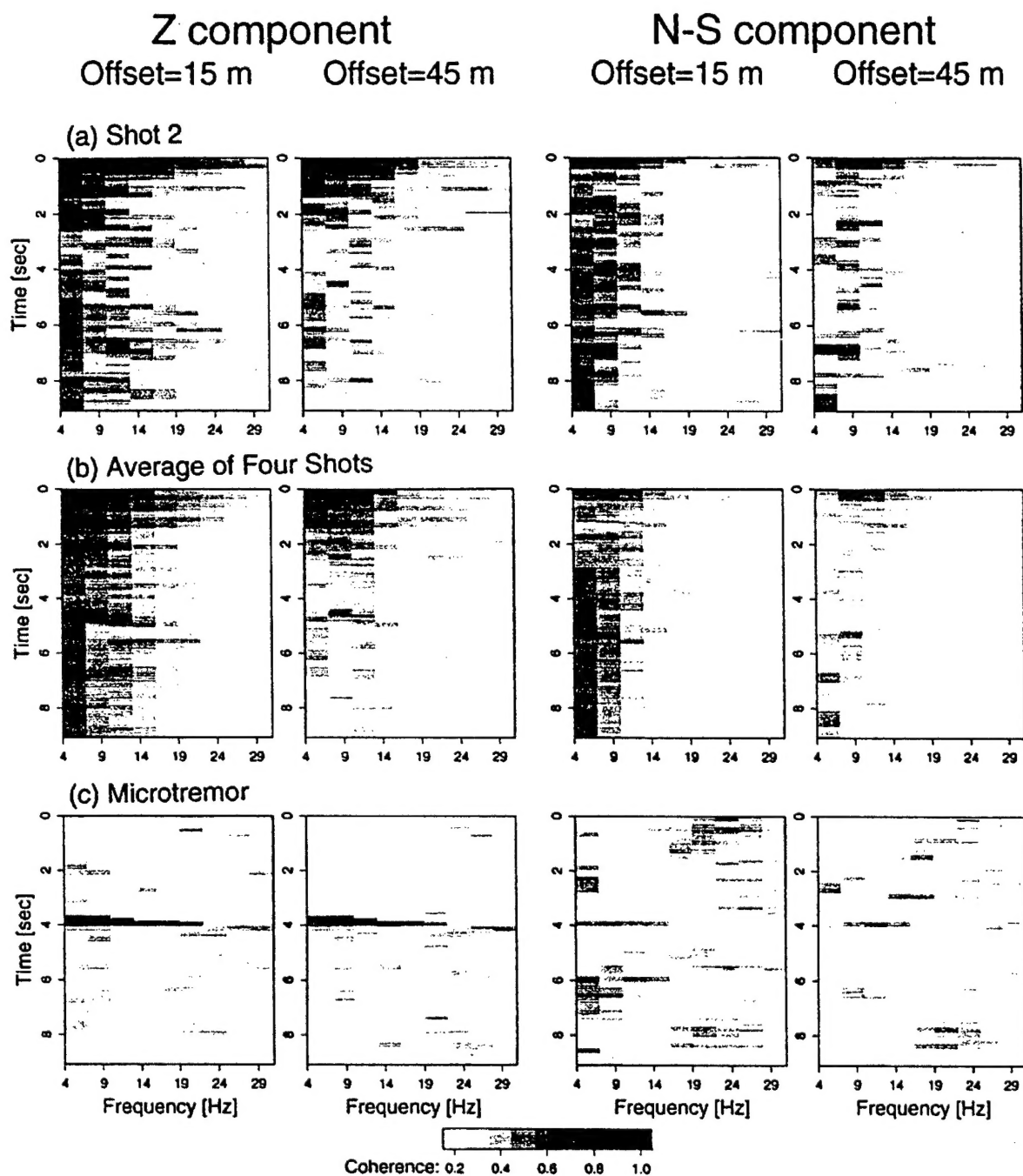
Figure 11. Waveform coherence (indicated by graytone shading from black to white, which corresponds to values of 1 to 0.2) versus time and frequency for offsets of 15 and 45 m for various subsets of the data. The results for vertical components (left two columns) and north–south components (right two columns) are shown for just shot 2 (upper row), for the average of four shots (middle row), and for the microtremor window (lower row).

region. The array aperture is too small to provide high resolution of incoming wave fronts, but both *P*-wave polarization and relative arrival times indicate large backazimuth biases of from 30° to 50°. While we could not fully reconcile both sets of observations with a simple model, it appears that subsurface dipping layers with fairly strong velocity contrasts are responsible for the large azimuthal deflections. In a region like the Santa Cruz Mountains, with very low velocity near-surface sediments, direct seismic waves are steeply incident under the receivers, which enhances their

sensitivity to azimuthal deflection by moderately dipping structures. Combined with strong near-surface lateral-velocity gradients, produced by boulders and heterogeneities in the weathered layer, there is high potential for single-sensor and even small-aperture array measurements to be biased by site effects. We qualitatively account for the observations with a simple three-dimensional velocity model motivated by the shallow seismic refraction survey. The actual structure is undoubtedly more complex, but the integrated effects of the structure appear to be in the correct regime.

Given the strong effect of shallow-dipping interfaces on the direct *P* wave, it is interesting to consider the effects on secondary arrivals. The receiver structure is such that one expects the entire wave field to be influenced, although variations in the incident angles of secondary arrivals should change the biases as a function of lag time into the coda. For both *P* and *S* waves, the effect of subsurface dipping interfaces with positive velocity contrasts is to refract the wave direction toward the normal to the interface, and toward the dip direction of the interface (Fig. 6). If we use the dipping interface to define the *SH* and *SV* components of motion, the amplification effect from refraction is most pronounced for the *SV* component, and the *SV* polarization is refracted to be more horizontal. The net effect of a dipping interface can thus be to cause some systematic polarization of the *S*-wave field, with amplification of motion in some directions. This will hold for complex wave fields with many *P*- and *S*-wave arrivals incident on the same structure from different azimuths. There will be a net refraction effect by the subsurface interface that can preferentially influence some components of motion.

The observation of preferred direction of *S*-wave shaking at the ZAYA array (Bonamassa *et al.*, 1991) may be in part due to the presence of dipping interfaces under the stations. It is useful to consider a simple geometry. Along the axis of a V-shaped valley structure underlying low-velocity material, as shown in Figure 12, the direction of the *S*-wave ray paths from different azimuths will be refracted so that the horizontal component of shaking tends to align with the axis of the valley. For sites overlying one of the valley flanks, waves incident from the updip side of the valley will be similarly refracted, while waves incident from the downdip side will refract so that horizontal shaking is along the dip direction. The precise pattern induced is a function of the incident wave parameters and the specific structural geometry. Frequency dependence of the preferred shaking directions is expected for complex layered structures, with finite-frequency effects differing in the extent of refraction and amplification for each passband. Higher frequencies will be more sensitive to very shallow structure, while lower frequencies average the structural effects over a larger depth extent. The development of preferred orientation of shaking is likely to be more pronounced in the coda than in the direct signal due to the fact that the coda involves arrivals from many azimuths, which allows the effect of refraction toward specific directions to accumulate. While simulation with
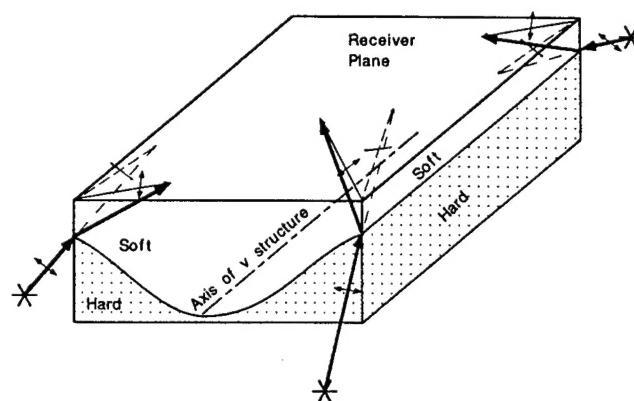

Figure 12.   Interpretation of preferred direction of *S*-wave horizontal shaking caused by subsurface structure. Dipping interfaces beneath the station rotate the surface particle motion toward the strike of the dipping interface for waves incident from the up-dip direction. For a V-shaped valley as shown, the *S*-wave shaking will be preferentially oriented along the axis of the valley. *S*-wave ray paths incident from below the valley are shown for several azimuths, with the bold lines. The thin dashed arrows on the surface indicate the azimuth those rays would have if not refracted by the dipping sides. The thin solid arrow on the surface indicates the refracted azimuth. Note that the sense of *S*-wave shaking (small two-headed arrows) is refracted toward the axis of the valley.

three-dimensional wave propagation is needed to quantify the structural effect (and is being conducted by Bonamassa and Vidale, in preparation), the numerical simulations of Khair *et al.* (1991) show that preferred directions of ground shaking do develop along the valley axis as described, as a complex function of geometry and incidence angle. While simple dipping structures may not give rise to all of the directional resonances observed by Bonamassa *et al.* (1991), it is likely that they provide the gross structural controls, with superimposed small-scale heterogeneity. The wedge-like shape of this particular site effect may also contribute reverberation patterns that enhance directional interference.

The other clear manifestation of site effect in the Zayante data is the rapid spatial decay of high-frequency waveform coherence, which proves comparable to that observed at harder-rock sites. While some mild spatial systematics influenced by the gross structure were detected, the main feature is that high-frequency coherence drops off rapidly on the scale of tens of meters. This provides further evidence for caution in interpretation of high-frequency signal in terms of source effects, unless the site effect can be reliably corrected for.

Acknowledgments

References

Bannister, S. C., E. S. Husebye, and B. O. Ruud (1990). Teleseismic P coda analyzed by three-component and array techniques: deterministic location of topographic P-to-Rg scattering near the NORESS array, *Bull. Seism. Soc. Am.* **80b,** 1969–1986.

Bonamassa, O. and J. E. Vidale (1991). Directional site resonances observed from aftershocks of the 18 October 1989 Loma Prieta earthquake, *Bull. Seism. Soc. Am.* **81,** 1945–1957.

Bonamassa, O., J. E. Vidale, H. Houston, and S. Y. Schwartz (1991). Directional site resonances and the influence of near-surface geology on ground motion, *Geophys. Res. Lett.* **18,** 901–904.

Bonamassa, O., J. E. Vidale, and A. Nardi (1993). P- and S-wave tomography on the Santa Cruz Mountains: an attempt to explain directional resonances, *EOS* **74,** 437.

Brabb, E. E. and D. T. W. Dibblee Jr. (1979). Preliminary geologic map of the Castle Rock Ridge quadrangle, Santa Cruz and Santa Clara counties, California, *U.S. Geol. Surv. Open-File Rept. 79-0659.*

Buchbinder, G. G. R. (1987). P-wave deflection or off-azimuth arrivals in the Charlevoix seismic zone, *Bull. Seism. Soc. Am.* **77,** 2152–2162.

Buchbinder, G. G. R. (1990). Shear wave splitting and anisotropy from the aftershocks of the Nahanni, Northwest Territories, earthquakes, *J. Geophys. Res.* **95,** 4777–4785.

Buchbinder, G. G. R. and R. A. W. Haddon (1990). Azimuthal anomalies of short-period P-wave arrivals from Nahanni aftershocks, Northwest Territories, Canada, and effects of surface topography, *Bull. Seism. Soc. Am.* **80,** 1272–1283.

Bullen, K. E. (1963). *An Introduction to the Theory of Seismology,* Cambridge University Press, New York, 381 pp.

Cassidy, J. F. (1992). Numerical experiments in broadband receiver function analysis, *Bull. Seism. Soc. Am.* **82,** 1453–1474.

Dainty, A. M. and M. N. Toksöz (1990). Array analysis of seismic scattering, *Bull. Seism. Soc. Am.* **80,** 2242–2260.

Eberhart-Phillips, D. and A. J. Michael (1991). The 1991 active seismic experiment in the Loma Prieta, California region: shallow seismicity and fault structure, *EOS* **72,** 311.

Frankel, A., S. Hough, P. Friberg, and R. Busby (1991). Observation of Loma Prieta aftershocks from a dense array in Sunnyvale, California, *Bull. Seism. Soc. Am.* **81,** 1900–1922.

Geli, L., P.-Y. Bard, and B. Jullien (1988). The effect of topography on earthquake ground motion: a review and new results, *Bull. Seism. Soc. Am.* **78,** 42–63.

Gupta, I. N., C. S. Lynnes, T. W. McElfresh, and R. A. Wagner (1990). Broadband f-k analysis of NORESS array and single station data to identify sources of near-receiver and near-source scattering, *Bull. Seism. Soc. Am.* **80B,** 2227–2241.

Hartzell, S. H., D. L. Carver, and K. W. King (1994). Initial investigation of site and topographic effects at Robinwood Ridge, California, *Bull. Seism. Soc. Am.* **84,** 1336–1349.

Hedlin, M. A. H., J. B. Minster, and J. Orcutt (1991). Beam-stack imaging using a small aperture array, *Geophys. Res. Lett.* **18,** 1771–1774.

Khair, K. R., S. K. Datta, and A. H. Shah (1991). Amplification of obliquely incident seismic waves by cylindrical alluvial valleys of arbitrary cross-sectional shape. II. Incident SH and Rayleigh waves, *Bull. Seism. Soc. Am.* **81,** 346–357.

King, J. L. and B. E. Tucker (1984). Observed variations of earthquake motion across a sediment-filled valley, *Bull. Seism. Soc. Am.* **74,** 137–151.

Langston, C. A. (1977). The effect of planar dipping structure on source and receiver responses for constant ray parameter, *Bull. Seism. Soc. Am.* **76,** 1029–1050.

Langston, C. A. (1979). Structure under Mount Rainier, Washington, inferred from teleseismic body waves, *J. Geophys. Res.* **84,** 4749–4762.

Magotra, N., N. Ahmed, and E. Chael (1987). Seismic event detection and source location using single-station (three-component) data, *Bull. Seism. Soc. Am.* **77,** 958–971.

Menke, W., A. L. Lerner-Lam, B. Dubendorff, and J. Pacheco (1990). Polarization and coherence of 5 to 30 Hz seismic wavefields at a hard-rock site and their relevance to velocity heterogeneities in the crust, *Bull. Seism. Soc. Am.* **80,** 430–449.

Menke, W. A., L. Shengold, G. Hongsheng, H. Ge, and A. Lerner-Lam (1991). Performance of the short-period geophones of the IRIS/PASSCAL array, *Bull. Seism. Soc. Am.* **81,** 232–242.

Mori, J., J. Filson, E. Cranswick, R. Borcherdt, R. Amirbekian, V. Aharonian, and L. Hachverdian (1994). Measurements of *P* and *S* wave fronts from the dense three-dimensional array at Garni, Armenia, *Bull. Seism. Soc. Am.* **84,** 1089–1096.

Niazi, M. (1966). Corrections to apparent azimuths and traveltime gradients for a dipping Mohorivicic discontinuity, *Bull. Seism. Soc. Am.* **56,** 491–509.

Pedersen, H., B. Lebrun, D. Hatzfeld, M. Campillo, and P. Y. Bard (1994). Ground-motion amplitude across ridges, *Bull. Seism. Soc. Am.* **84,** 1786–1800.

Suteau-Henson, A. (1990). Estimating azimuth and slowness from three-component and array stations, *Bull. Seism. Soc. Am.* **80,** 1987–1998.

Suteau-Henson, A. (1991). Three-component analysis of regional phases at NORESS and ARCESS: polarization and phase identification, *Bull. Seism. Soc. Am.* **81,** 2419–2440.

Tucker, B. E. and J. L. King (1984). Dependence of sediment-filled valley response on input amplitude and valley properties, *Bull. Seism. Soc. Am.* **74,** 153–165.

Tucker, B. E., J. L. King, D. Hatzfeld, and I. L. Nersesov (1984). Observations of hard-rock site effects, *Bull. Seism. Soc. Am.* **74,** 121–136.

Vernon, F. L., J. Fletcher, L. Carroll, and A. Chave (1991). Coherence of seismic body waves from local events as measured by a small-aperture array, *J. Geophys. Res.* **96,** 11981–11996.

Wagner, G. S. and T. J. Owens (1993). Broadband bearing-time records of three-component seismic array data and their application to the study of local earthquake coda, *Geophys. Res. Lett.* **20,** 1823–1826.

Wagner, G. S. and T. J. Owens (1995). Regional wavefield decomposition and characterization using three-component seismic array data, *J. Geophys. Res.,* in press.

Xie, X.-B. and T. Lay (1994). The excitation of explosion Lg: a finite-difference investigation, *Bull. Seism. Soc. Am.* **84,** 324–342.

Zhang, J. and C. A. Langston (1992). 2-D and 3-D structure effects on the receiver functions, *Seism. Res. Lett.* **63,** 37.

Institute of Tectonics and W. M. Keck Seismological Laboratory
University of California, Santa Cruz
Santa Cruz, California 95064